University of Strathclyde

Department of Naval Architecture, Ocean and Marine Engineering

Fluid-Structure Interaction Models on the Hydroelastic Analysis of Containerships in Waves

Yujia Wei

A thesis presented in fulfilment of the requirements for the degree of Doctor of Philosophy

2023

This thesis is the result of the author's original research. It has been composed by the author and has not been previously submitted for examination which has led to the award of a degree.

Signed: Yujia Wei Date: 08/03/2023

I dedicate this to my grandmother, wishing her to get well soon and enjoy her twilight years.

Acknowledgements

There are no proper words to convey my deep gratitude to my supervisors, Dr Tahsin Tezdogan and Prof. Atilla Incecik, for their continuous support and thoughtful guidance throughout my doctoral journey.

Firstly, I express my most profound appreciation to my prime supervisor Dr Tezdogan, who provides me with this PhD opportunity to learn from him during the past three years. He is a remarkable mentor, a terrific teacher and a wonderful friend. I have benefited from his extensive experience and guidance in my academic and private life. I aspire to him as the template for my future life and career. In addition, I would also like to thank my second supervisor Prof. Atilla Incecik for his treasured support and experience, which were really influential in shaping my research mind and future career.

I am most grateful to the collaborators for leading me with their expertise and intuition in my research problems: Dr JiaoLong Jia; Mr Huang Songxing, and other computational scientists at the South China University of Technology.

Several important elements should be factored into the completion of this work: I would like to thank our department’s research secretaries, Mrs Susan and Lynn, for all of their assistance and great support. I would also like to thank the University of Strathclyde Faculty of Engineering for the provision of the ARCHIE-WeSt high-performance computing facilities and associated supported services.

I am deeply indebted to my parents, Chen Shumei and Wei Yong, for their everlasting love, encouragement and financial support. It was their love that raised me up again when I got weary. I would also thank my beloved girlfriend Miss Zhang Xinyu, and her parents for their full understanding and support. I am genuinely grateful to Xinyu and Poppy for always keeping me company and making every day special.

Finally, I would like to thank all my colleagues and friends who assisted me during my PhD and helped me to spend three fantastic years in Glasgow. Dr Momchil Terziev, Dr Huang Yang, Dr Zhou Yang, Dr Jin Peng, Mr Zhang Deqing, Mr Hou Hongbo, Mr Yu Shuangrui, Dr Zhang Ming, Mr Zhao Guangwei, Dr Zhou Banghao, Dr Li Shen. Special thanks to Mr Li Xiang, my colleague and flatmate, who understands me the best, encourages and helps me get through this agonizing period in the most positive way.

Contents

List of Figures

List of Tables

Nomenclature

Roman Symbols

U	Fluid velocity
U_g	Flow velocity of gird node
U_r	Artificial compressive velocity
P_d	Dynamic pressure
μ_{eff}	Effective dynamic viscosity
f_σ	Surface tension
U_r	Artificial compressive velocity
ρ_w	Water density
ρ_a	Air density
E	Young's modulus
Γ_k	Effective diffusivity of the turbulent kinetic energy
k	Turbulent kinetic energy
Γ_ω	Effective diffusivity of the specific dissipation rate
ω	Specific dissipation rate
$\check{P}_k$	Turbulence production terms
D_ω	Dissipation terms
Y_ω	Cross-diffusion term
μ_t	Turbulent viscosity
a_k	Turbulent coefficient
S	Strain rate magnitude
I	Turbulence intensity
μ_{ref}	Reference velocity
l	Turbulence length scale

a_i	Amplitude of wave components
x_0	Focal location
t_0	Focal time
t	Time
A_0	Target theoretical linear wave amplitude
k	Wave number
U_s	Displacement vector of the structure
P_s	Second Piola-Kirchoff stress tensor
f_s	Body force per unit mass
q	Position
$\dot{q}$	Velocity
$\ddot{q}$	Acceleration
g	Gravity
V_T	Turbulent kinetic eddy viscosity
d	Point displacement field
δ_B	Deflection of beam point
I	Moment of inertia
M	Bending moments
y	The distances to point from neutral axis
λ	Scale factor
B	Breath
L	Characteristics length
T	Design draft
KG	Vertical centre of gravity
k_{yy}	Moment of inertia

R_e	Reynolds number
H_s	Wave frequency
C_b	Block coefficient
A	Displacement
F_n	Froude number
h	Wave depth
V	Current speed
F_x	Axial force component
F_y	Shear force component at y direction
F_z	Shear force component at z direction
ε_x	Axial strain
κ_x	Bending curvature parameters
∇	Displacement volume
p	Order of accuracy
R	Convergence ratio
G	Shear Modulus
EI_y	Flexural rigidity
d	Structure damping

Greek Symbols

a	Volume fraction variable
γ	Diffusion coefficient for mesh motion equation
η	Free surface elevation
μ	Dynamic viscosity of fluid
ν	Kinematic viscosity of fluid
ρ	Density of fluid
θ	Wave angle
ω	Angular frequency
ϕ	wave phase
δ	Adjacent layer thickness
ν	Poisson ratio
ξ	Wave Amplitude
φ	Phase angle

Abbreviations

1D	One-dimensional
2D	Two-dimensional
3D	Three-dimensional
CFD	Computational fluid dynamics
DoF	Degree of freedom
FEA	Finite element analysis
MBD	Multibody dynamics
FSI	Fluid structure interaction
DMB	Discretized module beam
RANS	Reynolds averaged Navier-stokes
SST	Shear stress transport
RAO	Response amplitude operator
VOF	Volume of fluid
VBM	Vertical bending moment
S_VBM	Still water vertical bending moment
W_VBM	Wave-induced vertical bending moment
T_VBM	Total vertical bending moment
PM	Pierson–Moskowitz
BEM	Boundary element method
MPWEs	Most probable wave episodes
WEC	wave energy converters
FOWT	Floating offshore wind turbine
FVM	Finite volume method
EB	Euler-Bernoulli

CTV	Crew transfer vessel
FDM	Finite difference method
FEM	Finite element method
HOBEM	Higher-order boundary element method
DNS	Direct numerical simulation
LES	Large eddy simulation
ITTC	International towing tank conference
URANS	Unsteady Reynolds Averaged Navier Stokes
SPH	Smoothed particle hydrodynamics
FSPO	Floating production storage and offloading
VLFS	Very large floating structure
NWT	Numerical wave tank
DAE	Differential-Algebraic Equations
GEBT	Geometrically Exact Beam Theory
PISO	Pressure implicit with splitting of operator
SIMPLE	Semi-implicit method for pressure-linked equations
GCI	Grid convergence index
RE	Richardson extrapolation
CAE	Computer-aided engineering
IMO	International Maritime Organization
MC	Monte Carlo
WP	Wave probe
LCG	Longitudinal distance of the centre of gravity
aCG	Longitudinal distance of acceleration

Abstract

Commercial vessels have recently been increasing in size to meet the fast-growing demand for transportation and operations. However, this trend may result in more flexible or "softer" hulls. The flexible hull structure and high operational speed requirements bring the ship's natural frequency closer to the wave encounter frequency, increasing the probability of resonance or high-frequency vibrations. Therefore, hydroelastic effects and relevant loads should be considered when designing wave loads and evaluating the strength of large ships.

A robust numerical model is in search of ship designers and regulators, intended to predict the impact of hydroelasticity in the initial stages of design as per the design regulations, where there exists a greater opportunity to make modifications and utilise high-fidelity tools to verify the performance of advanced designs.

This study aims to fill this gap by performing robust numerical investigations based on open-source software on the seakeeping and hydroelastic analysis of a monohull under wave excitations. Firstly, a detailed literature review is presented to overview the previous theoretical and numerical methods for ship hydroelasticity. This review also includes a general comparison between these hydroelastic techniques and discusses the differences.

Following this, two fully coupled CFD-based unsteady FSI numerical frameworks are established: coupled CFD-FEA and CFD-DMB methods, respectively. The physical principle of these FSI models is to treat a ship's surface hull as an elastic body and interact with its surrounding flow field to form a fully coupled system. Taking advantage of the present numerical models, the hydroelastic behaviours of a containership, such as its vertical bending displacement and corresponding bending moment, can be quantified, and the "springing" and "whipping" behaviour can be measured. It is believed that the present FSI model will exhibit more advantages over the traditional rigid-body method in the ship seakeeping field.

Later, the presented CFD-DMB model is further extended for its application to irregular extreme waves and damaged ship conditions. The results achieved from these studies could also help to assess the structural integrity and longitudinal strength of a ship (intact or damaged), which serves as an improved technique for regulations to evaluate conventional ship designs.

Finally, the results drawn from each chapter of this thesis are summarised and discussed, and recommendations are made for future research.

1 Introduction

This chapter provides an overview of the topics covered in this thesis. It lists the motivations behind each chapter and presents individual research aims and objectives. Finally, the chapter provides an overview of the thesis structure.

1.1 General Perspectives

The global impact of the hydroelastic effects on a ship structure could be categorised into the springing and whipping phenomena. The magnitude of springing loads is usually low, and thus, the influence of springing on ship structure is usually not an ultimate strength issue (Jiao et al. 2021). However, springing vibrations could significantly contribute to the fatigue damage of the hull structure due to continuous high-cycle loads during long-term operation (Han et al. 2017).

On the other hand, whipping loads are by means of transient impact loading due to fierce bow, stern flare and bottom slamming. The oscillations usually decay rapidly due to the fluid and structural damping effects. However, whipping can add dynamic stress to the structure of the same order of magnitude as the wave-induced bending stress. Thus, predicting whipping response is significant for ultimate strength estimation with failure mode detection.

Current numerical capabilities for global ship hydroelastic analysis range from modal description of a beam model with strip theory, to CFD method coupled with the full finite-element discretization of the ship structure. In addition, extensive research has been proposed based on the potential-flow methods that use either the modal model or finite element model for the structure.

Viscous effects are likely to be the most dominant, particularly in large amplitude waves and high Froude number (Fn) conditions, which are ignored in potential flow theory . CFD is a good alternative as it can implicitly consider nonlinearities arising from the hydrodynamic actions and aid in visualizing the flow features (Jiao et al. 2021). Furthermore, CFD-based techniques are advantageous for performing exploratory studies at much less expense than analogous experimental studies.

While CFD simulations can routinely provide global ship motions and external loadings, the hull section loads required for wave load analysis, such as vertical bending moment and shearing force, cannot be directly obtained. Therefore, the CFD method can be coupled with a structure solver to study the dynamic responses of a flexible ship on a free surface. In the past, due to the high computational costs of transient FSI simulations, often a one-way coupling was used where the added mass effects were not considered in the fluid simulation.

Continued technology advances offer ever-increasing computational power, which extends the capacity to implement a two-way coupling algorithm for the FSI model. In some cases, CFD and finite element analysis (FEA) are coupled based on a two-way coupling algorithm for the hydroelastic simulations. In this method, the external fluid loads obtained from the CFD solver and the motions and structural deformations obtained from the FEA solver are exchanged between each other in a staggered coupling regime in the time domain. However, the CFD-FEA coupling method requires significant computational efforts, making it challenging to extend its applications to irregular wave conditions. An efficient CFD-DMB method is recently implemented in this study for ship hydroelasticity analysis. In this approach, the ship hull is divided into multiple floating rigid sections, while a stiffness matrix based on an Euler-Bernoulli (EB) beam theory, equivalently representing the structure's stiffness, is employed to connect ship neighbouring sections. A series of validation and verification studies are presented on the present CFD-DMB method and compared to the co-simulation and experimental solutions with the favourable agreement.

Following this, two critical factors in the ship hydroelasticity are investigated based on the present CFD-DMB method, i.e., extreme wave loads and damaged ship conditions. The numerical results from these applications will be valuable in better assessing the longitudinal strength of the ship with the consideration of structural integrity (intact and damaged), which assists in conventional ship designs and post-damaged evacuations.

To the best of this author's knowledge, this thesis introduces novel research which builds on that found in the current literature.

Throughout this thesis, the open-source CFD toolbox OpenFOAM, which is developed under the GNU rule, is used wherever an unsteady RANS approach has been applied. Additionally, two open-source structural solvers, Calculix and MBDyn are adopted for the ship structural deformation analysis. The supercomputer facility at the University of Strathclyde (ARCHIE-WeST) has been utilized for parallel studies of extensive simulations.

1.2 Motivations behind this Study

Before detailing the specific objectives of this thesis, an overview of the general motivations behind this study given in each chapter will be presented, along with a brief demonstration of how these studies fill in the gaps in the literature.

- With the fast development of the offshore wind industry, to facilitate the incoming maintenance work, crew transfer vessels (CTVs) by means of sending technicians from land to site also support landing operation services. Such landing operation requires the means to own high seakeeping capacity, in which the vessels must remain stationary for several minutes during the transfer phases. Therefore, a numerical model was established to evaluate the seakeeping characteristics of a CTV in wave conditions. The Unsteady RANS model adopted in OpenFOAM was employed in this study to solve the flow field. Correspondingly, the dynamic ship motions were calculated from the fluid forces at hull surface. The numerical results were validated against exploratory studies previously conducted at the University of Strathclyde, which aimed to evaluate the most feasible OpenFOAM modelling setup (Chapter 4.2).

- The hydroelastic responses of large vessels, such as containerships operating in waves, are of particular importance for ensuring structural integrity and safety. This is because vibration-induced loads are superimposed onto wave-induced loads, which can enlarge the structure's responses. In such cases, the deformation of the structure may significantly violate the surrounding flow fields, forming a fully coupled system. The original assumption of a rigid ship may lead to inaccurate predictions of hydrodynamic loadings and ship motions. To address this, a quantitative FSI method based on the CFD-FEA coupling approach was established to predict the accurate hydrodynamic forces and subsequent hydroelastic responses of a container ship under wave excitations. Although the CFD–FEA coupling method has been used to predict ship hydroelastic responses in some literature, the related numerical technique is immature and still needs to be further applied and refined owing to its high superiority. The present work fills the gap that no open-source FSI framework was developed for ship hydroelasticity studies. This study will shed light on open community users who are interested in repeating such work for their future studies (Chapter 5).
- Most ship hydroelastic research in the literature has focused on regular wave conditions. However, regular waves are not representative of actual extreme events. On the other hand, simulating random waves based on transient RANs simulation requires long runs to capture near-extreme events, resulting in huge computational burdens. In practice, focused wave events generated based on the “New wave” theory are used as an alternative to long-term irregular wave simulations. This study aims to fill the gap that in related ship hydroelasticity research investigates on the extreme ship motions based on the focused wave theory and a two-way FSI model. The improved and validated numerical tool used in this study is expected to provide more precise and detailed insight into the physical phenomena of the ship's dynamic motions and its hydroelastic loads in real sea conditions.

The goal of this work is to access the structural integrity of the ship longitudinal strength in extreme condition, which serves an improved technique to evaluate conventional ship designs (Chapter 6).

- Intensive shipping activities inevitably increase the likelihood of ship accidents, such as collision, contact and grounding. These accidents can result in catastrophic consequences in terms of structural damage and human loss. Damage to the ship's surface frequently occurs during ship-to-ship collisions. Seawater floods into the damaged compartment with sloshing effects, which poses a severe risk to the ship's stability and increases the risk of capsizing. Even if the ship survives the damage from a stability perspective, it can still suffer from increased longitudinal vertical bending moments of the hull girder. Therefore, a novel FSI model was established in this chapter to fill the gap that the majority of research in the literature on damaged ships treated ships as rigid bodies, in which the hydroelastic loads at the hull girder were not considered. The numerical results in this study are valuable to determine whether the damaged ship will experience secondary damage due to hydroelastic response, thereby helping to decide whether the emergency response in the post-accident situation is required and helping with the design of future conventional ships (Chapter 7).

1.3 Research Aim and Objectives

The main objective of this thesis is to perform numerical investigations on the nonlinear wave-induced load effects of the selected S175 type of containership with consideration of ship hydroelasticity under different environmental conditions. The specific objectives of this thesis have been arranged to cover all of the cutting-edge issues in the previous chapters and are stated as follows:

- To review the available literature on ship hydroelasticity problems and to investigate the advantages and drawbacks through various prediction techniques.
- To evaluate the optimal settings in OpenFOAM by conducting a CFD application of a CTV operating in regular head waves.
- To evaluate the performance of 1D beam modelling among FEA, DMB and theoretical methods and discuss their capabilities of extending to the ship applications.
- To establish an open-source CFD-based FSI coupling approach to predict the dynamic motions and sectional loads of a containership operating in regular head seas.

- To demonstrate the sensitivity and uncertainty of the adopted CFD-FEA model for a flexible containership sailing in regular waves.
- To develop an effective CFD-DMB framework employing a proficient two-way loose coupling algorithm to address the significant computational demands imposed by the coupling of CFD and FEA methods.
- To predict the extreme wave loadings on a flexible containership in response-conditioned waves using the CFD-DMB approach for short-term nonlinear analysis.
- To investigate the influences of the surface hull damages on damaged ship motions and residual hull girder stress considering ship hydroelasticity.
- To better understand of the local flooding water dynamics inside the damaged compartment.

1.4 Publications

The above research objectives were achieved, and the related numerical results were published in three conference papers and two journal papers. The summary of these papers is outlined below:

Journal Publications:

1 **Wei, Y.**, Incecik, A., & Tezdogan, T. (2022). A fully coupled CFD-DMB approach on the ship hydroelasticity of a containership in extreme wave conditions. *Journal of Marine Science and Engineering*, *10*(11), 1778.

2 **Wei, Y**., Incecik, A., & Tezdogan, T. (2022). Ship hydroelasticity analysis of a damaged ship based on a two-way coupled CFD-DMB method. *Ocean Engineering*, https://doi.org/10.1016/j.oceaneng.2023.114075.

Conference Publications:

3 **Wei, Y.**, & Tezdogan, T. (2021, September). A CFD study of the behavior of a crew transfer vessel in head seas using OpenFOAM. In *2nd International Conference on Ship and Marine Technology*. **Presenter** in Hybrid, June 2021

4 **Wei, Y.**, & Tezdogan, T. (2022, June). A fluid-structure interaction model on the hydroelastic analysis of a container ship using PRECICE. In *International Conference on Offshore Mechanics and Arctic Engineering* (Vol. 85925, p. V007T08A035). American Society of Mechanical Engineers. **Presenter** in Hybrid, Hamburg, Germany, June 2022.

5 **Wei, Y.**, Incecik, A., & Tezdogan, T. (2023). A numerical assessment of propeller-excited vibration on the hull girder of a containership in waves based on a two-way coupled FSI model. *IACM COMPUTATIONAL FLUIDS CONFERENCE (CFC)* [Abstract Accepted].

1.5 Thesis Structure

- Chapter 2 (Critical Review) provides a comprehensive literature survey of the theoretical and numerical models developed to solve seakeeping and hydroelastic problems for ships. It presents the historical evolution across traditional rigid ship seakeeping method to wave-flexible body interaction method. This chapter is an essential foundation for understanding the succeeding chapters.
- Chapter 3 (Numerical Methods) delves into the physical principles of the CFD and structural solvers used in this study, along with derived formulations. Additionally, it discusses two established FSI coupling frameworks, the CFD-FEA and CFD-DMB methods, are explained. A general discussion of the strength and weaknesses between two frameworks is also presented.
- Chapter 4 (Validation Studies) presents three validation studies for each separate solver before coupling them together. The first validation study evaluates the beam modelling performance through finite element analysis (FEA) and multibody dynamics (MBD) using theoretical values. The second validation study assesses the accuracy of the CFD solver by applying a rigid CTV in waves. Finally, the third validation study examines the accuracy of the coupled CFD-DMB method by investigating the dynamic motions of a flexible barge in waves. The results of these validation studies provide a foundation for the succeeding chapters.
- Chapter 5 (Hydroelastic Analysis of a Containership in Regular Heading Waves Based on a CFD-FEA Coupling Approach Using PreCICE) established a novel CFD-FEA framework for ship hydroelasticity. The elaborate preCICE library is implemented to communicate the fluid solver “OpenFOAM” and structure solver “CalculiX”. This fully coupled FSI framework is first proposed in this study to investigate the hydroelastic behaviour of a container ship with a forward speed in regular waves. The results are validated against available co-simulation results and shown in good agreement with the experiments.
- Chapter 6 (A Fully Coupled CFD-DMB Approach on the Ship Hydroelasticity of a Containership in Extreme Wave Conditions) presents an efficient coupled CFD-DMB method for the numerical predictions of nonlinear hydroelastic responses of a ship advancing in calm and extreme wave conditions. The numerical results, including the flexible ship motions, vertical bending moments (VBMs) and green water on-deck, are systematically analysed between the regular and focused wave conditions.

- Chapter 7 (A Hydroelasticity Analysis of a Damaged Ship Based on a Two-Way Coupled CFD-DMB Method) presents a numerical investigation of the hull girder loads on a deformable containership S175 with intact and damaged conditions advancing in regular waves with operating speeds. Two damaged opening scenarios (e.g., damaged tank numbers and tank positions) are evaluated, aiming to explain the mechanism underlying the hydroelasticity of a damaged ship in head seas. A system investigation on the damaged ship motions, resulting hull girder loads and flooding water sloshing phenomenon is presented.
- Chapter 8 (Conclusions and Future Research) discusses how this thesis has contributed to existing knowledge and assesses how well the aims and objectives have been achieved. Suggestions and recommendations are listed for each sub-topic for future research.

2 Critical Review

This chapter presents an overview of the theoretical and numerical methods used to solve seakeeping and hydroelasticity problems for marine vessels. Firstly, historical overviews of the wave-ship interaction and hydroelasticity problems are briefly discussed. Then, the developments of numerical methods of ship global hydroelasticity methods are illustrated. The remaining part of this chapter focuses on a literature survey of specific areas of ship hydroelasticity, including extreme weather conditions and damaged ship conditions.

2.1 Review of Wave-Ship Interaction Problem

Accurate predictions of hydrodynamic loads and corresponding ship motions are of prime importance for the wave-ship interaction problems. Consequently, the theoretical methods of ship motion computations have been under development over the past 70 years. Earlier theoretical prediction methods followed the pioneering works of Korvin-Kroukovsky (1955) based on two-dimensional theories. Various researchers subsequently contributed many 2D strip theory methods of computations. Among these, the most successful and widely applied method is the STF strip theory developed by Salvesen et al. (1970), still widely used by industry. Around the same period, several analytical studies were also undertaken to extend the slender body theory to the seakeeping of slender hulls (Newman 1979).

According to the different treatments of the ship's hydrodynamic disturbance, numerical studies of wave-ship interaction may be categorized into two- or three-dimensional problems to be solved in the time or frequency domain using viscous or inviscid methods. This thesis does not aim to review all these research studies comprehensively. A considerable amount of review papers are available for ship hydrodynamics in the literature, for example, numerical methods on ship applications (Zhang et al. 2006), computational ship hydrodynamics (Stern et al. 2013), loads for use in the design of ships (Hirdaris et al. 2014).

To show a clear path of the numerical approaches on the wave-ship interaction problem, this thesis will start to discuss from inviscid potential flow to viscous CFD method and finally briefly discuss the next generation of meshless particle method.

Numerical research methods are mainly categorized into the finite difference method (FDM), finite volume method (FVM), finite element method (FEM) and boundary element method (BEM). The BEM method provides a solution for potential flow problems with linear or nonlinear free surface and boundary conditions, commonly applied to solve hydrodynamic problems. The BEM method could be categorised by its two characteristics: the boundary element types and boundary integral equations, as shown in Fig. 2.1.

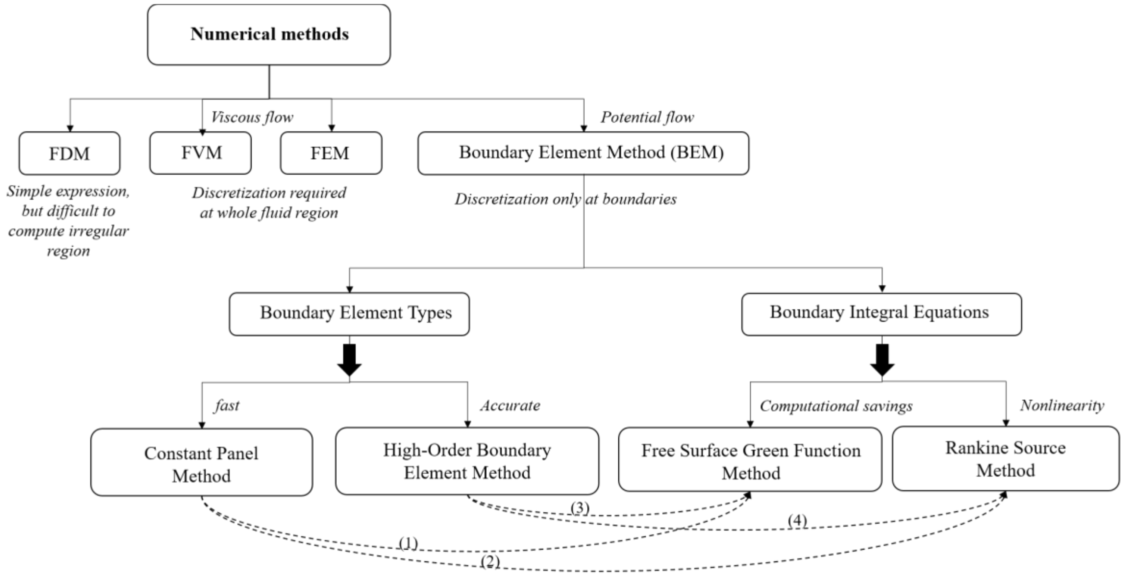

Figure 2.1: The framework of numerical methods in BEM.

Two common boundary element types are the constant panel method and the high-order boundary element method (HOBEM). The constant panel method, which was initially proposed by Hess et al. (1967), has been widely used in hydrodynamic calculations. The constant boundary method divides the surface of the floating body into a quadrilateral or triangular plane panel element, and the values of each point at the panel element are equal to the value at its centre point. However, this method encounters problems with curved surfaces, because the discontinuities occur between units and the interpolation errors can arise.

The HOBEM is commonly adopted for curved surface modelling, which overcomes the limitations of the constant panel method. HOBEM discretises the boundary of the computational domain into the curved surface panel, and the functions between the node values can calculate the value of any point on the panel. Therefore, physical quantities, such as velocity potential, change continuously within the unit. By choosing an appropriate Green's function, the integral area is only on the surface of the floating body, which simplifies the calculation and makes it suitable for solving the problem with the infinite domain. Many scholars have adopted HOBEM to calculate the interaction between waves and floating bodies; for example, Chen et al. (2016) applied HOBEM incorporated with the Rankine source method to solve ship waves in linear and nonlinear approaches. The numerical results, including ship wave drag, sinkage, trim and wave pattern, were all predicted in general good agreement with experimental data. The numerical efficiency and accuracy were two significant advantages of using the HOBEM methods highlighted by the authors. A comparison of the HOBEM and constant panel methods was presented by Liu et al. (1990) for calculating linear hydrodynamic loadings on large floating bodies.

By applying a specific form of Green's theorem, the obtained boundary integral equations are different; two common methods are the free surface Green function method and the Rankine source method. The free surface Green function method is known as reliable for zero-speed problems. The principal advantages of the Rankine Source method are twofold: The Rankine singularity is simple to treat computationally, and the distributed mesh panels at the free surface allow more flexibility with variable coefficients. Nakos et al. (1991) applied a numerical program called SWAN based on a three-dimensional Rankine Panel Method to investigate the seakeeping behaviours of a Wigley ship advancing with forward speeds. The successful agreement of the numerical results upon the prediction of the Kelvin wake and hydrodynamic coefficients was achieved compared to the experimental results. However, as the author pointed that, a drawback of the Rankine-panel method was that it requires more mesh panels compared to other methods, resulting in the computational overhead associated with the solution of the resulting matrix equation.

Later, three-dimensional potential flow theory became widely established, and extensive research has been conducted on the wave-structure interaction problems. Sen (2002) presented 3D time-domain ship motion computations based upon the transient Green function, which extended the work from Lin et al. (1991) for large amplitude motions by considering the exact Froude-Krylov and hydrostatic restoring force. Unlike 2D strip theory-based methods, this fully 3D ship-motion computational scheme provided a significant improvement in determining the occurrences of deck wetness and forefoot emergence.

The potential flow theory provides efficient insight into the initial design stage of shipbuilding; however, it cannot reproduce some critical physical phenomena such as wave breaking and viscous effects. El Moctar et al. (2017) questioned the use of potential flow theory in extreme wave conditions where viscosity effects become critical for modelling large free-surface elevation waves. In contrast, the fully nonlinear computational fluid dynamics (CFD) method solves the Navier-Stokes equation, which accounts for the viscous flow effects and is commonly used as an alternative. CFD has gained high popularity for such predictions due to its low cost compared to the experimental fluid dynamics (EFD) procedures. Until now, CFD has been successfully applied to a wide range of research and engineering problems in many fields of study and industries, including aerodynamics and aerospace analysis, environmental engineering, industrial system design, etc.

Turbulence constitutes one of the most important aspects of CFD modelling, and modelling turbulence is key in obtaining correct and reliable CFD results. Based on the length scale, the turbulence flows can be solved in four methods, as shown in Fig. 2.2: the Direct Numerical simulation (DNS) method, Large Eddy simulation (LES) method, Reynolds Averaged Navier Stokes (RANS) method and Boundary Layer Approximation method.

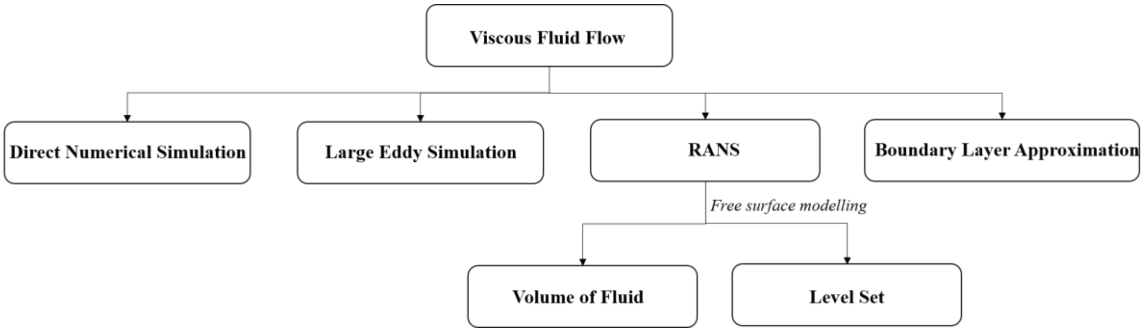

Figure 2.2: A schematic view of the numerical method for the viscous fluid flow modelling.

With regard to the seakeeping behaviour of a ship, the CFD method solves the RANS equations, which are commonly used to investigate ship seakeeping in waves. Extensive research has been proposed and validated the performance of the CFD method in the studies of ship seakeeping performance under different environmental conditions; for example, there were three workshops, held in Gothenburg and Tokyo, every five years, between 2000 to 2015, evaluated the comprehensive CFD methods, i.e., on verification and validation method in 2005 (Larsson et al. 2003), local flow predictions in 2010 (Larsson et al. 2013) and ship resistance and self-propulsion in 2015 (Larsson et al. 2015) of the selected ship models.

Later on, Simonsen et al. (2013) conducted a series of EFD and CFD studies to predict the seakeeping behaviour of KCS containerships in calm water and regular head seas. Comparing the motions and forces from EFD and CFD, they found reasonably good agreement for resistance and dynamic sinkage and trim in calm water. However they observed deviations in the measured ship resistances in wave conditions, which indicated that estimating ship resistance might be difficult in CFD simulations. Demirel et al. (2017) carried out CFD simulations of the roughness effects on the resistance and effective power of the full-scale 3D KRISO Container Ship (KCS) hull. The resulting frictional resistance values of the present study were then compared with the results obtained using the similarity law analysis. In order to ensure the accuracy of the CFD results, in terms of model design should follow the regulations issued by International Towing Tank Conference (ITTC), i.e., practical ship CFD applications (ITTC 2011) and ship resistance (Procedings 2014).

For free surface modelling, the Volume of Fluid (VOF) method (Hirt et al. 1981) is commonly combined with the CFD method to simulate the free surface in the computational domain, which is used in many computer codes, such as ANSYS Fluent, OpenFOAM, STAR-CCM+, etc. Tezdogan et al. (2015) performed a fully nonlinear RANS simulation based on commercial CFD package STAR-CCM+ to predict the ship motions and added resistance of a full-scale KRISO containership, and to estimate the increase in effective power and fuel consumption due to slow steaming. Detailed explanations of the VOF technique adopted in STAR-CCM+ can be found in their paper. The advantage of the VOF method over alternative methods is that as the volumetric data is used to store interface location, conservation of volume is guaranteed (assuming incompressible fluids). Many researchers have extensive studied the use of the CFD-VOF method for seakeeping problems, including coupled ship motions in deep water (Tezdogan et al. 2015, Tezdogan et al. 2016), ship resistance in restricted shallow water (Terziev et al. 2018), ship manoeuvring in irregular waves (Kim et al. 2022), to name a few.

Another commonly used free surface modelling method is the level-set approach, which has been reported to have high computational efficiency; however, there are issues with mass conservation. Hochbaum (2002) presented a two-phase level set method to capture the free surface and coupled it with URANS equations to simulate the flow field around ships. Numerical results, including ship motions and predicted forces and moments on the hull, were presented and compared against experimental data with favourable agreement. Castiglione et al. (2011) predicted the seakeeping characteristics of a high-speed catamaran in a high sea state by the URANS solver CFDSHIP-Iowa V.4. The fluid phase of the code solved the unsteady RANS equations, and the free surface was captured using a single-phase level-set approach (Carrica et al. 2007) and (Carrica et al. 2007). In contrast to the standard level-set method for incompressible flow, the single-phase level set method is only concerned with the solution of the flow field in the water phase. Several advantages of the single-phase level set method against VOF and traditional level set method are that: 1) the interface remained sharp during water propagations, 2) this method reduces the overall computational time by computing simpler equations and 3) this method avoids the problem related to large density ratios in two-phase methods.

The particle method, specifically the SPH (Smoothed Particle Hydrodynamics) method based on the mesh-free Lagrangian principle, is ideally for simulating problems dominated by complex boundary dynamics, such as free surface flows or large boundary displacement. This method is considered the next generation of solving wave-structure problems. It overcomes the numerical challenges of mesh-based CFD which can precisely capture the free surface with fragmentation and reconnection, such as splash and breaking waves.

Several research studies have used the SPH method to solve wave-structure problems. Le Touzé et al. (2010) studied the transient flooding behaviour of an FSPO vessel with intact and damaged conditions in waves using an SPH toolbox called SPH-flow. Their results demonstrated that the SPH method can handle large free surface deformations and showed great potential for future free surface generation. However, the predicted peak amplitudes of the structure were twice larger than the experimental values due to the coarse mesh applied in the model.

Kawamura et al. (2016) presented numerical simulations using SPH solver DualSPHysics, to discuss the capability and accuracy of the SPH method for fishing vessels in severe water-shipping situations. The numerical results, including wave elevations and 6DOFs ship motions, showed favourable agreement with their experiments, except some dependencies were noticed in roll and sway motions. The reason was that the authors suppressed the number of fluid particles to reduce the overall computational burdens. Overall, the particle methods show great potential for future wave-structure modelling; however, they are always associated with substantial computational requirements.

2.2 Historical Overview of Hydroelasticity Methods and Applications

Hydroelasticity is a scientific field that concerned with the deformation of elastic in response to hydrodynamic excitations, depending on elastic deformation. The theory of hydroelasticity was quickly adopted in the marine and ocean engineering section; it may intuitively be assumed that awareness of marine structures experiencing strains and stresses, hence their structural flexibility, has been an accepted fact since it first appeared (Hirdaris et al. 2009).

To concern with the motion of the deformable ship through fluid water, the unified strip-beam theory was creatively used by Bishop et al. (1979) in the analysis of rigid body motion and elastic vibration of monohulls. The fluid effects were predicted by strip theory (Gerritsma et al. 1964), while the generalized modes were composed of the rigid motion modes and the dry modes of the ship structure represented as a non-uniform beam. Price et al. (1985) presented a general three-dimensional hydroelastic theory based on linear potential flow theory and the classical kinematic rigid body boundary condition. This theory can be applied to fixed and moveable marine structures. Gu et al. (1989) presented a time-domain hydroelastic simulation for a monohull to predict the vertical ship motions and bending moments with the considerations of the structure nonlinearity.

They implemented a Timoshenko beam to represent the ship structure, enabling them to estimate the nonlinear responses of an elastic ship under fluid excitations. This method was further applied to evaluate the real-time structural responses of ships in regular or irregular seas. Around the same period, Price et al. (1985) extended its applications to examine the fluid-structure interaction behaviour of non-beam like floating structures, in which the fluid motions were determined by a 3D potential flow theory and the structural modes were obtained by a finite element approach.

The complexity of hydroelasticity theory has led to the adoption on simple geometry for the first several decades. Arai et al. (1997) and Arai (1998) presented a two-dimensional coupled simulation to investigate the hydroelastic impact of a cylinder under severe water impact. The authors applied a CFD method for fluid field analysis, and the structure deformation was solved using a modal representation of a cylindrical shell. The fluid and structure solvers were coupled by including a source term in the fluid continuity equations to account for the deflection of the body. The numerical results compared with experiments for free-drop tests of a cylinder and showed good agreement. Faltinsen (1999) investigated the strains in the longitudinal stiffeners a hull with a wedge-shaped cross-section during the water entry phase. The effect of structural vibrations on the fluid flow was incorporated by solving the 2D Laplace equation with an orthotropic plate theory. The numerical results pointed out that the deadrise angle and impact velocity were of critical importance to hydroelasticity and a function was derived based on the non-dimensionalised of these two values.

Lu et al. (2000) proposed analogous research, which studied the hydroelastic impact of a wedge with a coupled BEM-FEA model for the fluid and structure. The structure was modelled with Euler-beam elements, and the fluid was assumed to be described by a velocity potential that satisfied fully-nonlinear free surface boundary conditions.

Later, Faltinsen (2000) proposed a thorough survey on theoretical, numerical and experimental studies for water-impact problems in ocean engineering field. The conclusions from this article allowed one to determine when the hydroelasticity is important and also provided a summary of the important parameters in ship hydroelasticity field, i.e., the geometric properties of the structure, the impact velocity, and the relative angle between the water and the structure. Maki et al. (2011) extended the hydroelastic method proposed by Paik et al. (2009) to investigate the hydroelastic impact of a wedge-shaped body onto a calm free surface. The one-way transfer was applied to predict the stress field on the fluid–structure interface due to rigid-body impact.

The evolution of naval architecture, combined with advancements in computational technology, has led to the application of a wide range of hydroelasticity methods in more complex marine structures. As examples shown in Fig 2.3, ship structure modelling (Paik et al. 2009) (Jiao et al. 2021) (Lakshmynarayanana et al. 2020) (Wei et al. 2022), offshore floating wind turbine (Karimirad et al. 2011) (Liu et al. 2019), large floating FPSO, VLFS in severe environment (Kashiwagi 2000) (Watanabe et al. 2004). The common feature of these structures is that they are large in dimensions, especially for some floating structures, i.e., VLFS, which own large ratio in its length-width to the thickness direction, and the hydroelastic effects become prime important when the horizontal scale of the wavelength relative to the structure is small. Hydroelasticity theory further applied to investigate the vibrations of rotating marine propeller with Dhinesh et al. (2010) (Abbas et al. 2015) (Chen et al. 2019) or without ship hull effects (Li et al. 2017) (Lin et al. 1996) (He et al. 2012), to name a few.

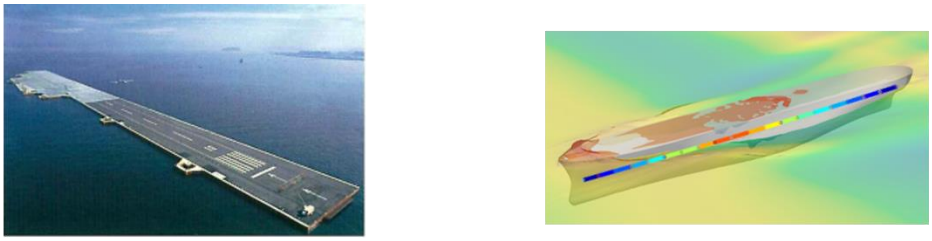

(a) Mega floater in Tokyo Bay

(b) S175 type of containership

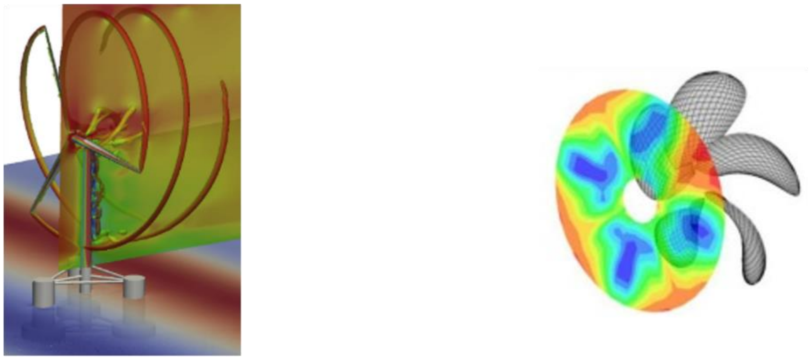

(c) Semi-submersible Floating wind turbine OC4

(d) Marine propeller 4119

Figure 2.3: A serial research of hydroelasticity on various marine applications: (a) Mega floater in Tokyo Bay (Kashiwagi 2000), (b) S175 type of containership (Wei et al. 2022), (c) Semi-submersible floating wind turbine (Liu et al. 2019), (d) Marine propeller 4119 (Chen et al. 2019).

2.3 Global Vessel Hydroelastic Response

Commercial vessels tend to increase their dimensions to meet the fast development of transportation and operations. An increase in ship size tends to make the hull more “flexible” and leads to the wave encounter frequency being closer to the ship’s wetted natural frequency. In such resonance frequency, comparatively small vibration-induced loads are superposed to the wave-induced load that may significantly violate the ship motions and deform the ship structure. This phenomenon is called the ship’s global hydroelastic effect, which is of particular importance in the determination of design wave loads and structure strength evaluation of large ships (Hirdaris et al. 2014).

Hydroelastic response of ship hulls can be categorised twofold: springing and whipping. Springing is a resonance phenomenon where the excitation encounter frequency matches the ship’s structural frequency (usually the first bending mode). Whipping describes a type of ringing phenomenon when a transient hull vibration is induced by local section slamming.

The prediction of vibration loads on a deformable ship is challenging due to the strongly nonlinear free surface and the structure elastic behaviour. In such cases, the deformed ship structure interacts with the surrounding flow fields, which form a fully coupled fluid-structure-interaction (FSI) system against the traditional rigid ship assumption. Hirdaris et al. (2009), Jiao et al. (2021) and Bakti et al. (2021) also supported this point of view, showing that the rigid body model may lead to inaccurate predictions of hydrodynamic loadings as well as the global ship motions. Therefore, a fully coupled fluid-structure interaction (FSI) approach was recommended to apply in the studies of predicting the flexible ship motions and hydrodynamics loads of ship under environmental excitations.

Over the past decade, the theoretical and numerical methods for predicting ship seakeeping performance based on hydroelasticity theory have gained momentum. To account for both fluid and structural features, the partitioned approach was adopted most commonly, in which the wave-structure system was divided into the fluid and structure parts and solved iteratively. Another numerical method against is called the monolithic approach, which solved the whole fluid and structure equations together. A persisting discussion is, whether the monolith or the partitioned coupling approach is preferable. Here listed the advantages and drawbacks of both methods:

Partitioned VS monolithic

- The monolithic approach is usually said to be able to handle a higher amount of coupling instabilities (Bungartz et al. 2016)

- In test scenario comparisons, it has been shown that the monolithic approach is more computationally efficient when a high amount of interaction is present, although not by orders of magnitude.
- For weak interactions between fluid and structure, the partitioned approach is widely believed to be more efficient than the monolithic approach.
- The partitioned approach is said to offer more flexibility with respect to the physical models and the numerical schemes employed. Certain mismatches such as different time scales can be taken into account easier in the partitioned approach than in the monolithic approach.
- The monolithic approach has the potential to reduce the amount of methods and schemes involved which results in a lower numerical and technical complexity and a lower amount of instabilities arising from the coupling.

In general, ship hydroelasticity problems are types of weak interaction, the partitioned approach owns flexibility and efficiency, which is the optimum choice to adapt. The partitioned approach may origin from the pioneering work of Bishop et al. (1979). In their book, the authors first developed a linear fluid-structure-interaction model on the basis of 2D potential flow theory and a linear beam model to investigate the rigid and flexible behaviour of a monohull in waves. Within this framework, the flexible structural characteristics of the ship were idealised as an elastic beam and interacted with the fluid forces. The theory was subsequently extended by Bishop et al. (1986) to a generalised beam model for floating vehicles or more complicated shapes. The three-dimensional hydroelasticity theory was established in the early 1980s by Bishop et al. (1986), since then a great deal of process has been made in the development and applications of the hydroelasticity analysis on ship structures based on the potential theory. A road map of the development of ship hydroelasticity in partitioned approach is prepared in Fig 2.4.

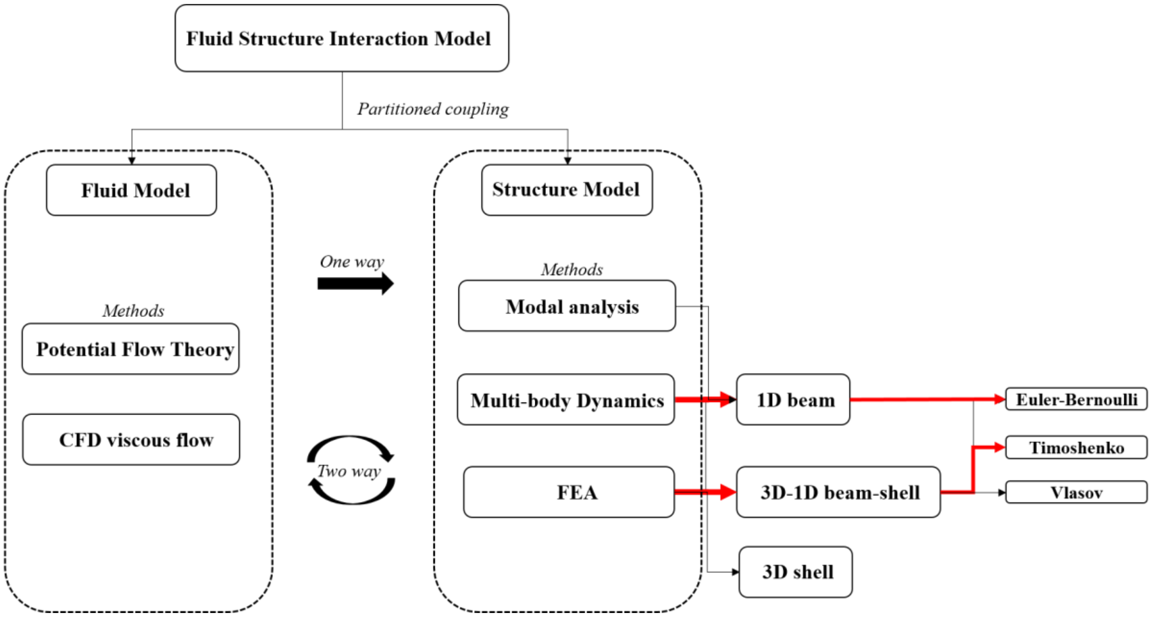

Figure 2.4: A schematic diagram for the partitioned method of FSI method.

Senjanović et al. (2008) proposed a partitioned approach for hydroelastic analysis of a flexible segmented barge in waves. In their FSI approach, a 3D potential flow code based on the radiation–diffraction theory (Salvesen et al. 1970) was coupled with a 3D FEM structural model. The numerical results for barge responses and distortion in waves have been examined based on their model experiments Senjanović et al. (2009). Kim et al. (2014) carried out ship springing and whipping analysis using a coupled method, in which the fluid flow was solved by 3D Rankine panel method and the structure deformation was considered based on a 3D-1D shell-beam structural. The proposed structure model consisted of two parts, the shell elements for ship wet surface modelling and the beam model was a classical idealization of the ship structure. The eigenvalue analysis of the beam model was required in prior to examine the performance of the selected beam theory to represent the real ship behaviour.

Later on, the fully nonlinear CFD method solves the RANS equations, was adopted to investigate ship hydroelasticity in seaways by coupling with a structure solver to study the dynamic responses of a flexible ship on a free surface. The external fluid pressure exported from the CFD simulation is used to derive the structural responses in the structure solver, and the structural deformations are fed back into the CFD solver to deform the mesh.

In some cases, CFD and the finite element analysis (FEA) are coupled for the hydroelastic simulations based on a one-way coupling approach (Lakshmynarayanana et al. 2020) or a two-way coupling approach (Jiao et al. 2021). The main difference between one-way and two-way coupling methods on ship wave loads and hydroelastic responses was the consideration of added mass effects. Lakshmynarayanana et al. (2020) and Takami et al. (2019) investigated the influences of one/two way algorithm on ship hydroelasticity based on a commercial co-simulation interface (Star-CCM+ & ABAQUS). Based on their suggestions, the one-way coupling approach may not be appropriate for the studies of the springing and whipping because the added mass effects in the elastic deformation need to be accounted, and it may result in an underestimate of the high vibratory components and wave loads. As summarised above, a two-way coupling algorithm is the most appropriate method for ship hydroelasticity studies in the partitioned coupling approach due to the strong interaction between elastic bodies and free surface.

Generally, a two-way algorithm can be further divided into a two-way strong and a two-way loose coupling method. The two-way strong coupling method, indicated by Benra et al. (2011), has the second-order's convergence rate, suitably designed for FSI problems with a strong dependence between fluid and structure. Such a two-way strong coupling method has been applied for the flexible ship seakeeping problem by using the commercial co-simulation interface (Star-CCM+ & ABAQUS) or open-source coupling library PreCICE (Bungartz et al. 2016). In contrast, the two-way loose coupling method owns a light and efficient data communication scheme with acceptable tolerance and accuracy. A detailed explanation on the algorithm perspective of two-way strong and loose coupled methods was presented in later Chapter 3.3.1 and 3.3.2.

The demonstration of the ship hydroelasticity in structure solver can be categorized into three types in FEA, the pure-beam model, the beam-shell model and the full-ship model, as shown in Fig. 2.5.

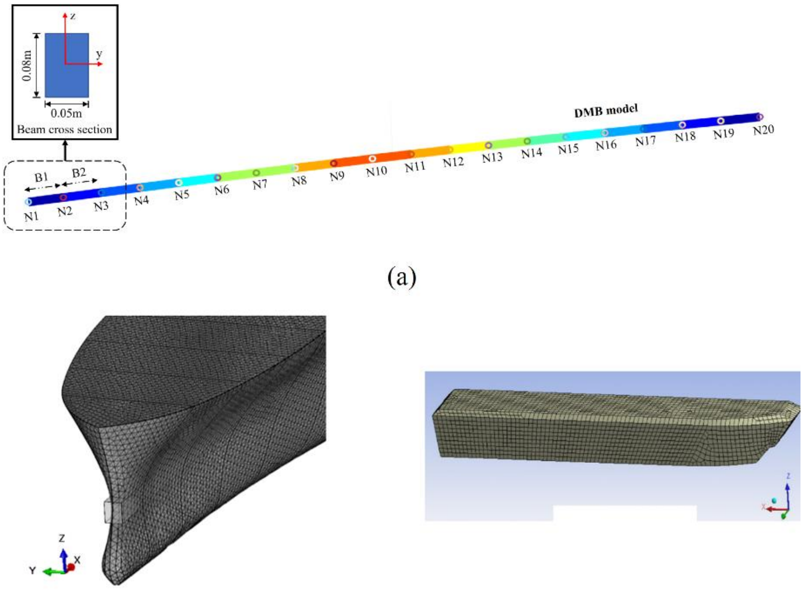

(a)

(b)

(c)

Figure 2.5: Examples of three types of structural modelling: (a) Pure-beam model (Wei et al. 2022), (b) Shell-beam model (Wei et al. 2022), (c) Full-ship model (Ma et al. 2012).

The pure-beam model (1D beam) was designed based on the beam theory, i.e., Euler-Bernoulli beam or a Timoshenko beam, in which the ship's elastic deformations were computed by solving the beam equation of motions and external forces. El Moctar et al. (2017) proposed a study based on the Timoshenko beam model coupled with a CFD model by a two-way coupling method to investigate the wave-induced structural loads of three containerships in regular and deterministic wave sequences. Their numerical results, including the dynamics loads and structural vibrations, agreed well with the experiments, which assessed the feasibility of using the beam model and transient RANS solver to obtain the short-term statistical measures of nonlinear ship responses.

Second, the beam-shell model (1D-3D beam-shell) requires a more complex design in FEA, in which the ship geometrical models in the CFD and FEA solvers should be topologically equal. The wet hull surface is generated using the shell elements and kinematically constrained with the beam nodes. Prior to the FSI simulations, the structural modal analysis has to be applied to calibrate the beam profiles (Jiao et al. 2021, Jiao et al. 2021). Such an FEA model was coupled with a CFD solver based on a two-way coupling approach through a co-simulation interface (Star-CCM+ & ABAQUS) by Lakshmynarayanana et al. (2019), Lakshmynarayanana et al. (2020) and Jiao et al. (2021) to predict the motions, wave loads, and hydroelastic vibrations of an S175 containership in waves with forward speeds. Their results, including global ship motions and vertical bending moments in different regular wave conditions, were comprehensively analysed and validated with the existing experimental results (Chen et al. 2001).

The third method is the full-ship model (2D shell), which discretises the whole ship and substructure using the shell finite elements in the FEA software. This method is capable of accounting for the complex deformation behaviours of the ship and predicting local stress distributions; however, it is computationally very demanding. Ma et al. (2012) modelled the full ship with sandwich composite material using ANSYS and coupled it with CFX through the ANSYS workbench. Their FSI results were further studied with stress analysis, which revealed that the most vulnerable region in the sandwich plate structure was the core-skin interface near the girder.

A comparison among three different ship structural modelling (1D beam, 1D-3D beam-shell and 2D shell) was presented by Hirdaris et al. (2003) on a bulk carrier in wave conditions with different headings. According to the author's results, all three structural models produced results that were close to each other in vertical motions and symmetric loadings. However, the deviations arise in the antisymmetric plane; specifically, the differences were noticed from the torsional moments between the results produced by the 2D shell and 1D-3D structural idealizations. The reason may arise from the beam warping effects induced by the torsional moments, resulting in the Timoshenko's beam theory which is inadequate in simulating the antisymmetric deformations for a slender thin-wall hull.

The above-mentioned CFD-FEA coupling method requires significant computational efforts (Lakshmynarayanana et al. 2019, Bakti et al. 2021), making extending applications to more complex wave conditions difficult. Recently, a CFD-DMB method was proposed by Lu et al. (2016) in the investigation of the hydroelastic behaviour of large VLFs. The DMB model has a similar set-up to the traditional hydroelastic experiments. In this approach, the ship hull is divided into multiple floating rigid segments, while a stiffness matrix based on a Euler-Bernoulli (EB) beam theory, equivalently representing the structure's stiffness, is employed to connect ship neighbouring sections. In this method, only a one-dimensional beam is modelled in the structural solver and it can significantly save computational efforts compared to the coupled CFD-FEA method. Based on the above design, the dynamic motions of the ship are both affected by the hydrodynamic forces from fluid solver and restricted by the deformation conditions of the equivalent beam properties from the structural solver.

The CFD-DMB coupling approach has been applied successfully in the literature, for example, in flexible wind turbine blades (Liu et al. 2019) and aircraft wings (Tamer 2021). However, in these applications, a single-phase solver was applied to calculate the air forces at the geometry surface with a low mass ratio. For multiphase cases, the DMB method has been successfully employed by Li et al. (2022) on the dynamic motion of a close-loop WEC array in waves. Lu et al. (2016)

investigated the hydroelasticity of very large floating structures (VLFs) in waves which were solved in both frequency (Wei et al. 2017) and time domains (Wei et al. 2018). In addition, Zhang et al. (2018) extended its application for a flexible marine structure with complex geometric features by means of FEM simulation, the structural stiffness matrix was calculated from the standard finite element method and converted to the equivalent beam stiffness using a static condensation technique and rigid-body-motion transformation matrix. Their results, including structural deformations and internal loadings showed favourable agreement with the results from experiments (Yago et al. 1996). Recently, Bakti et al. (2021) studied the forward speed effects on the elastic responses of an analytical Wigley hull by using a BEM-DMB coupling method in both regular and irregular waves. Their results showed that a noticeable increase of ship vertical bending moments occurs when the ship speed increases due to the whipping phenomenon.

2.4 Ship Hydroelasticity in Focused Waves

Ships can experience slamming impacts while operating at high speeds, in severe sea states, or both. Severe slamming events can result in enormous local impact pressure and hull girder global whipping responses, which is critical for the ultimate strength evaluation of a ship structure. El Moctar et al. (2017) presented a statistical report from the International Union of Marine Insurance (Seltmann et al. 2015) that approximately 36% of ship losses of all total losses between 2001 to 2015, were associated with ships encountering harsh weather.

In a realistic sea state, the slamming event is a highly random process. Concerning the extreme load prediction and fatigue evaluations, attention shall be paid to more than just the deterministic load cases and also to short-term and long-term statistical properties of the events. Most of the long-term statistical properties can be obtained from short-term statistics.

The extreme value analysis and fatigue predictions during a ship's lifetime require a correct physical (hydrodynamic) model of the ship's behaviour in severe sea states, a proper stochastic characterization of the ocean waves and proper probability and stochastic theories, taking into account the nonlinear effects. The flow around a ship in extreme seas is characterized by high nonlinearities, wave breaking, air trapping, etc. Navier Stokes-Equations are better suited to describe these physical phenomena.

The irregular wave model has been developed and validated in CFD for many years. Elangovan (2011) simulated irregular waves based on a flap-type wave maker, and the wave data was derived from the Bretschneider wave spectrum (PM). The predicted wave elevations were processed for FFT analysis and validated with the selected ocean spectrum with a favourable agreement. Based on CFD and potential flow theory, Baquet et al. (2017) simulated a fully nonlinear, steep and irregular wave field of three-hour duration. The authors pointed out that the significant wave heights from the long-time CFD simulations were lower than the target wave due to the energy loss. Therefore, energy compensation methods were required to improve the simulation accuracy. Romanowski et al. (2019) proposed a methodology to determine the mesh grid and time step sizes for completely unknown irregular seas. This served for practical CFD analyses and avoided reworking the simulation. A pre-processing procedure was required to decompose an irregular sea into multi-regular components. Then, the regular wave elevations were imported to StarCCM+ for irregular sea generation corresponding to defined limits. Based on a series of uncertainty and validation studies, the numerical results achieved a level of accuracy that satisfied the simulation time error and other mesh errors.

The irregular wave procedure can be applied not only to simulate real sea conditions, but also to predict ship motion responses in waves by spectral analysis. Shen et al. (2014) presented numerical prediction of ship motion responses based on an efficient irregular wave generation procedure in OpenFOAM, in which the irregular waves were generated by a white noise spectrum with the superposition of a set of linear waves. Three monohull models with five irregular wave conditions have been performed to validate the presented methods with good agreement. Seakeeping analysis of a waterjet-propelled trimaran in short-crested irregular wave conditions was carried out by Zhang et al. (2021) in a viscous CFD-based method, which took the fully nonlinear and viscous effects into account. The irregular wave system was generated by superimposing a plurality of micro-simple harmonics with different frequencies, amplitudes, directions and random phases. Kim et al. (2022) presented ship manoeuvrability studies of a containership navigating irregular wave conditions based on a fully nonlinear RANS model. The long-crested irregular seas were generated by deriving the JONSWAP spectrum with a significant wave height of 5m and a peak period of 12.4s in full scale.

Most of the above-mentioned literature focused on ship seakeeping behaviours in irregular waves were presented based on a rigid ship assumption, in which the ship hydroelasticity is not considered. In order to predict ship longitudinal moments in extreme conditions, it is essential to consider the nonlinear and hydroelastic effect in a unified analysis containing both the rigid body motion and the elastic vibration of ships responding to waves because the hydrodynamic loads depend not only on the ship's rigid motion.

Several pieces of research in literature applied nonlinear FSI methods for the hydroelastric effects of the ship in extreme seas. El Moctar et al. (2017) presented a coupled FSI method to assess slamming-induced hull whipping on sectional loads of ships in regular and irregular waves. The fluid solver solved the Reynolds-averaged Navier-Stokes (RANS) equations coupled with the nonlinear structure solver to account for the ship's elastic deformation under the wave excitations. The short-crested waves were generated according to the concept of the Most Likely Response Wave WLRW (Dietz 2005). The authors compared the midship vertical bending moments of ship in an MLRW sequence among three different numerical approaches: the BEM, CFD rigid and FSI model, which found that the FSI model was most appropriate of capturing the high nonlinear results and the peak hogging moments were 15% higher when compared to rigid ship model. Similar research was carried out by Takami et al. (2020) to predict the extreme value distribution of the vertical bending moment of a containership in a given short-term sea state. Irregular wave events were tailored by which the most probable wave episodes (MPWEs). To predict the extreme value distribution of the VBM, the co-simulation interface coupled CFD and FEA were adopted to provide high-fidelity numerical solutions.

The direct long-term FSI simulations covering the entire ship's life are unrealistic; therefore, most of the ship hydroelasticity research was presented in regular wave assumptions. However, regular waves are unrepresentative of actual extreme events, as stated by Ning et al. (2009) and cannot represent the most severe conditions. The focused wave theory is used as an alternative overcome the above issue for a long-term irregular wave modelling. The concept of the focused wave was first proposed by Davis et al. (1966) by modulation of a series of conventional sinusoidal wave trains generated from a prescribed wave spectrum and superimposing the crests. Since then, experiments and numerical investigations have been carried out using the focused wave groups to replace the irregular waves in the nonlinear wave-wave interaction studies. For example, Baldock et al. (1996) created wave focus events through the superposition of regular wave trains based on the linear wave theory and investigated the effects of nonlinearity of wave-wave interactions. Ning et al. (2009) studied the propagation of the focused wave groups with different incident wave parameters and compared the solutions between the first- and second-order wave theory.

The focused wave theory has been adopted to investigate the wave-structure problems and predict the extreme loads on offshore structures. These studies were initially focused on a simple floater (Gao et al. 2016), and then extended to complex floating structures, such as wave energy converters (WECs) (Draycott et al. 2019) or semi-submersible wind turbine foundation (Bredmose et al. 2010, Zhou et al. 2019). Zhou et al. (2019), Zhou et al. (2021) further extended their applications of studying the dynamic motions of a fully coupled aero-hydro-moored of FOWT subject to focused wave conditions. Recently, (Wei et al. 2022)presented a fully coupled approach between CFD and

DMB method for the numerical prediction of nonlinear hydroelastic responses of a ship advancing in regular and focused wave conditions. The authors founded that the focused wave case will lead to an increase of the longitudinal responses of the hull compared to regular wave condition, i.e., the heave, pitch and total VBMs rise about 25%, 20% and 9%, respectively. In focused wave conditions, intensive ship responses and severe waves cause stronger slamming phenomena. It is found that the instantaneous impact pressure from the focused wave is higher and sharper compared to the regular waves and comes along with the obvious green water on deck phenomena.

2.5 Damaged Ship Hydroelasticity in Waves

One area that has become of great concern to ships' design and operation is the influences of accidental damages on seakeeping behaviour with the considerations of ship hydroelasticity. Despite many efforts to improve the structural design of ships over the years, serious damage to ship hulls continues to occur due to collision and grounding and excessive loading. According to the statistical data from Lloyd's Register (Lloyd's_Register 1996), a total of 76 ships were lost due to damage by collision, which occupied about 43% of the total loss, between 1991 and 1995. In recent years, two serious accidents occurred due to the failure of the hull structure, MSC NAPOLI in 2007 and MOL COMFORT in 2013, as shown in Fig. 2.6. It was reported that both vessels were broken due to the large hogging of the hull structure.

(a) (b)

Figure 2.6: Two major accidents in recent years (Sun et al. 2021): (a) MSC NAPOLI, (b) MOL COMFORT.

The prediction of damaged survivability is challenging, since the damage openings at hull surface not only lead to flooding, but also reduce the local structural integrity. In such circumstances, ships may easily be excited by the inner and outer fluid loads. This forms a complex coupled system. The traditional rigid-body assumption may lead to the inaccurate prediction of hydrodynamic loadings as well as the resulting ship motions. Therefore, a coupled Fluid-Structure-Interaction (FSI) method to predict the correct dynamic motion and hydroelastic responses of a containership in waves will have to be used for accurate load and response predictions.

The damage openings on a ship hull occur frequently during ship-to-ship collisions. Seawater floods into the damage compartment, which may result in sloshing which poses a serious risk to the ship's stability with a risk for capsize (Manderbacka et al. 2019). This mechanism may become more complicated when the ship sails in waves.

In order to investigate the phenomenon of flooding flow into a damaged compartment of a ship, a series of model experiments were performed accordingly. Ćatipović et al. (2018) obtained results from their model experiments and found that the wave-induced vertical motions (e.g., heave and pitch) of a damaged ship model were generally greater than that for an intact ship. In order to predict the stability of damaged ships, the nonlinear interaction between the water in the flooded compartment and ship motions has to be considered (Gao et al. 2013). Siddiqui et al. (2020) presented the results of a series of experimental studies of a 2D damage hull section in waves systemically investigating the effects of wave parameters, damage compartment size and its opening sizes. Their results confirmed that for a floating damaged section in waves, the floodwater behaviour was highly coupled with body motions, and the overall behaviour was very different as compared to the intact condition.

Parallel with the experimental investigations, numerical simulations were developed to predict the dynamics of flooding water and damaged ship responses. Modified empirical Bernoulli equations were used to evaluate the flow rate through the opening. In addition, the lumped mass method (Manderbacka et al. 2015), shallow water theory (Santos et al. 2008) and MPS method (Hashimoto et al. 2017) were developed to predict the transient behaviour of damaged ship sections or ships associated with flooding. Subsequently, a fully nonlinear computational fluid dynamics method (Gao et al. 2013, Gao et al. 2015, Gao et al. 2021) was developed to improve the floodwater motions by considering the energy transaction between the water inside and outside the damaged compartment as well as the coupled effects between the damaged ship motions and fluid motions inside the damaged tanks.

Another important concern of a damaged ship is the reduction of its structural strength due to the loss of load-carrying structural elements. In such circumstances, the damaged ship may be more vulnerable to lose its structural integrity due to the environmental loads. The seawater dynamics in a damaged compartment significantly changes the load distribution on a ship hull in longitudinal direction, which greatly affects not only the still-water bending moment (S_VBMs), but also the wave-induced bending moment (W_VBMs) (Lee et al. 2012, Mikulić et al. 2018).

There has been a great deal of research devoted to investigate the influences of damaged ships on the W_VBMs. For example, Chan et al. (2003) proposed a nonlinear time-domain simulation to predict the dynamic structural loads on a Ro-Ro ship in regular waves in intact and damaged conditions. The authors obtained higher global wave loads and VBMs for a damaged ship than those evaluated for intact conditions. Fols∅ et al. (2008) and Lee et al. (2012) presented different linear methods for numerical simulations on a damaged oil tanker and warship. Their results confirmed that the magnitudes of W_VBM for damaged ship conditions were about 11 % - 15% greater than intact ship in heading seas. Begovic et al. (2017) conducted experimental investigations of hull girder loads on an intact and damaged naval ship DTMB5415 at zero speed in both head and beam regular waves. The researchers reported that the vertical shear force (VSF) and VBM values are significantly larger for the damaged ship in heading waves, with an approximate 10% increase compared to the intact ship in the whole wave range tested. Similar experimental studies were conducted by Ćatipović et al. (2018), reporting a 28% increase in W_VBMs of the damaged ship compared to the intact ship. Mikulić et al. (2018) proposed an efficient method to evaluate the vertical bending moment of a damaged ship in different wave directions through an in-house MATLAB code, and the hydrodynamic forces were calculated using WAMIT. The authors concluded that the wave-induced VBM of the damaged ship was generally larger than that of the intact ship, especially for stern-quartering waves.

Based on the above statements, even if the ship has survived the damage from the perspective of stability, it can still suffer from the risk of increased longitudinal W_VBM of the hull girder (Begovic et al. 2013). The enlarged vertical loads on the hull girder may further lead to secondary damages, i.e., deformations or even collapses. Under these circumstances, it is important to estimate the correct W_VBMs of a damaged ship with the considerations of the ship hull elasticity and flooding water dynamics as suggested by the Soares et al. (2009).

Recently, Wei et al. (2022) presented numerical investigations of the hull girder loads on a flexible containership S175 with intact and damaged conditions advancing in regular waves with forward speeds based on a fully coupled CFD-DMB method. The obtained numerical results show that the damaged ship experiences less vertical motions but greater global wave loads than the intact ship. This paper also demonstrated that ship damages greatly influence the hull girder vertical bending moments (VBMs), while water VBM is very sensitive to the added weight from flooding water. In specific ship-damage conditions, local hogging moments at several amidship sections exceeded the international regulation limits. Therefore, a new safety factor was recommended to fulfil the over-limited hogging moments of damaged ships.

2.6 Concluding Remarks

Until this point, a broad literature review has been done on existing hydroelasticity methods and related topics, which will be covered in the following chapters of this thesis. During this literature review, the following gaps in the literature have been detected:

- No FSI studies have successfully implemented a two-way weak algorithm for ship hydroelasticity problems.
- No study has developed a CFD-FEA or CFD-DMB framework for ship hydroelasticity problems based on a repeatable, free and open-source software framework.
- No study has looked into the extreme effects of ship hydroelasticity based on a New-wave theory.
- No study was investigated the ship hydroelasticity in extreme wave conditions by combining a transient FSI simulation and the focused wave theory.
- No study has been performed on the influences of the damaged openings on the ship seakeeping behaviours with the consideration of hydroelasticity based on a transient FSI model.

The following main chapters of this thesis aim to fill these gaps listed above, using the state-of-the-art coupled methodologies: CFD-FEA or CFD-DMB.

3 Numerical Methods

In the outline of this chapter, first, the physical principals of the selected fluid and structure solvers are explained with derived formulations. Then, two coupling FSI frameworks: CFD-FEA (FSI1) and CFD-DMB methods (FSI2), are presented separately, and the differences are discussed. Inside each FSI framework, OpenFOAM is utilised as the CFD solver and coupled with structural solvers (i.e., Calculix or MBDyn) through different coupling schemes. A schematic view of the coupling approaches is prepared in Fig. 3.1 to help understand the commonalities and differences between these two frameworks, where the CFD-FEA coupling framework is indicated in black, and the CFD-DMB coupling framework is shown in blue.

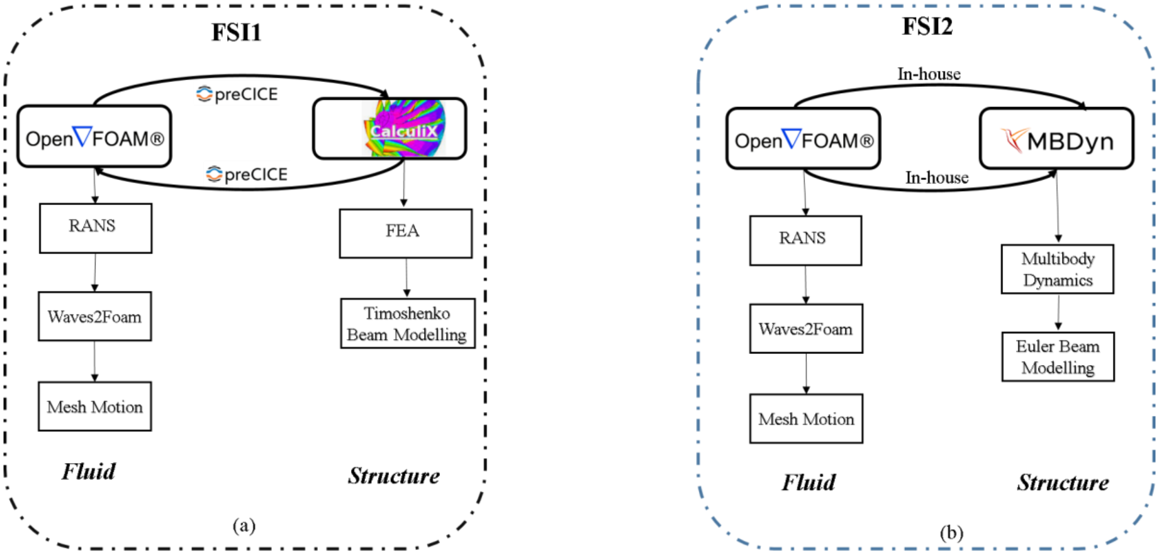

Figure 3.1: A schematic view of the proposed two FSI frameworks in this study.

3.1 Fluid Flow Modelling

The open-source CFD toolbox OpenFOAM is applied to model the fluid field by solving the nonlinear RANS equations using an FVM method using the multi-phase solver interFoam.

3.1.1 Governing equations of flow field

The fluid flow around the ship is assumed to be transient, incompressible and viscous, which is governed by the continuity and momentum equations as given below:

$$\nabla \cdot U = 0 \tag{3.1}$$

$$\frac{\partial \rho U}{\partial t} + \nabla \cdot \left(\rho\left(U - U_g\right)\right) = -\nabla P_d - g \cdot x \nabla \rho + \nabla(\mu_{eff} \nabla \mathrm{U}) + (\nabla \mathrm{U}) \cdot \mu_{eff} + f_\sigma \tag{3.2}$$

where U refers to the velocity of flow field, ρ is the mixed density of water and air, g is the gravity acceleration, P_d refers to the dynamic pressure, μ_{eff} is the effective dynamic viscosity, f_σ is the surface tension which is only considered at the free surface.

The Volume of Fluid (VOF) method (Hirt et al. 1981) is adopted to simulate the free surface in the numerical domain by solving an additional transport equation for the scalar quantity, a, which represents the volume fraction of fluid for each cells.

$$\frac{\partial a}{\partial t} + \nabla \cdot [(U - U_g)]a] + \nabla \cdot [U_r(1-a)a] = 0 \tag{3.3}$$

where U_r is the artificial compressive velocity which only functions near the free surface due to the inclusion of $(1-a)a$.

For a two-phase flow problem, the volume fraction of each phase is used as the weighting factor to calculate the mixture properties. The equations for the density and the viscosity can be expressed by:

$$\rho = a\rho_w + (1-a)\rho_a \tag{3.4}$$

$$\mu = a\mu_w + (1-a)\mu_a \tag{3.5}$$

where, subscripts w and a represent the water and air phases, respectively.

To reduce numerical smearing and sustain a sharp interface between water and air, OpenFoam specially adds an artificial compression term $U_r(1-a)a$ (the third term in Eq.3 Weller (2002), where U_r is the artificial compressive velocity which only functions near the free surface due to the inclusion of $(1-a)a$.

3.1.2 Turbulence modelling

While modelling ships sails in oceans, Reynolds number of fluid field surrounding the ship may rise to 10^7 and the fluid flow is fully turbulent. In CFD simulations, the model scale ship is considered, but the Reynolds number is around 10^5, which means that turbulence effects should be taken into account. The turbulent flow contains unsteady vortices, which leads to fluctuation changes of the pressure/velocity and certain dissipation of kinetic energy. Thus, it is of great importance to account for the turbulence effect in computational models by applying appropriate turbulent models.

The $k-\omega$ SST turbulence model is applied for turbulence modelling, which is widely adopted in industry. This turbulence model combines the advanced features of applying the standard $k-\omega$ model near the boundary layer and switching to the standard $k-\epsilon$ model in the far-field. The governing equations for the turbulent kinetic energy k and the specific dissipation rate ω are defined as follows:

$$\frac{\partial\rho k}{\partial t} + \nabla\cdot(\rho \mathrm{U} k) = \nabla\cdot(\Gamma_k \nabla k) + \check{P}_k - D_k \tag{3.6}$$

$$\frac{\partial\rho\omega}{\partial t} + \nabla\cdot(\rho \mathrm{U} \omega) = \nabla\cdot(\Gamma_\omega \nabla \omega) + P_\omega - D_\omega + Y_\omega \tag{3.7}$$

$$\Gamma_k = \mu + \alpha_k \mu_t \tag{3.8}$$

$$\Gamma_\omega = \mu + \alpha_\omega \mu_t \tag{3.9}$$

where Γ_k and Γ_ω denote as the effective diffusivity of the turbulent kinetic energy k and the specific dissipation rate ω, respectively; $\check{P}_k$ and P_ω represents the turbulence production terms while D_k and D_ω are the dissipation terms; Y_ω is the cross-diffusion term; μ and μ_t are the dynamic and turbulent viscosity; α_k and α_ω are the turbulent coefficients which blended by a blending function F_1 ,

$$\phi = F_1\phi_\omega + (1 - F_1)\phi_\epsilon \tag{3.10}$$

The blending function F_1 is also used to blend between the empirical constants, when $F_1 = 1$ means inside the boundary layer and $F_1 = 0$ is in the free stream; arg_1 depends on the distance from the field point to the closest wall d.

$$F_1 = \tanh\,(arg_1^4) \tag{3.11}$$

$$arg_1 = \min\left[\max\left(\frac{\sqrt{k}}{\beta^*\omega d}, \frac{500\nu}{d^2\omega}\right), \frac{4\rho\alpha_{w2}k}{CD_{kw}^{+}d^2}\right] \tag{3.12}$$

where ϕ_ω and ϕ_ϵ are the model constant in the $k-\omega$ (e.g., β^*) and $k-\epsilon$ model (e.g., C_μ), respectively.

The blending function F_1 is to combine $k-\omega$ and $k-\epsilon$ which forming $k-\omega$ B(Baseline)ST model, however, Menter (1994) pointed out the wall shear stress is over predicted at this stage. Therefore, a viscosity limiter μ_t is introduced to extend the $k-\omega$ BST model to $k-\omega$ SST model.

$$\underbrace{\mu_t = \frac{\rho k}{\omega}}_{\text{BST } model} \qquad \underbrace{\mu_t = \frac{\rho\alpha_1 k}{\max\,(\alpha_1\omega, SF_2)}}_{\text{SST } model} \tag{3.13}$$

where S denotes as the strain rate magnitude $S = \sqrt{2S_{ij}S_{ji}}$ and F_2 is another blending functions $F_2 = \tanh\,(arg_2^2)$, and $arg_2 = \max\,(\frac{2\sqrt{k}}{\beta^*\omega d}, \frac{500\nu}{d^2\omega})$.

The default model coefficients of the $k-\omega$ SST model implemented in OpenFOAM is listed in Table 3.1.

Table 3.1: Coefficients for the $k-\omega\ SST$ turbulence model.

α_{k1}	α_{k2}	$\alpha_{\omega 1}$	$\alpha_{\omega 2}$	β_1	β_2	γ_1	γ_2	β^*	α_1	b_1	c_1
0.85	1.0	0.5	0.856	0.075	0.0828	0.556	0.44	0.09	0.31	1.0	10.0

The boundary inlet turbulent parameters were calculated and assigned at the initial condition with the following equations:

$$k=\frac{3}{2}(I\left|u_{ref}\right|)^2 \tag{3.14}$$

$$\omega=\frac{\sqrt{k}}{C_\mu^{1/4}\cdot L} \tag{3.15}$$

$$V_T=\sqrt{\frac{3}{2}}\cdot u_{ref}\cdot I\cdot l \tag{3.16}$$

where I denotes the turbulence intensity $I=0.16\cdot Re^{-\frac{1}{8}}$; u_{ref} is the reference velocity; L is the reference length scale which equals to the structure characteristic length; V_T is the turbulent kinetic eddy viscosity; $C_\mu=0.09$ is a model coefficient of the $k-\omega$ turbulence model; l is the turbulence length scale $l=0.4\cdot\delta$; δ is the first adjacent layer thickness can be calculated as $\delta=\frac{L}{\sqrt{Re}}$.

3.1.3 Wave modelling

Wave modelling is of prime importance in ship hydroelasticity analysis, an open-source toolbox "waves2Foam" (Jacobsen et al. 2012) is applied in this study to generate and absorb free surface waves in the numerical wave tank (NWT). The relaxation zone technique is adopted to provide better wave quality near the inlet boundary and remove spurious reflection at the outlet boundary. The following equations specify the primary function of the relaxation zones:

$$a_R(\chi_R)=1-\frac{\exp(\chi_R^{3.5})-1}{\exp(1)-1} \tag{3.17}$$

$$\phi_R=\omega_R\phi_R^{computed}+(1-\omega_R)\,\phi_R^{target} \tag{3.18}$$

where ϕ_R refers to either the velocity or volume fraction of water a. The weighting function a_R is always equals to 1 at the interface between the non-relaxed computational domain and the relaxation zones, χ_R is a value between 0 and 1. The relations between χ_R and a_R are shown in Fig. 3.2.

At least three surface elevation gauges are placed inside the wave domain, as shown in Fig. 3.2. WP1 and WP3 are placed inside the regions of wave propagation and damping to monitor the wave quality and wave absorption. WP2 is located in the front of the ship bow to monitor the intake water motions.

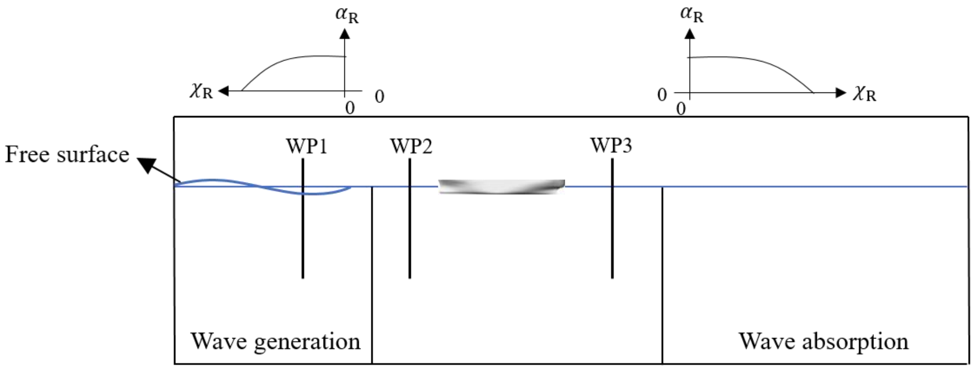

Figure 3.2: Diagram of the variation of χ_R and a_R in relaxation zones and probes positions.

3.1.3.1 Regular wave modelling

The waves2Foam toolbox generic supports various regular wave equations, i.e., Stokes waves, cnoidal wave, stream waves etc. The validity of free surface wave model either depends on the wave depth or wave steepness and the selection of wave theory regarding to the Méhauté (1976). The regular wave is generated in deep water condition with wave steepness less than 0.05 throughout this work, therefore, the Stokes's second-order wave theory is selected, with the resulting expression of free surface and velocity components are:

$$\eta = \frac{H}{2}\cos(\theta) + k\frac{H^2}{4}\frac{3-\sigma^2}{4\sigma^3}\cos\,(2\theta) \tag{3.19}$$

$$u = \frac{H}{2}\omega\frac{\cosh\,(kz)}{\sinh\,(kz)}\cos(\theta) + \frac{3}{4}\frac{H^2\omega k cosh(2kz)}{4sinh^4(kh)}\cos(2\theta) \tag{3.20}$$

$$w = \frac{H}{2}\omega\frac{\sinh\,(kz)}{\sinh\,(kz)}\sin(\theta) + \frac{3}{4}\frac{H^2\omega k sinh(2kz)}{4sinh^4(kh)}\sin(2\theta) \tag{3.21}$$

where, H is the wave height, wave angle $\theta = kx - \omega t + \psi$ with k is the wave number, ω is the angular frequency and ψ is the wave phase and $\sigma = \tanh(\mathrm{kh})$.

3.1.3.2 Focused wave modelling

The focused wave group implemented in this study is based on the NewWave theory (Ning et al. 2009), which generates the extreme wave event from a specified sea spectrum by superimposing several relatively small amplitude waves at a chosen point and time. The spectral shapes of irregular waves were implemented by the JONSWAP spectrum (Hasselmann et al. 1973). The significant wave heights H_s, peak angular frequency is ω_p and peak lifting factor γ are the main parameters to the JONSWAP spectrum.

$$S_j(\omega) = \frac{5}{16} H_s^2 \omega_p^5 \omega_j^{-5} \left(-\frac{5}{4}\right) \exp\,(\left(\frac{\omega_j}{w_p}\right)^{-4})\gamma^{\beta} \tag{3.22}$$

$$\beta = exp\,[\frac{-(\omega-\omega_p)^2}{2\sigma^2}{\omega_p}^2] \tag{3.23}$$

where, β is the coefficient related to the peak lifting factor γ, σ is the shape factor with a value of 0.09.

For the linear NewWave theory, the amplitude of each wave component a_i of frequency f_i is defined as

$$a_i = A_0 \frac{S(f_i)\Delta f}{\sum_i^N S(f_i)\Delta f} \tag{3.24}$$

where $S(f_i)$ is the surface spectral density, Δf is the frequency step (which depends on the number of wave components N and bandwidth), and A_0 is the target theoretical linear wave amplitude of the focused wave (Ning et al. 2009). The extreme wave represented by linear NewWave theory is simply the scaled auto-correlation function corresponding to a specified spectrum.

The linear free surface elevation $\eta^{(1)}$ and horizontal and vertical velocities $u^{(1)}$ and $\omega^{(1)}$ are given by:

$$\eta^{(1)} = \sum_{i=1}^{N} a_i \cos\,[k_i(x-x_0) - \omega_i(t-t_0) + \varphi] \tag{3.25}$$

$$u^{(1)} = \sum_{i=1}^{N} \frac{a_i g k_i}{\omega_i} \frac{cosh k_i(z+h)}{\cosh\,(k_i h)} \cos[k_i(x-x_0) - \omega_i(t-t_0) + \varphi] \tag{3.26}$$

$$\omega^{(1)} = \sum_{i=1}^{N} \frac{a_i g k_i}{\omega_i} \frac{sinh k_i(z+h)}{\cosh\,(k_i h)} \sin[k_i(x-x_0) - \omega_i(t-t_0) + \varphi] \tag{3.27}$$

where, z is the free surface amplitude measured from the Mean Water Level (MWL), x_0, t_0 are the predefined focal location and focal time respectively, a_i is the amplitude of wave components, g is the gravity acceleration, h is the water depth, φ is the phase angle $k_i = \frac{{\omega_i}^2}{g}\tanh\,(k_i h)$ is the wave number and $\omega_i = 2\pi f_i$ is the frequency.

Modulation of phase angle among individual wave components (Eq. 3.25- Eq. 3.27) can superpose the wave peak at a fixed time and position with the mathematical represent as:

$$\varphi = k_i(x-x_0) - \omega_i(t-t_0) + 2m\pi, m = 0, \pm1, \pm2, \cdots \tag{3.28}$$

A uniform current is often applied at the boundary inlet to simulate the ship forward speed in CFD modelling. However, the current effects have influences on the focused wave modelling, including wave steepness, focusing time and position, owning to the nonlinear interaction between the wave and current (Zhang et al. 2014). In the present study, the nonlinear interaction between the wave and current were not considered, therefore, a linear focus wave with the current model proposed by (Li et al. 2012) was implemented as given in Eq. 3.29.

$$(\omega_i - k_i V)^2 = k_i g tan(k_i h) \tag{3.29}$$

where, V is the uniform current speed. Based on this wave-current dispersion relation, the circular wave frequency ω_i and wave number k_i can be calculated by using a mathematical iterative method, the positive root of Eq. 3.29 will find the value of k_i. The rest of wave parameters i.e., wavelength and frequency are updated accordingly. The current at boundary inlet provides a horizontal flow velocity and modifies the focused wave velocity from Eq. 3.26 to Eq. 3.30. To achieve the peak of wave trains energy at a target time and position, the focal location and time are required to be modulated accordingly.

$$u^{(1)} = \sum_{i=1}^{N} \frac{a_i g k_i}{\omega_i} \frac{coshk_i(z+h)}{\cosh(k_i h)} \cos[k_i(x - x_0) - \omega_i(t - t_0) + \varphi] + V \tag{3.30}$$

3.1.4 Finite Volume Mesh Generation and Boundary Conditions

The finite volume mesh was generated using the OpenFOAM default mesh generation tool “SnappyHexMesh” based on cell splitting and mesh fitting techniques (Jasak et al. 2007). A uniform background mesh was initially generated and used to project and snap cells onto the geometry, and then the mesh refinements can flexibly be specified on edges, surfaces and volumes to obtain optimum geometry feature resolutions. The numerical domain used in this study simulates ship motions in deep-water condition, which extends in the three dimensions, i.e., $-1.5\,L < x < 2\,L$, $-0.6\,L < y < 0.6\,L$ and $-1.5\,L < z < 0.5\,L$, where L refers to the ship length between perpendiculars. The grid density at the free surface is progressively refined until it fulfilled the guidelines from (ITTC 2017), in which a minimum of 100 cells per wavelength and 12 cells per wave height were used on the free surface modelling in this study as shown in Figure 3.3(a). To ensure that the high Reynolds number flow features are approximately captured, the grids density at the area around the ship hull are further refined several times with boundary layers, primarily maintains the adjacent wall layer-thickness coordinate $y+$ close to 30. It is worth noting that the proper wall functions are implemented for the hull patch surfaces to model the approximate wall behaviour when the adjacent layer thickness stays in a log-law region. The numerical domain with a wave height of 0.12m and encounter wave frequency of 5.581 Hz is chosen as a representative case, which is displayed in Fig. 3.3 with a general view of the computational mesh and mesh refinement zones.

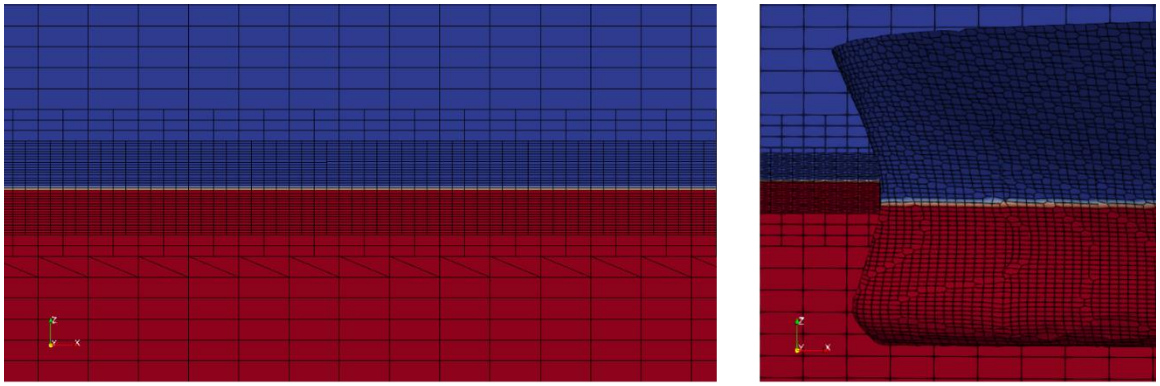
(a) (b)

Figure 3.3: Mesh refinement: (a) Near the free surface, (b) Details at the ship bow.

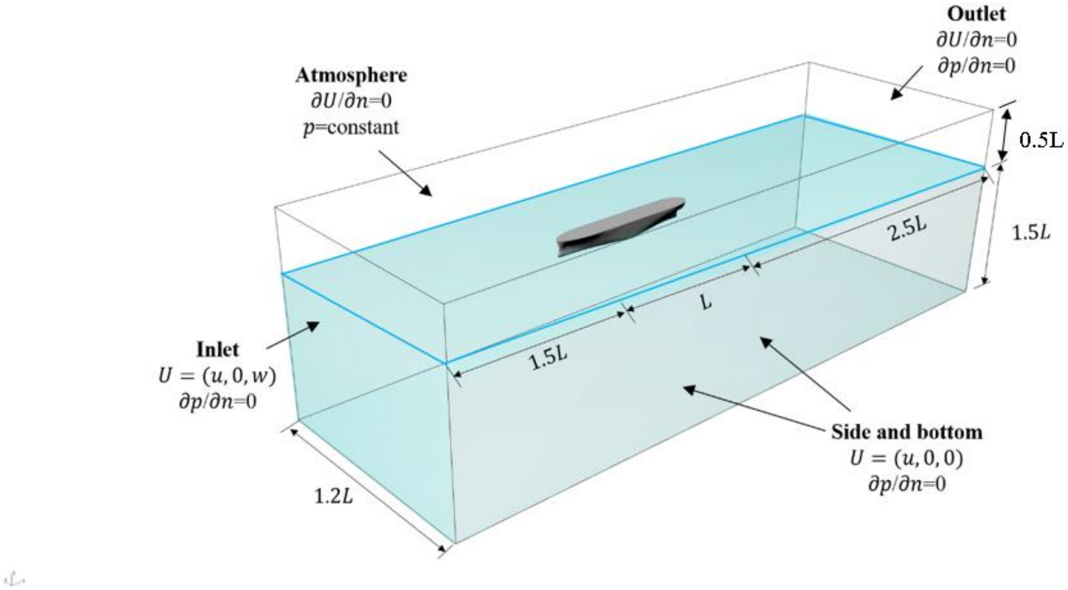

Figure 3.4: The numerical domain with the applied boundaries for the deep-water case.

The boundary conditions for a wave tank are shown as a representative case in Fig. 3.4 as follows: At the left boundary inlet, the velocity inlet is prescribed as the incident wave and current, while the pressure is set as zero gradient. At the right boundary outlet, the current velocity outlet is applied to preserve the conservative of flux inside the computational domain. The boundary condition of the domain top part is set as atmosphere. The lateral sides are set as symmetry planes to avoid wave reflection at the boundaries. The bottom boundary is set as a symmetry plane for deep-water modelling. The moving wall boundary condition with zero pressure gradient is defined on the surface of the ship hull.

3.2 Structural Response Calculation

3.2.1 Rigid body motion

The rigid body dynamic problem is solved using the rigidBodyDynamic library generic in OpenFOAM, where the code is appropriate of solving single rigid body motions. The numerical code is built from the articulated algorithm (Featherstone 2014) using a propagation method of solving forward dynamics problems. The algorithm has a complexity of the order of (n), which is the least possible order of complexity.

The equation of motion of a rigid body system can be written as

$$H(q)\ddot{q} + C(q, \dot{q}) = \tau \tag{3.31}$$

where $q, \dot{q}, \ddot{q}$ denote as the position, velocity and acceleration of the joints, H is the inertia matrix, C is the force which produces zero acceleration, which accounts for forces like gravity, Coriolis and centrifugal forces, τ is the total force acting on the bodies. In this equation, multi-values can be calculated based on what has been provided. Therefore, the forward dynamics method is applied to calculate the acceleration based on the initial position, velocities and forces with the equations shown below:

$$\ddot{q} = FD(model, q, \dot{q}, \ddot{q}) \tag{3.32}$$

This calculated acceleration will be integrated for the first time step to get the new position and velocity, which will be used as an input for the next time step. The forces at bodies are updated simultaneously. Boundary conditions can be applied to a rigid body by applying restrains (forces acting on the body) and constrained (the degree of freedom is restricted).

For multi rigid bodies dynamics, the propagation method was applied to solve the above forward dynamics equations by sequentially calculating the coefficients of each rigid body on the chain; the algorithm detail refers to chapter 7 in their book (Featherstone 2014).

3.2.2 Finite element analysis (FEA)

The finite element method (FEM) is a general numerical method for solving partial differential equations. To solve a problem, the FEM subdivides the system into discrete elements, which are implemented by the construction of a mesh of object. The FEM formulates a boundary value problem, finally results in solving a system of algebraic equations. The governing equation of the structure solver is the weak form of the balance of momentum and is written in the differential form:

$$\rho_s \frac{D^2 U_s}{D^2 t^2} = \nabla \cdot P_s + \rho_s f_s \tag{3.33}$$

where U_s denotes the displacement vector of the structure and its second derivatives represents the acceleration, surface forces are modelled by the second Piola-Kirchoff stress tensor P_s, while the body force per unit mass, such as gravity, is represented by f_s.

A constitutive equation describing the relation between the stress and strain is used to close Eq. 3.33. Specially, for a Saint Venant-Kirchhoff material, the second Piola-Kirchoff stress tensor P_s is obtained by

$$P_s = C{:}E, E = 1/2(F^T F - \delta) \tag{3.34}$$

where C denotes as the elasticity tensor, E is the Green-Lagrange strain tensor, F represents the deformation gradient, and δ is the unit tensor. The governing equation 3.33 is further discretized using the finite element method. With the application of the virtual work method, a linear algebraic equation system by discretisation in the complete solid domain is obtained:

$$[K]\{U_s\} + [M]\frac{D^2}{Dt^2}\{U_s\} = \{F\} \tag{3.35}$$

where $[K]$ denotes the global stiffness matrix, $[M]$ is the global matrix, and $\{F\}$ represents the global force vector.

3.2.3 Multibody Dynamics

To model the nonlinear hydroelastic behaviour of the ship in question, the discrete module beam (DMB) method was applied by adopting a multibody approach in the structure solver MBDyn (Masarati et al. 2014). The term multibody system is related to a large number of engineering fields of research, especially in robotics and vehicle dynamics. Each single body or element of a multibody system is determined their positions and resulting forces by applying the Newton (free particle) and Euler (rigid body) equations, respectively. Later, a series of formalisms were derived, and specifically in MBDyn, which adopts a Lagrange multiplier or redundant coordinate set formations for a multibody system. Compared to the reduced coordinate set method, where only minimum numbers of degrees of freedom (DoFs) are used to describe the motion of the system, a redundant formulation which allows 6 DoFs motion for each body and constraints are enforced by Lagrange multiplier (Masarati et al. 2014). In results, the dynamic behaviour of a multi-body system is derived its motion from the equilibrium of applied forces and the rate of change of momentum.

The demonstration of the DMB method in MBDyn is similar to the standard hydroelasticity experiment's set-up of (Bakti et al. 2021). To make an example of the ship hull was divided into *m* sections, connected by *m-1* beam elements, consisting of a multi-body structure system. For each body of the system, the Newton-Euler equations of motion were established in the differential-algebraic form as a set of first-order equations together with the constraint equations, resulting in a system of Differential-Algebraic Equations (DAE) as follows.

$$M\dot{x} = P \tag{3.36}$$

$$\dot{p} + \phi_x^T \lambda = f(x, \dot{x}, t) \tag{3.37}$$

$$\phi(x, t) = 0 \tag{3.38}$$

where, *M* denotes the inertia matrix of the rigid body, *x* denotes the translational and rotational parameters in the global reference frame. *P* refers to the momentum of the body. λ is the vector of the Lagrange multipliers for the constraints; f is the external force and moment vector exerted upon the body which might be related to its displacement and velocity as well as time. φ is a set of kinematic constraints applied on the body and ϕ_x^T is the Jacobian of φ with respect to the generalized coordinate.

The distance between the centre of gravity of two adjacent sections is taken as a spatial beam for considerating the effects of structural deformation, as shown in Fig. 3.5. The beam element used in the present study is a three-node beam element which is implemented in the MBDyn software by a finite volume approach for the multibody formulation of three-node beam elements based on the Geometrically Exact Beam Theory (GEBT) (Ghiringhelli et al. 2000). The internal forces and moments are evaluated at the cross-section at the evaluation points and related to the geometrical strains and curvatures via the constitutive law with the following equations (Ghiringhelli et al. 2000).

$$\begin{Bmatrix} F_x \\ F_y \\ F_z \\ M_x \\ M_y \\ M_z \end{Bmatrix} = f\left\{ \begin{Bmatrix} \varepsilon_x \\ \gamma_y \\ \gamma_z \\ \kappa_{xy} \\ \kappa_{yz} \\ \kappa_{xz} \end{Bmatrix}, \begin{Bmatrix} \dot{\varepsilon}_x \\ \dot{\gamma}_y \\ \dot{\gamma}_z \\ \dot{\kappa}_{xy} \\ \dot{\kappa}_{yz} \\ \dot{\kappa}_{xz} \end{Bmatrix} \right\} \tag{3.39}$$

where F_x is the axial force component, F_y and F_z are the shear force component, M_x is the torsional moment component, M_y and M_z denote as bending moment components; ε_x, γ_y and γ_z are axial strain and shear strain coefficients, κ_{xy}, κ_{yz} and κ_{xz} are the bending curvature parameters, f denotes as an arbitrary function of beam material constitutive law.

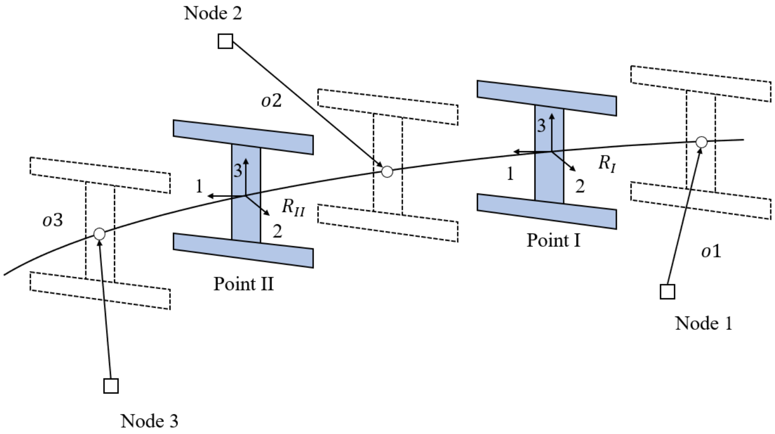

Figure 3.5: An example of a three-node beam element geometry (Ghiringhelli et al. 2000).

The performance of the above beam model has been validated by Bauchau et al. (2016), Liu et al. (2017) and Liu et al. (2019). According to Bauchau et al. (2016), this beam model is valid when the structure's plane section remains plane (no shear deformation) and deformed beam angles are small. The effects of cross-section warping are assumed to be small and neglected.

3.3 Coupling Framework

The purpose of this chapter is first to explain two elaborate FSI coupling frameworks used in this study: 1) A two-way strong coupling between CFD solver OpenFOAM and FEA solver CalculiX, and 2) A two-way loose coupling between OpenFOAM and multi-dynamics solver MBDyn. Then, a closer look at the differences between the two frameworks regarding three key factors: the coupling methods, data mapping scheme and dynamic mesh technique. Finally, a general discussion has been made on which condition a two-way strong or loose coupling gives plausible results.

3.3.1 FSI1: OpenFOAM coupled with CalculiX

The FSI1 coupling framework was established via an open-source coupling library preCICE, which built connections between the OpenFOAM solver and CalculiX by implementing a two-way strong coupling algorithm.

3.3.1.1 Coupling method

The two-way strong coupling algorithm, as indicated by Benra et al. (2011), has a second-order convergence rate, makes it appropriate for the FSI problems with strong dependences between each field involved. Such a two-way strong coupling algorithm has been offered the possibility in open-source coupling library preCICE (Bungartz et al. 2016) with the name of the implicit iterative method. The workflow for a two-way strong coupling algorithm in OpenFOAM is shown in Fig. 3.6.

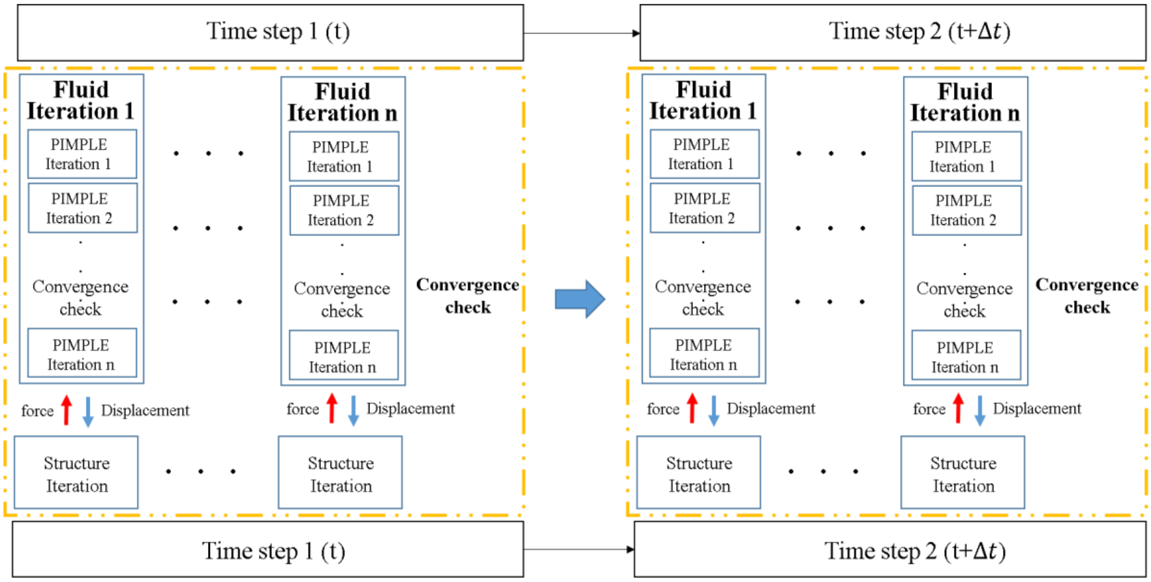

Figure 3.6: The workflow of a two-way strong coupling algorithm in OpenFOAM.

The figure shows that the two-way strong algorithm consists of two types of iteration loops, the outer iteration loop and the PIMPLE iteration loop which inside each outer iteration loop. The outer iteration loop is controlled by the coupling library PreCICE. Users can specify a convergence measurement function; for example, PreCICE supports three types of convergence measurement functions, e.g., the absolute, the relative and minimum iteration number functions. The most commonly used function is the relative convergence measures function. Based on this function, the convergence is considered if the relative coupling residuals of the communication data (displacement and forces) during the last iteration is below a value. Inside each outer loop iteration, the subcycling is iterated multiple times to fulfil the PIMPLE algorithm's convergence in order to stabilise the simulation and preserve equilibrium conditions on the interface. It is worth noting that the PIMPLE Algorithm combines PISO (Pressure Implicit with Splitting of Operator) and SIMPLE (Semi-Implicit Method for Pressure-Linked Equations).

An acceleration scheme is essential for implicit coupling, which implements an under-relaxation factor in every iteration based on the current residuals of the defined primary data. The processed data gives advantages in fastening the convergence speed and stabilising the fixed-point iteration. In PreCICE, three types of acceleration can be configured: constant (constant under-relaxation), Aitken (adaptive under-relaxation), and various quasi-Newton variants. The detailed description of these acceleration schemes refers to the thesis by Gatzhammer (2014) and the mathematical description refers to Mehl et al. (2016).

The main configuration of coupling OpenFOAM and CalculiX via PreCICE is shown in Fig. 3.7. A parallel implicit algorithm, as recommended above, was applied between the fluid and structure solvers using a peer-to-peer approach, as shown in Fig. 3.7. Two official adapters, OpenFOAM adapter (Chourdakis 2017) and CalculiX adapter (Uekermann et al. 2017) are plugged in for data communications. An improved IQN-ILS method (Degroote et al. 2009) is employed to stabilize and accelerate the convergences.

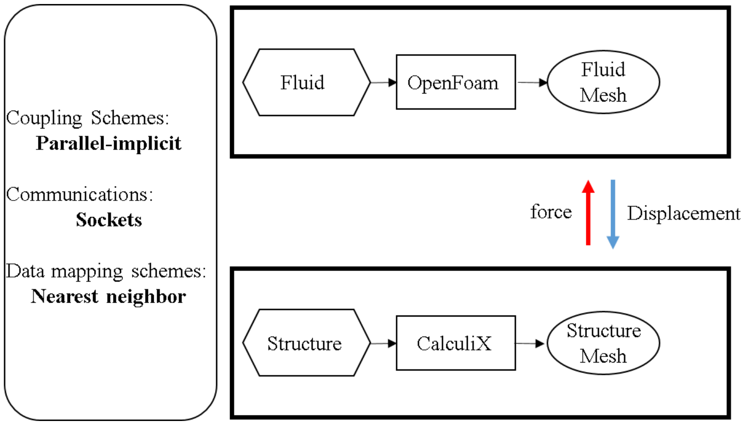

Figure 3.7: Configuration of the fluid structure interaction procedure via PreCICE.

Another critical factor in coupling a transient FSI simulation is correctly mapping the data at the coupling interface through a pair of non-matching grids of fluid and structure meshes. The fluid-structure interface exists at the boundary between fluids and structures, mostly called wet surfaces, which shares the information of the solution between two mediums. For ship hydroelasticity, the fluid and structural solver are coupled with displacements and velocities at the wet surfaces. The fluid solver delivers forces exerted on the structure as an output. Then, the structure solver takes these forces as an input and computes displacements and velocities as an output.

The data communication is controlled by mapping schemes in PreCICE and aims to satisfy the geometrical compatibility and the equilibrium conditions on the wet surfaces. The coupling library PreCICE supports various types of mapping schemes for users, ranging from first-order nearest neighbour mapping to high order Radial-basis function mapping. In this study, two schemes for data mapping, in which the consistent mapping scheme is applied for the transformation of displacements. In contrast, a conservative mapping scheme is applied for forces for energy balance. This way, boundary conditions are fulfilled by both the kinematic (equality of forces) and the dynamic (equality of velocities and displacements).

The nearest neighbour mapping scheme is used in the ship hydroelasticity study, which owns a first-order accuracy. The advantage of this scheme is that it is efficient for complex simulations, which fasten the data coupling speeds when a large number of discrete grids are located on wet surfaces. It owns relatively simple model setups and no requirements to specify geometry feature edges, which is appropriate for prime design for large simulations. However, the accuracy of the present scheme is questionable, therefore, finer meshing is required on the wet surface, and an uncertainty test is recommended. One representative case of the wet surfaces generated through the fluid and structure solver is shown in Fig. 3.8.

The fluid mesh density is intended to design finer than the structure mesh to calculate the fluid forces more precisely and eliminate the numerical instability at the initial conditions.

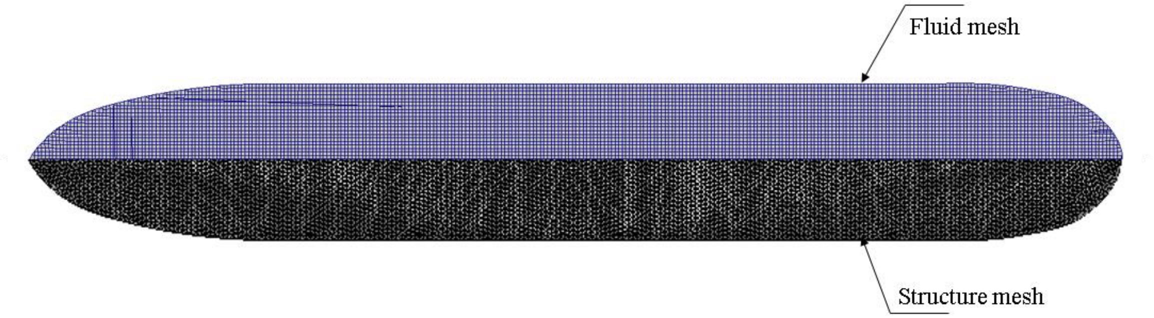

Figure 3.8 Example of non-matching wet-surface meshes through fluid and structure sides, CFD mesh (Shown in blue) and FEA mesh (Shown in black).

3.3.1.2 Dynamic mesh technique

To update the fluid mesh motion according to the solution from the structure solver, the dynamic mesh handling technique of mesh motion is applied based on the finite volume-based Laplacian mesh motion for the displacement field. This dynamic mesh operation solely involves the displacements of the mesh points without altering the topological information of the mesh (Jasak

2009). The distortion of internal parts of the solution domain relies on the solution of a diffusion (Laplace) transport equation for the displacement point fields using the equation shown below.

$$\nabla.(\gamma\nabla d) = 0 \tag{3.40}$$

where γ is the displacement diffusion coefficient, and d is the point displacement field. The diffusion rate of displacement from the boundaries to the internal mesh regions is defined with the spatially varying diffusion coefficient *y* given as a function of the distance between the point and the mesh boundary $\gamma = \gamma(r)$. In order to calculate the displacements at the mesh points (cell corners), interpolations from the cell-centred values to mesh points are required. The mesh motion boundary conditions are applied to the moving bodies, using data computed based upon the calculations from the structure solver.

3.3.2 FSI2: OpenFOAM coupled with MBDyn

The FSI2 coupling framework is established between OpenFOAM and multi-body dynamic solver MBDyn based on a two-way loose coupling algorithm in an iteratively staggered coupling regime. Two solvers are communicated through sockets; the OpenFOAM solver worked as the main solver, and MBDyn reacted as the slave solver.

3.3.2.1 Coupling method

The two-way loose coupling method has a relatively simplified workflow, as shown in Figure 3.9. Compared to the two-way strong coupling workflow in Fig. 3.8, there exists no outer iterations inside each time step in a two-way loose coupling approach. The communication data are transferred directly within each sub-cycling until the PIMPLE algorithm converged. To stabilize the whole simulation and preserve equilibrium conditions on the interface, a minimum of five PIMPLE iterations are recommended inside each time step. Based on the above design, the communications between the fluid and structure solver can be performed efficiently, which significantly reduces on the overall computational cost.

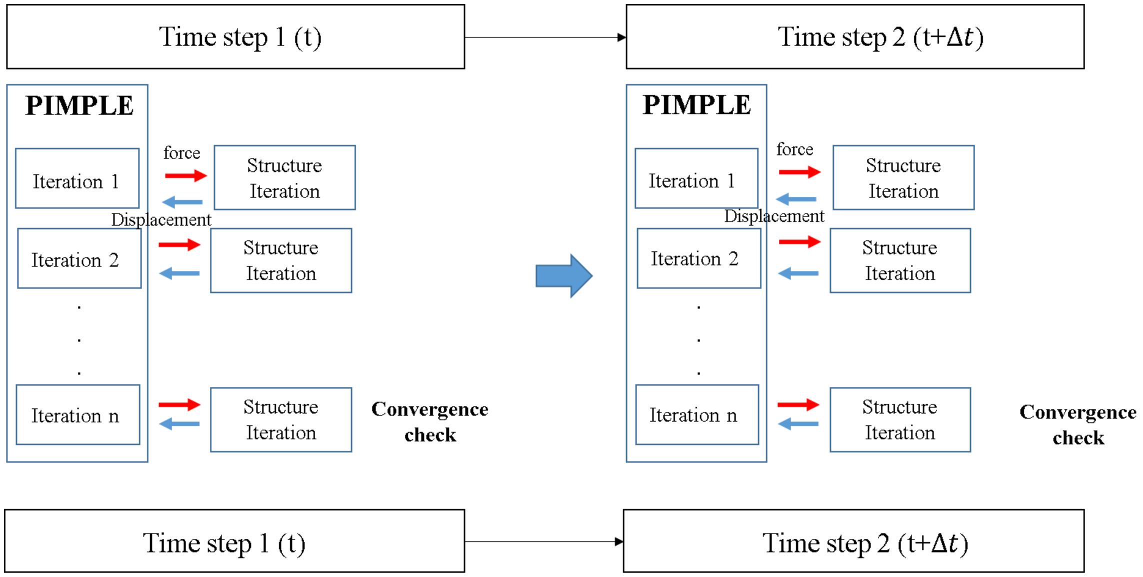

Figure 3.9: Two-way strongly coupling algorithm and two-way weak coupling algorithm.

A detailed workflow of the present CFD-DMB approach is shown in Fig. 3.10. At the start of a CFD-DMB simulation, MBDyn creates a TCP/IP socket and acts as a server waiting the client OpenFOAM connects to the socket. Inside the data communication scheme, the scalar quantities of pressure and wall shear stress integrated though fluid wet surface are calculated from the OpenFOAM and mapped onto the structure nodes in MBDyn. By accepting the force data, the MBDyn solves the differential equations (Eq. 3.36 - Eq. 3.38) and predicts the structural responses. The update nodal displacement then feeds back to the CFD solver so as to establish a two-way communication.

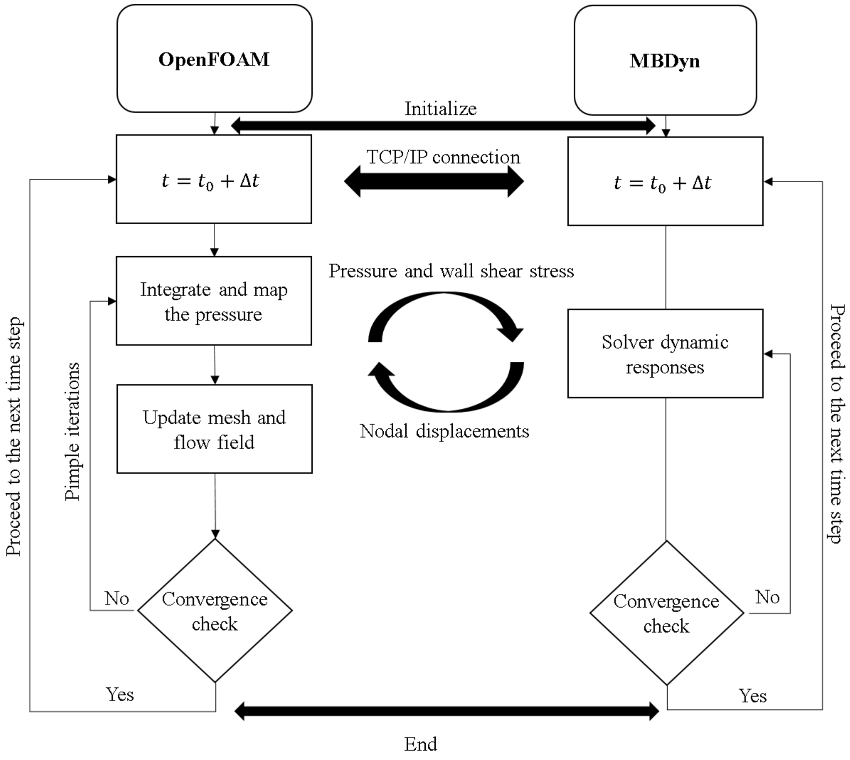

Figure 3.10: The workflow of two-way CFD-DMB coupling framework.

3.3.2.2 Dynamic mesh technique

The fluid mesh has to be updated simultaneously based on the dynamic mesh technique of mesh motion, which relies on the solution of Laplace transport equations for the displacement point fields. However, the dynamic mesh technique handling in the CFD-DMB approach requires the mesh motion to have solid body motion and cell deformation functions.

The solid body motion involves displacement of mesh points, which is performed so that the points retain their relative positions. On the other hand, mesh deformation is introduced at boundary meshes, which induces relative motions between mesh points, distorts mesh cells and modifies the mesh in an inhomogeneous way. The inverse mesh deformation is applied to define the motions at mesh boundaries in which the large motions are present. The fields solve cell-centred mesh motions with the boundary fields stored at face centres. In order to calculate the displacement at cell corner points, interpolation from cell-centred values to the mesh points must be performed.

3.3.3 Concluding Remarks

In this chapter, two transient CFD-based FSI frameworks are established for ship hydroelasticity analysis: the CFD-FEA and the CFD-DMB methods. The various numerical methods and techniques adopted in the frameworks are discussed in detail. The high-fidelity CFD toolbox OpenFOAM is applied to model fluid flow and the free surface is modelled via the VOF method. An open-source wave generation tool is incorporated for wave generation and absorption in a numerical domain. For the structural modelling, two structure software (Calculix and MBDyn) are employed for calculating the structural responses of flexible components. In order to couple the fluid and structure solver, a two-way strong and a two-way loose algorithm are applied for the CFD-FEA and CFD-DMB framework, respectively. A series of coupling procedures, including coupling schemes, data communications and mesh motions are descripted about both methods. The strengths and weakness of two frameworks are summarized in Table 3.2.

Table 3.2: A general evaluation of the present CFD-FEA and CFD-DMB method.

Numerical methods	**Advantages**	**Disadvantages**
CFD-FEA	➢ Appropriate for strong FSI problems. ➢ High numerical accuracy.	➢ Large computational demands. ➢ Critical mesh distortion in the presence of large structural deformation.
CFD-DMB	➢ Significantly reduces the overall computational efforts.	➢ Time stepping and field interpolation procedures that are not always energy preserving, leading to divergence or artificial damping in the solution. ➢ No post-processing tool.

4 Validation Studies

Validation assessment is of prime importance for numerical simulations to determine if the computational model agrees with physical reality. First, the beam performance was evaluated by analysing a simple cantilever beam's deformation between two structural solvers (i.e., Calculix and MBDyn) and the analytical results. Later, the CFD model in OpenFOAM was accessed by investigating the seakeeping behaviour of a CTV vessel in head seas. Finally, the coupled CFD-DMB method was validated using a flexible segmented barge in waves. The numerical results were compared with that from another co-simulation, theories and experiments.

4.1 Beam Behaviour Validation

The first validation case was to examine the accuracy of beam modelling between the FEA and DMB methods using the open-source toolbox Calculix V2.13 and MBDyn V7.3. The numerical results were further compared to the commercial FEA software Abaqus V2020 and the theoretical values. A simple cantilever beam was selected as a representative case with one end fixed and a constant load acted at the other tip, as shown in Fig 4.1. The gravity is not considered.

Two assumptions have to be made:

- Normal of neutral surface remains normal after deformation.
- Deformation is relatively small.

Based on the above assumptions, the Euler-Bernoulli beam theory was adopted for beam modelling. The material characteristics of the elastic beam was summarized in Table 4.1.

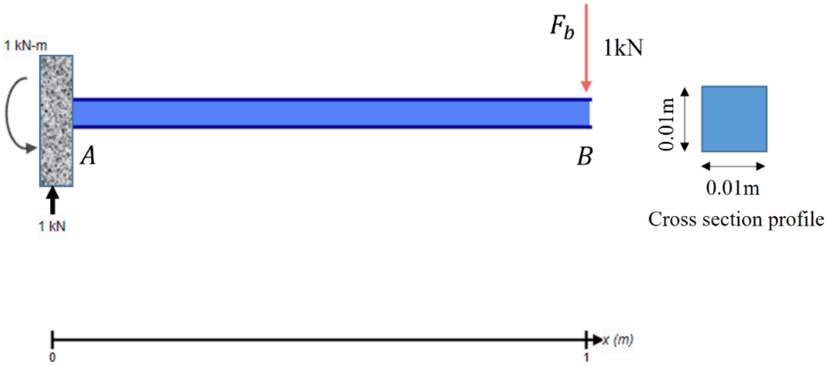

Figure 4.1: A fixed-end cantilever beam with cross section profile.

1. The theoretical equations for a pure vertical bending beam can be summarized as follows:

$$\delta_B = \frac{F_b L^3}{3EI} \tag{4.1}$$

$$M = -F_b \cdot L \tag{4.2}$$

$$\sigma = \frac{My}{I} \tag{4.3}$$

where δ_B is the deflection of beam point B, E is the modulus of elasticity, I is the moment of inertia, L is the length of beam, M denotes the bending moments, y is the distances to point from neutral axis.

Table 4.1: Physical properties of the cantilever beam.

Properties	Unit	Value
Beam length L	m	1
Concentrated load F_b	N	10
Cross-section height	m	0.01
Cross-section thickness	m	0.01
Young’s Modulus E	Gp_a	210
Poisson’s Ratio	-	0.3

2. Beam in FEA

Beams modelling in Abaqus were well introduced in their manual (Abaqus 2012); following the software modules from defining the geometry, determining the material properties and boundary conditions, and finally creating a job, users were capable of building the model for analysis. Although the open-source FEA solver Calculix does not support a graphical user interface (GUI) as Abaqus, users could draw the grid through other pre-processing software and write the .inp file based on their tutorials (Dhondt 2017).

3. Beam in MBDyn

The beam modelling procedure in multi-body dynamics software MBDyn can be found in their tutorial (Masarati 2017). One additional pair of total joints was introduced to clamp the left end beam point with a static background node to restrain the left end in space.

For evaluation of the results, the displacement of the trailing edge of the beam was computed over time shown in Fig. 4.2, and the maximum bending moments were estimated for each numerical model. The overall comparison is shown in Table 4.2.

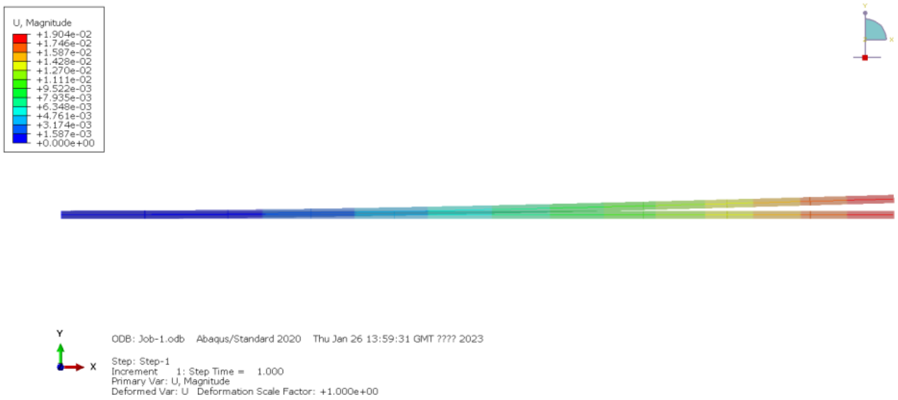

Figure 4.2: Vertical displacement of the cantilever beam (Example postprocessed in Abaqus).

Table 4.2: Comparisons of beam deformation and bending moments among FEA, DMB and theory.

	Displacement	Error (%)	Bending moments
Theoretical solutions	0.01905	-	10.0
Calculix	0.01860	2.36	10.0
Abaqus	0.01904	0.05	10.0
MBDyn	0.01869	1.89	10.0

4.2 Seakeeping Evaluation of a Rigid Crew Transfer Vessel (CTV) in Head Seas

Crew transfer vessels, as applicable to the offshore wind industry, were mainly a type of catamaran with a size between 16 meters to 27 meters, providing maintenance services by transferring technicians from port to offshore wind platforms. The double-hull featured vessels had less hull volume, small displacement and low drag in the water, which benefited the high mobility and fuel economics. During the transfer phase, the seakeeping characteristics need more attention, as Phillips et al. (2015) stated that technicians may be more sensitive to get the motion sickness effects than seamen.

There were several existing guidelines which illustrated the operational limits of a crew transfer sailing at sea conditions with the consideration of the crew comforts, the corresponding criteria were listed:

- The vertical acceleration aCG at LCG was less than 0.15g, and horizontal acceleration was about 0.12g (DNV 2020) (G9 2014).
- The maximum significant wave height was 1.5m, noting that the operational ability was also affected by the wave frequency, wave length and current (VERITAS 2018).

- The maximum pitch and roll RMS values were 4 degrees and 6 degrees, respectively.

Generally, the accurate prediction of the rigid ship motion was the primary importance to study on the transferability and accessibility of CTV operation at seas.

4.2.1 Model Description

The research vessel used in this study was a double-hull catamaran that had a length of 18m, and a light draft of 1.38m, which were common types used for providing services among wind farms. The ship model used in this analysis received from the hydrodynamic lab of the University of Strathclyde with a scale ratio of 1:10. The vessel parameters were verified with several experimental tests before, including the weighting, inclining and swing test (Lin 2019). The vessel's main particulars in model scale were shown in Table 4.3 and its hull form was shown in Fig. 4.3.

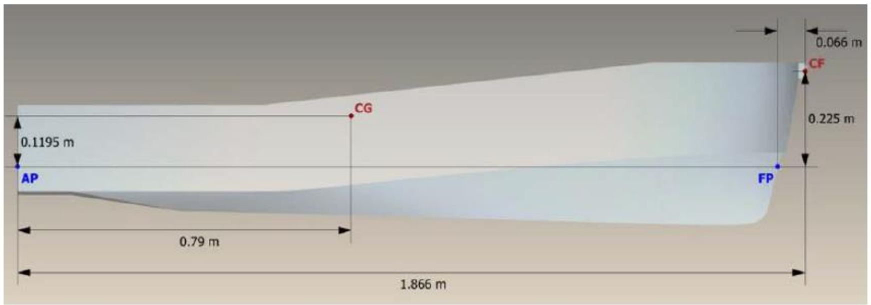

Figure 4.3: Body plane of the catamaran model.

Table 4.3: The principal particulars of a catamaran ship.

Principal particulars	Symbol	Scale
Scale factor	λ(-)	10
Length	$L(m)$	1.850
Breath	$B(m)$	0.690
Design draft	$T(m)$	0.138
Displacement volume	$\nabla(m^3)$	0.044
Vertical center of gravity (from keel)	$KG(m)$	0.253
Moment of inertia	$k_{yy}(\mathrm{kg}m^2)$	9.157
Reynolds number	R_e(-)	4.26×10^7

Turbulence was modelled with the Reynolds-averaged stress (RAS) SST $k - \omega$ model. The inlet turbulence parameters were carefully calculated and assigned at the initial condition with the following equations from Islam et al. (2019).

$$I = 0.16 \cdot Re^{-\frac{1}{8}} \tag{4.4}$$

$$k = \frac{3}{2}(u \cdot I)^2) \tag{4.5}$$

$$\delta = \frac{L}{\sqrt{Re}} \tag{4.6}$$

$$\mathrm{l} = 0.4 \cdot \delta \tag{4.7}$$

$$C_\mu = 0.09 \tag{4.8}$$

$$\omega = \frac{\sqrt{k}}{C_\mu^{1/4} \cdot l} \tag{4.9}$$

$$V_T = \sqrt{\frac{3}{2}} \cdot u \cdot I \cdot l \tag{4.10}$$

Where I was the turbulence intensity; k was the turbulent kinetic energy; δ was the height of the first adjacent layer; l was the turbulence length scale, ω was the turbulence specific dissipation rate, V_T was the turbulent kinetic eddy viscosity. $C_\mu = 0.09$ was a model coefficient of the $k - \epsilon$ and $k - \omega$ turbulence models.

In OpenFOAM, the time derivative term was discretized using the first order backward Euler scheme, which has been widely used in the industry. The second order linear upwind differencing scheme was set for convection terms. The artificial compression term was introduced to the phase fraction convection equation to exert pressure on the interface to keep it from dispersing. The pressure-momentum coupling equations were solved based on the PIMPLE algorithm, which contained five sub-cycling for each time step with extra two pressure-correction inner loops. The cell motion was calculated for the mesh deformation technique. An overall relaxation factor of 0.9 was set for all variables to stabilize the numerical model.

The simulations were run on Archie-West HPC (High-Performance Computation) cluster. The specification of HPC cluster was a 2560 cores (64 Lenovo SD530 nodes) with 192GB of RAM per node (4.8GB per core) using Intel Xeon Gold 6138 (Skylake) processors. All the cases were run parallel on a single node (40 cores), the average time step was set to be 0.002s. All the simulations were run up to 30s for attaining stable results and the required the physical time was about 120h -

140h per case.

4.2.2 Verification and Validation

The verification study was a substantiation procedure that a numerical model represented a conceptual model within specified limits of accuracy (Oberkampf et al. 2002). According to ITTC (ITTC 2011), the numerical errors had three categories into iterative errors, gird size error, time step errors (Stern et al. 2001). The iterative error was mainly caused by the normalized residuals when solving PDE equations with the differential methods, the convergence should be achieved with at least three orders of magnitude decrease of error. The iterative error may be ignored in this case due to the tolerance control setting were applied in the solver. Only the uncertainty of grid and time were presented based on the error estimation approach called Grid Convergence Method (GCI), which was first presented by Celik et al. (2008) based on the Richardson extrapolation (RE) method. It referred to overcome the limitation RE method that the predicted variables may not exhibit a smooth monotonic dependence on grid resolution. Three key factors were studied, the convergence ratio R_k, the order of accuracy p and the Grid Convergence Index (GCI).

The convergence ratio implied the result difference between each two pair of cases, and the value was used to judge for the convergence conditions:

$$R_k = \epsilon_{21}/\epsilon_{32} \tag{4.11}$$

1. Monotonic convergence: $0 < R_k < 1$;
2. Oscillatory convergence: $R_k < 0$;
3. Divergence: $R_k > 1$

Where the ϵ_{21} and ϵ_{32} represented the solution differences of coarse case φ_1 and medium case φ_2, medium case φ_2 and fine case φ_3, the expression showed below.

$$\epsilon_{21} = \varphi_2 - \varphi_1 \tag{4.12}$$

$$\epsilon_{32} = \varphi_3 - \varphi_2 \tag{4.13}$$

The order of accuracy p and Grid Convergence Index (GCI) were predicted using the following equations:

$$p = \frac{1}{\ln(r_{21})}\left|\ln\left|\frac{\epsilon_{k32}}{\epsilon_{k21}}\right| + q(p)\right| \tag{4.14}$$

$$GCI_{fine}^{21} = \frac{1.25e_a^{21}}{r_{21}^{p}-1} \tag{4.15}$$

For performing the uncertainty analysis, three different mesh resolutions and three time steps were used. For the mesh convergence test, the grid numbers were refined at the free surface, the number increased with a rough ratio of $\sqrt{2}$ among coarse, medium and fine cases, from 8 to 16. The total grid numbers were increased correspondingly from 5.41 million (10 cells) to 9.19 million (16 cells). Also, three time steps, 0.002s, 0.004s, 0.008s were studied for the time convergence test, with an increasing ratio of 2. The GCI results were shown in Table 4.4, which were analysed for the trim and sinkage prediction with the ship has no forward speed and the wave period is 2s.

Table 4.4: The GCI uncertainty analysis performed for the catamaran model at wave frequency of 0.5 Hz.

Mesh convergence study	Trim at COG [m]	Sinkage at COG [m]	Time convergence study	Trim at COG [m]	Sinkage at COG [m]
Coarse solution (f1)	0.076	4.581	Coarse solution (f1)	0.0771	4.6475
Medium solution (f2)	0.075	4.591	Medium solution (f2)	0.0668	4.6220
Fine solution (f3)	0.074	4.632	Fine solution (f3)	0.0613	4.271
Number of coarse cells	4,492,152	4,492,152	Minimum time step	0.002	0.002
Number of medium cells	5,906,328	5,906,328	Medium time step	0.004	0.004
Number of fine cells	9,186,726	9,186,726	Maximum time step	0.008	0.008
Refinement ratio r21	0.761	0.760	Refinement ratio r21	2	2
Refinement ratio r32	0.643	0.643	Refinement ratio r32	2	2
Convergence ratio R	0.235	0.249	**Convergence ratio R**	1.872	0.066
Value of s	-1	-1	Value of s	-1	-1
Order of accuracy	1.432	1.326	**Order of accuracy**	0.905	3.902
Value of function	-1.055	-1.028	Value of function	0	0
Relative error	0.525%	0.222%	Relative error	13.359%	0.548
Extrapolated result	0.077	4.558	Extrapolated result	0.088	4.649
Extrapolated error	1.083%	-0.511%	Extrapolated error	13.275%	0.039%
GCI uncertainty	1.368%	0.636%	**GCI uncertainty**	19.134%	0.049%

As can be seen from the above analysis, the results showed three monotonous convergence cases and one divergence case. The divergence condition occur in the time uncertainty test because the maximum time step was selected as too large, therefore, fluid field may not solve correctly. A comprehensive uncertainty test on time-step sizes will be presented in future work.

The validation study presented here was the FFT evaluated results of the ship heave and pitch transfer functions with five wave frequencies. The medium-mesh grid density (12 grids at the free surface) and the smallest time steps (0.002s) were selected through all simulations. The numerical results (black) were compared with the experimental result (red), as shown in Fig. 4.4. The numerical results showed a good agreement with the experiments.

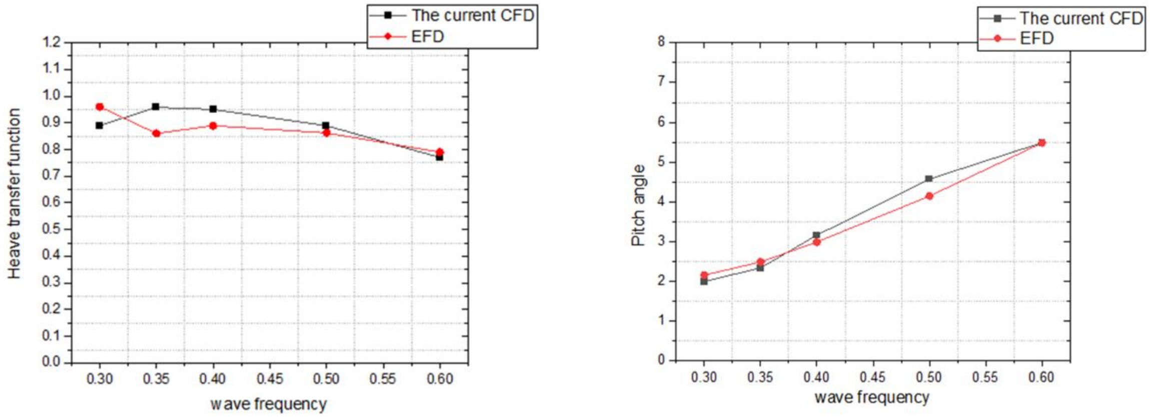

Figure 4.4: The heave and pitch results compared between numerical model and experiments.

To further illustrate the results, the stream velocity distribution at the free surface with four shot cuts was presented in Fig. 4.5 for one wave period. The resulting wave pattern showed a high resolution at the boundary conditions, which proved the current mesh distribution could capture the flow phenomenon at near-wall regions. It could be noted that the high flow velocity was captured at the region between two demi hulls, which may cause by the water trapping phenomenon.

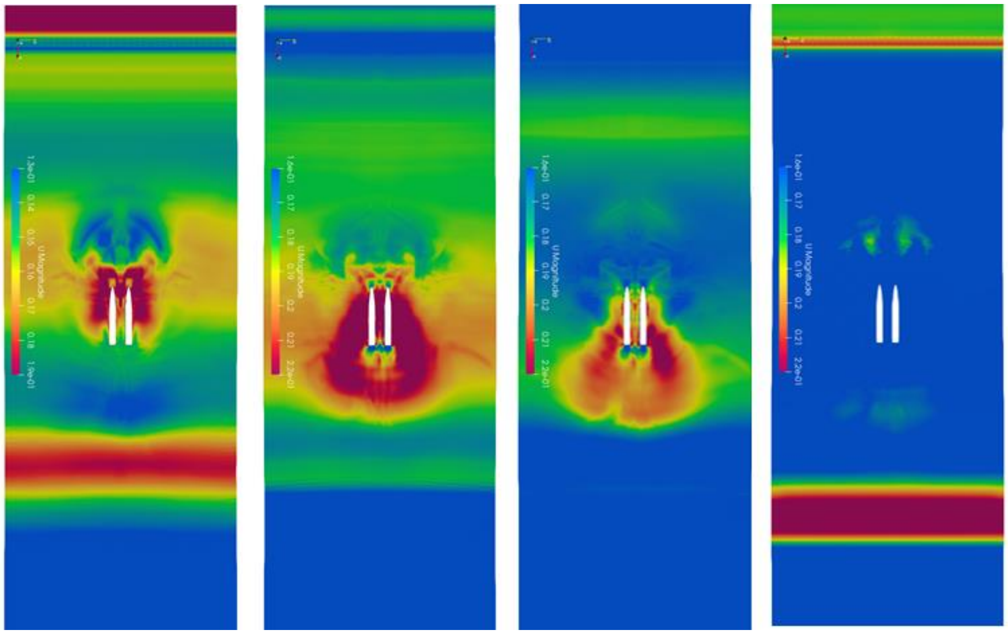

Figure 4.5: Velocity distribution on free surface and hull form for wave period at 2s.

4.2.3 Concluding Remarks

This study evaluated the CFD code in OpenFOAM by predicting a double-hull vessel motion in head waves. Three different mesh resolutions and three time steps were used to perform the numerical uncertainty analysis; then the results were compared with experimental data for validation. One numerical issue is worth noting that the displacement Laplacian mesh technique in OpenFOAM was not fully equipped to perform cases with well-pronounced ship motions, such as, cases with high wave frequencies and large wave amplitudes. Therefore, an alternative mesh handling method, i.e., sliding mesh or overset mesh technique, was recommended as alternatives.

In conclusion, it is found that the dynamic ship motions of the selected CTV were highly dependent on the environmental conditions, i.e., wave frequencies and wave amplitudes. In specific cases, e.g., short-wave conditions ($H_s > 0.5Hz$), the pitch motion was found over 4 degrees, which exceeded the limits from criteria; therefore, the ship may not be safe to operate in such conditions.

4.3 Hydroelastic Analysis of a Floating Barge Based on CFD-MBD Coupling Approach

The validation case for a transient FSI simulation was presented in this chapter on a benchmark flexible barge floating on the free surface. The floating barge was deformable under the wave excitation, which formed a coupled FSI system. This benchmark case has previously been studied by many researchers based on various numerical and experimental methods, i.e., experiments (Remy et al. 2006) and (Senjanović et al. 2009), potential flow coupled with FEA (Senjanović et al. 2008), CFD coupled with FEA (Lakshmynarayanana et al. 2019).

4.3.1 Model description

The numerical model has a similar setting up with the traditional hydroelastic experiments (Senjanović et al. 2008), as shown in Fig 4.6. The floating barge contained 12 connected segments. Each segment had a uniform cuboid shape except for the bow caisson which had a bevelled shape, as shown in Fig. 4.7. The segments were clamped to a steel rod which was placed 57mm above deck level. The rod had a square cross-section of $10\text{mm} * 10\text{mm}$ and its material characteristics were summarized in Table 4.5.

Figure 4.6: Hydroelastic experiments of the floating barge model, pictures from (Lakshmynarayanana et al. 2019) and (Senjanović et al. 2008).

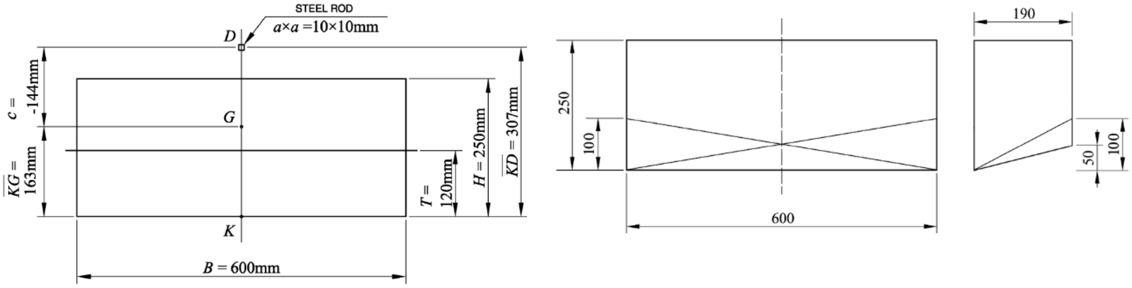

(a) (b)

Figure 4.7: Flexible barge geometry characteristics.

Table 4.5: The floating barge dimensions and rod characterises.

Parameters	Unit	Value
Length (L)	m	2.445
Beam (B)	m	0.6
Depth (D)	m	0.25
Draft (T)	m	0.163
Total mass (m_{total})	kg	172.55
Mass of each caisson	kg	13.7
Mass of bow caisson	kg	10.0
Moment of inertia of rod (k_{yy})	m^4	8.33×10^{-10}
Young's modulus of rod (E)	N/m^2	2.1×10^{11}

Figure 4.8(a) displayed the discretized mesh domain with a total of 3.5 million grids for the CFD solver. The surface mesh at the barge boundary was shown in Fig. 4.8(b); the mesh refinements

were uniformly applied on edges and surfaces to obtain optimum geometry feature resolutions. The grids density at the free surface was progressively refined until it fulfilled the guideline from (ITTC 2017), in which a minimum of 80 cells per wavelength and 12 cells per wave height were used on the free surface modelling in this study, as shown in Fig. 4.8(c). The boundary conditions for the fluid domain were specified, as shown in Fig. 4.8(d). Wave generation and absorption boundaries were adopted from Waves2Foam toolbox at the inlet and outlet boundaries. The symmetry boundary was assumed at the sides and bottom, which indicated a deep and open-water condition in OpenFOAM.

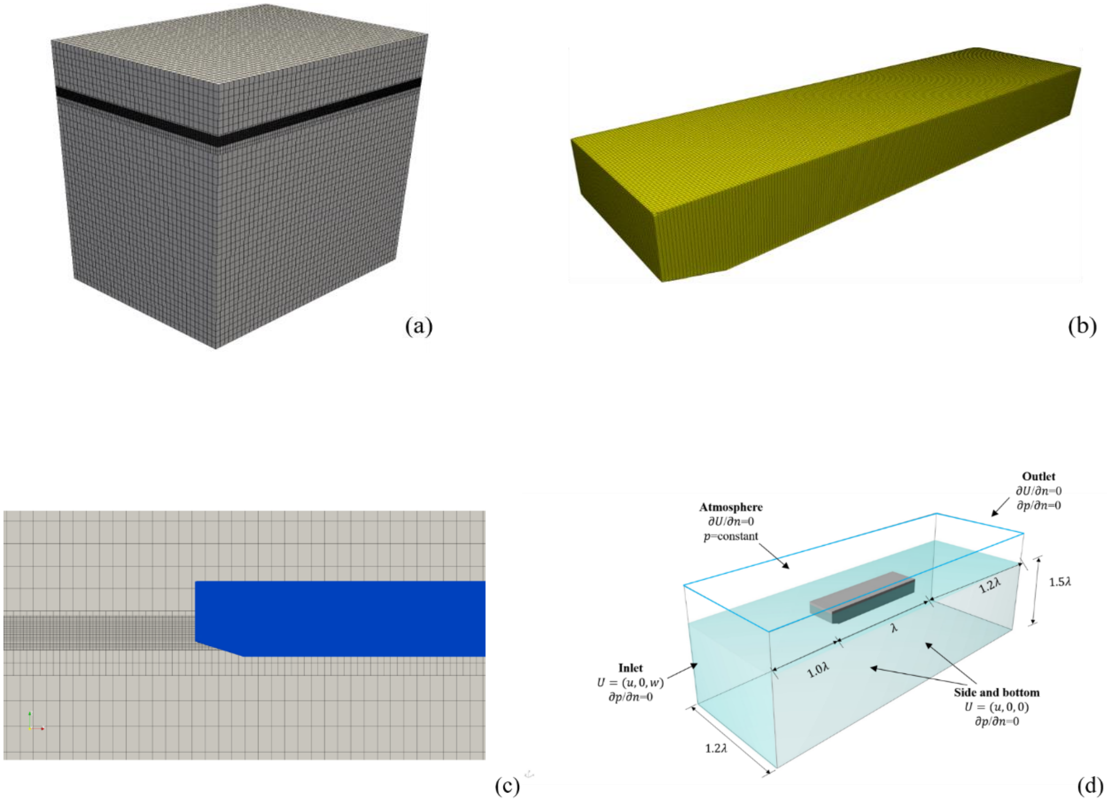

Figure 4.8: The detailed configuration of OpenFOAM set-ups: (a) Numerical domain mesh grid, (b) Surface mesh grid, (C) Mesh refinement, (d) Boundary conditions.

Responses of flexible barge with no forward speed were calculated in heading wave condition with four wave frequencies, as summarized in Table 4.6.

Table 4.6: Wave characteristics.

Wave periods (s)	Wave frequency (rad/s)	Wave length (m)	Wave height (m)	λ/L
0.9	6.981	1.264	0.1	0.52
1.0	6.283	1.561	0.1	0.64

1.2	5.235	2.248	0.1	0.92
1.6	3.926	3.996	0.1	1.63
1.8	3.490	5.058	0.1	2.07

The structural model was designed in multibody dynamics solver MBDyn and only the odd number of the barge segments were displayed in Fig. 4.9. MBDyn read manually the input cards including structural nodes, bodies, joints and beam elements. The structural nodes created the foundation of nodes at global positions, and then bodies and beam elements were generated basing on the structural nodes. The body element saved the input of mass properties and mass moment of inertia, which was used to represent the barge patch information. The steel rod was modelled using three-node beam elements, with a closed square cross section of $0.01\mathrm{m} * 0.01\mathrm{m}$. The detailed numerical demonstration of the structural model and material properties were summarized in Table 4.7 and 4.8.

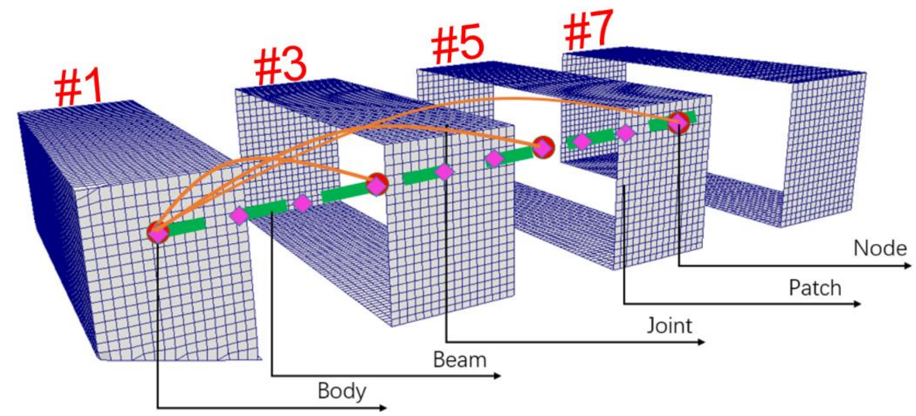

Figure 4.9: The numerical demonstration of DMB model for a floating barge.

Table 4.7: Structural model demonstration.

DMB model	Colour	Symbol	Number
Structural nodes	Pink diamond	N	25
Body elements	Red dot	B	12
Total joint elements	Orange line	TJ	26
Beam elements	Green rectangle	Bm	11

Table 4.8: Material properties for the input of body elements.

Material properties	Symbol	Unit	Value
Elastic Modulus	E	GPa	210
Shear Modulus	G	GPa	77
Flexural rigidity	EI_x	$\mathrm{N \cdot m^2}$	135
	EI_y	$\mathrm{N \cdot m^2}$	175
	EI_z	$\mathrm{N \cdot m^2}$	175
Moment of inertia	I_{xx}	$\mathrm{kg \cdot m^2}$	$I_{xx} = 1/12 \cdot Mass \cdot (w^2 + h^2)$
	I_{yy}	$\mathrm{kg \cdot m^2}$	$I_{yy} = 1/12 \cdot Mass \cdot (ddL^2 + w^2)$
	I_{zz}	$\mathrm{kg \cdot m^2}$	$I_{zz} = 1/12 \cdot Mass \cdot (ddL^2 + h^2)$
Structure damping	d		$1.0e^{-2}$

4.3.2 Hydrodynamic responses of the floating barges in waves

The RAOs of the vertical displacements were calculated at four barge segments (Pt.1, Pt.9, Pt.17 and Pt.23), and the numerical results were illustrated in Fig. 4.10. A series of regular wave conditions, ranging from 6.981 rad/s ($\lambda/L_{barge} = 0.9$) to 3.490 ($\lambda/L_{barge} = 2$) rad/s, were tested. A constant wave amplitude of 0.01m was selected, which was coincident with the experimental settings (Senjanović et al. 2008). It is worth noting that the gaps between the segments in the experimental model were not considered in the CFD-FEA model. The absence of gaps in the numerical model could result in slightly different hydrodynamic properties, i.e., added mass and fluid damping (Lakshmynarayanana et al. 2019). The numerical results were compared with a 2D linear ship hydroelasticity theory Mars, co-simulation (StarCCM+ & Abaqus) (Lakshmynarayanana et al. 2019) and experimental results by (Remy et al. 2006).

From the responses Fig. 4.10, an overall good agreement was found between the CFD-DMB method and the experimental predictions, however; the more significant differences were observed in short-wave conditions, i.e., wave frequencies of 6.28 rad/s and 6.98 rad/s. Meanwhile, the present CFD-DMB method under-predicted the displacements at barge amidships (Pt.9) at 6.98 rad/s, about 27%. One reason may arise from the limited mesh density in CFD modelling, which resulted in dependencies of free-surface wave modelling. The related convergence analysis was required for future uncertainty analysis.

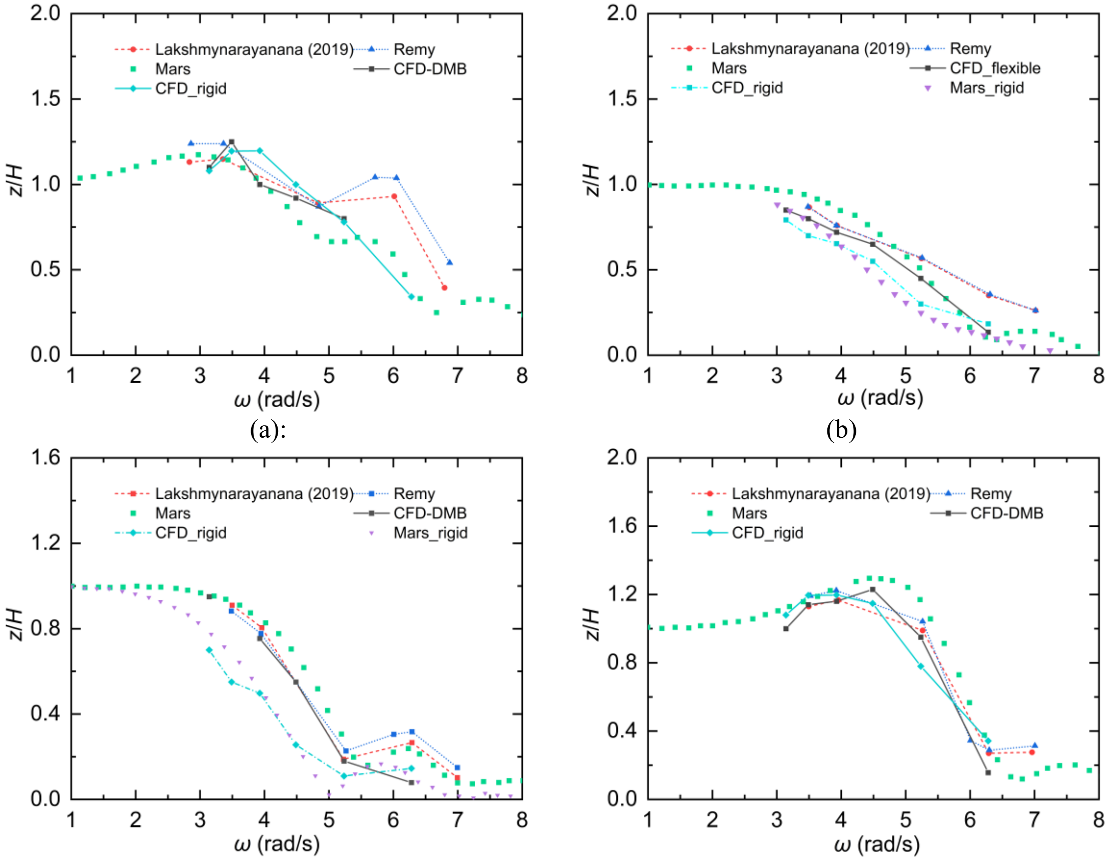

(a):

(b)

Figure 4.10: Validation on the displacements of barge segments and compared with the results from experiments (Remy et al. 2006), Mars (Lakshmynarayanana et al. 2019) and co-simulation (Lakshmynarayanana et al. 2019).

The VBM RAOs were calculated at barge amidships ($x/L = 0.5$) and compared to a 2-D linear hydroelastic analysis (Remy et al. 2006) and co-simulation results (Lakshmynarayanana et al. 2019), as shown in Fig. 4.11. By comparing the numerical results with the experiments, it is found that the general trend of the plots for the frequencies investigated was similar. Nevertheless, the relative magnitude of RAOs revealed significant differences close to resonant frequency (i.e., 5.25 rad/s). In general, the VBM was under-predicted by the present method among all wave frequencies, the magnitude was lower than that from co-simulation by about 6.5% and 12.4% by 2-D hydroelastic predictions.

Overall, the results from this validation exercise implied that the present CFD-DMB method was capable of predicting the vertical motions and loads of a very flexible structure to a good degree of accuracy.

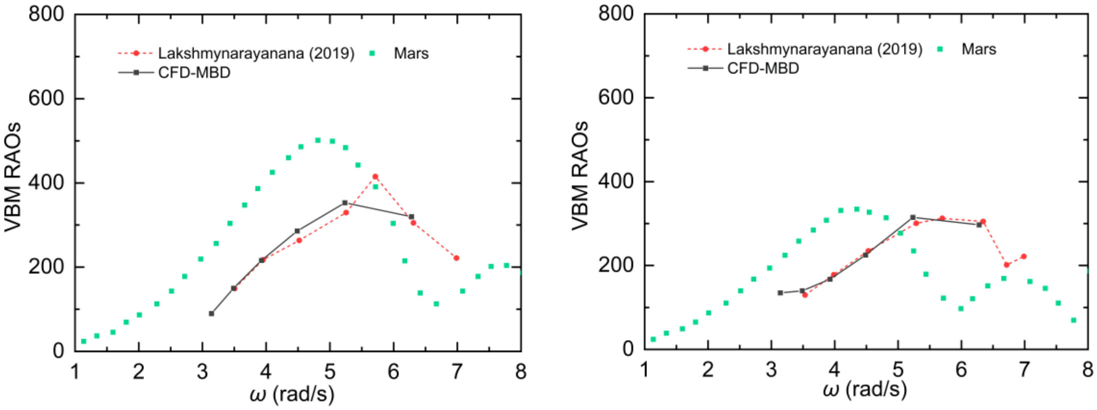

Figure 4.11: RAOs of the vertical bending moments of the flexible VLFS in heading waves ($x/L = 0.5$) and at barge section ($x/L = 0.66$).

4.4 Conclusion Remarks

Three validation studies were presented in this chapter to evaluate the numerical performance of the selected solvers.

In Chapter 4.1, the performance of beam model was evaluated between the FEA solver CalculiX and the multi-body dynamic solver MBDyn through an application of a simple cantilever beam. The beam bending behaviours, including deformation and bending moments, were examined.

In Chapter 4.2, a validation study was presented to assess the OpenFOAM code performance by investigating the vertical motions of a CTV in heading regular waves. The numerical predictions agreed well with the experimental results, and a GCI uncertainty study was applied to analyse the mesh and time-step sizes effect on the solutions. The GCI uncertainty results implied that the solution convergence was achieved for most cases; however, the mesh grid convergence always imposed larger error than the time-step. During the modelling procedure, the present OpenFOAM code posed stability issues while modelling at short wave cases, especially wave frequencies f_s was over $0.6\mathrm{rad/s}$. The model diverged due to the bad cell quality at the structural boundary layers. When the mesh cells were distorted significantly, the interpolation of these mesh cells became problematic, resulting in a local increase of numerical error and Courant number. Therefore, an advanced dynamic mesh technique, e.g., overset or sliding mesh, was recommended for future wave-structure problems with large motions.

In Chapter 4.3, the present CFD-DMB models were validated by applying a flexible barge on the free surface in head waves. The numerical results, including vertical displacements and symmetric bending moments, were computed using the CFD-DMB method shown favourable agreement with experimental measurements (Remy et al. 2006) and commercial co-simulation packages (StarCCM+ & Abaqus) results (Lakshmynarayanana et al. 2019). The numerical results were further compared to a 2D linear hydroelasticity theory, which found that the predictions using the CFD-DMB method shown improved results at the resonance period as it considered the nonlinearities and fluid damping. Overall, the results revealed that the present coupling technique was reliable and capable of future ship hydroelasticity analysis.

5 Hydroelastic Analysis of a Containership in Regular Heading Waves based on a CFD-FEA Coupling Approach using PreCICE

Most numerical studies on ship hydroelasticity relied on commercial coupling software or in-house codes; either a software license was required, or it was hard to reproducible. To extend the possibilities and test the performance of existing open-source FSI packages, in this chapter, a peer-to-peer coupling library "PreCICE" coupled OpenFOAM and CalculiX was first used to investigate the hydroelastic motion and loads of a containership (S175) in regular waves. The rest of this chapter was organized as follows: in Chapter 5.1, the FSI model setting ups and the methodology were discussed. Chapter 5.2 presented the dry and wet modal analysis to evaluate the structure model accuracy. In Chapter 5.3, the numerical results for the study on the dynamic motion of the flexible S175 ship in waves were presented and compared with another commercial FSI package and the experimental results. Both global ship motions and hydroelastic behaviour were included. The conclusions were drawn in the final section.

5.1 Model Description

In the present FSI study, a partitioned coupling scheme was applied to separate the solution domain into a fluid domain and structure domain and solving them iteratively. The detailed numerical methods of both fluid and solver solvers were described in the following sub-sections.

5.1.1 Ship Modelling

The benchmark S175 type of containership with a scale ratio of 1:40 was used in this study. The body plan of full-scale ship was shown in Fig 5.1. The main dimensions of the ship in the model- and full-scales were shown in Table 5.1.

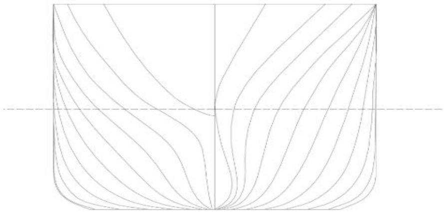

Figure 5.1: Body plane of the S175 hull (Jiao et al. 2021).

Table 5.1: Main properties of the S175 containership.

Ship Geometry description	Full scale	Model
Scale	1:1	1:40
Length between perpendiculars (L)	175 m	4.375 m

Breath (B)	25.4 m	0.635 m
Draft (T)	19.5 m	0.488 m
Displacement (Δ)	23,711 t	370 kg
Block coefficient (C_b)	0.562	0.562
Longitudinal centre of gravity (LCG) from after perpendicular	84.980 m	2.125 m
Vertical centre of gravity (KG) from base line	8.5 m	0.213 m
Transverse radius of gyration	9.652 m	0.241 m
Longitudinal radius of gyration	42.073 m	1.052 m

5.1.2 CFD Model

The finite volume mesh was generated by the mesh generation tool “SnappyHexMesh” based on a cell splitting and body fitting technique (Jasak et al. 2007). The numerical domain used to simulate ship motions in waves extended in three directions, i.e., -1.5L <x<2.0L, -1.0L<y<1.0L and -1.5L<z<1.0L, where L denoted as the ship length between perpendiculars (4.375m) (Tezdogan et al. 2015). The grids density at the free surface zone was progressively refined several times to fulfil the guideline from ITTC (2017) (Procedings 2014). According to these recommendations, a minimum of 120 cells per wavelength and 12 cells per wave height were used on the free surface in this study, as shown in Fig. 5.2 (Tezdogan et al. 2015). The choice of the K-omega SST turbulence model further required a more refined mesh at the area immediately around the ship hull, primarily maintained the adjacent wall layer thickness coordinate y+ close to 30 associated with the higher Reynolds number flow (Menter 1994).

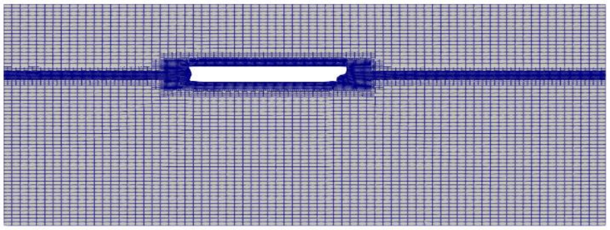

Figure 5.2: The front view of the computational wave domain.

The boundary conditions of the present CFD model were defined as follows. At the left boundary inlet, the velocity was prescribed as the incident wave and current, while the pressure was set as zero gradient. At the right boundary outlet, the current velocity outlet was applied to preserve the conservative of flux inside the computational domain. The boundary condition of the domain top part was set as atmosphere. The domain bottom boundary was set as symmetry plane which represented a deep-water condition as well as the lateral sides. The moving wall boundary condition with zero pressure gradient was defined on the surface of the ship hull.

5.1.3 Structural Model

A ship-beam segment model based on a beam-shell coupling approach which comprised a massless ship surface shell (including main deck) and a backbone beam, was built in the open-source FEA software CalculiX (Dhondt 2017). The hull surface was lengthwise cut for 20 sections, as shown in Fig. 5.3, and then discretized using 3-node triangular shell elements (S3), which in total 50,247 elements were used. The elements at hull surfaces were rigidly connected with the nodes at backbone beam, which allowed the forces and moments at the shell surfaces transferring to the beam nodes.

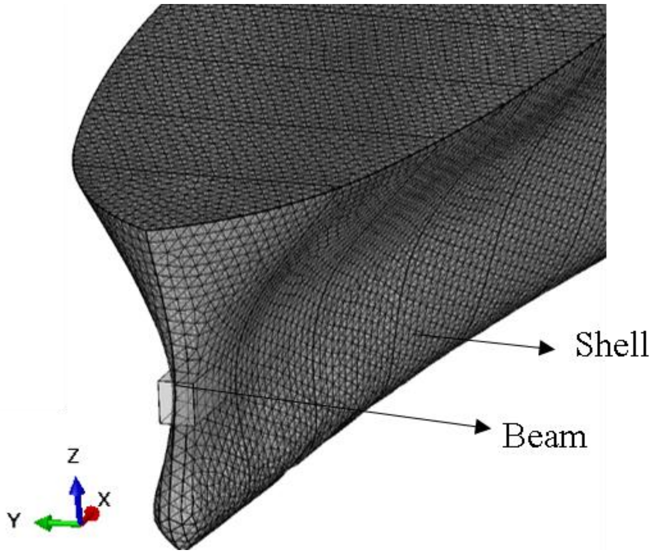

Figure 5.3: The virtual observation of the hull surface and beam discretization in CalculiX.

The backbone beam based on Timoshenko beam theory, whose governing equations were shown as below, was modelled using B32R beam elements.

The equations for Timoshenko beam with external loads can be expressed as given below:

Force equation

$$m(\mathrm{x})\frac{\partial^2 \mathrm{y}(x,t)}{\partial t^2}-\frac{\partial Q(x,t)}{\partial x}=f_3(x,t) \tag{5.1}$$

Moment equation

$$-\frac{\partial M(x,t)}{\partial x}+Q(x,t)-I\rho\frac{\partial^2 \Theta(x,t)}{\partial t^2}=0 \tag{5.2}$$

where $m(x)$ is body mass per unit length, $y(x,t)$ is displacement amplitude, $Q(x,t)$ is shear force, calculated by $Q(x,t) = GA\gamma(x,t)$, G is shear modulus, A is cross section area, $M(x,t)$ is bending moment, which has an equation of $M(x,t) = EI\, \partial\Theta(x,t)/\, \partial x$, where EI is the flexural stiffness, $f_3(x,t)$ is time dependent vertical environmental force per unit length.

It is worth noting that the B32R beam element was the preferred beam element of selections. It performed well for bending behaviour and avoided the shear locking and volumetric locking against other beam elements supported by CalculiX. The backbone beam was positioned at a height of vertical centre of gravity of ship model. The ship mass modelled as distributed point mass, which was placed on the beam elements as shown in Fig. 5.4 and Fig. 5.5. The material property of beam was defined as steel, i.e., elastic stiffness $\mathrm{E} = 210Gpa$ and Poisson ratio $v = 0.3$. The cross section of backbone beam was determined by calibrating the natural frequency of the beam to match with the second-node dry natural frequency of ship hull. The FE model was constrained for the y-axis translation and rotation by imposing constraints on the beam and shell nodes. Moreover, the beam center node was restrained in the direction of x-axis to avoid ship drift by the waves.

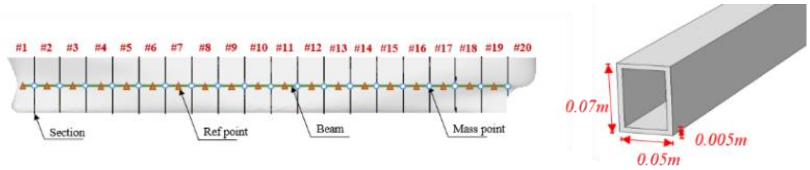

Figure 5.4: Ship backbone beam segement model settings.

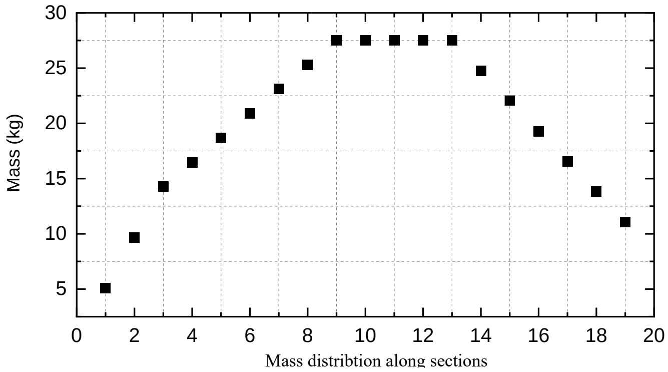

Figure 5.5: The mass distribution at each ship section along ship longitudinal axis.

5.2 Vibration Characteristics

5.2.1 Dry frequency analysis

The natural frequencies of the dry ship were estimated in vacuum, which assumed the free-free beam structure stayed in the absence of any external actions or internal damping. To avoid asymmetric effects (i.e., torsion or horizontal bending), the y-symmetry boundary conditions were applied for the FE model. The first three modes were calculated as listed in Table 5.2 and its deformation were shown in Fig. 5.6.

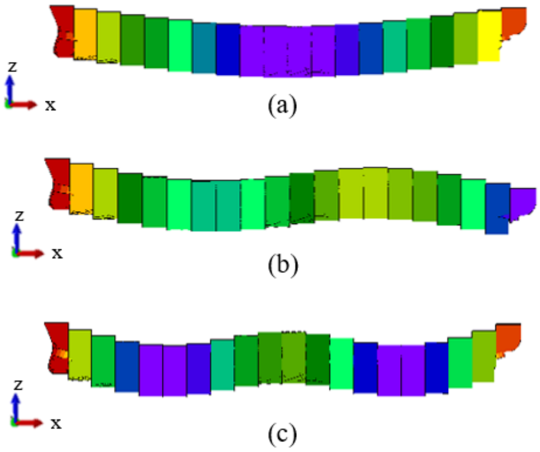

Figure 5.6: Dry ship natural frequency visualization.

When bending or torsional loads were not applied on the beam symmetry line, the beam may produce warping or non-uniform out of plane displacement. Although the warping effects due to the pure bending were small, a box-shaped beam section was assigned to the beam profile since this closed-type cross section was free from warping effects compared to the open sections. The beam thickness and section dimensions were determined by matching the second node natural frequencies of the ship-beam model with the full-scale ship. After calibration, the beam profile with a cross-section of $0.07\text{m} \cdot 0.05\text{m}$ and thickness 0.005m, was used through all later cases in this study.

5.2.2 Wet frequency analysis

An additional natural frequency estimation of the wet mode of hull was modelled based on a continuum-based fluid modelling approach using a commercial FEA software Abaqus/CAE 2020. In this type of application, the added mass effect was an important parameter to consider by modelling the surrounding infinite of water. The wet surface of ship hull was encapsulated in a fluid zone, and a pair of fluid-solid coupling surfaces were generated between the free surface and ship wet surface.

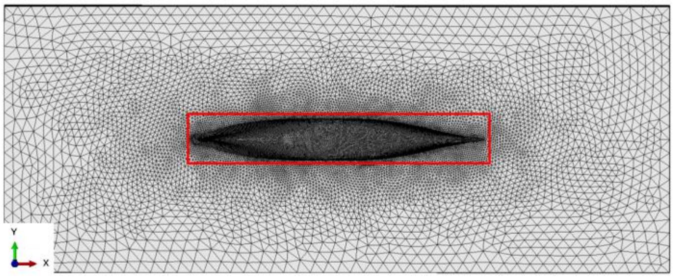

Figure 5.7: Acoustic fluid domain.

The acoustic medium, modelled by S4 acoustic element assigning with water density $1{,}025\mathrm{kg/m^3}$ was used to simulate the sea water condition. Figure 5.7 shows the dimension of the acoustic computational tank used in this study. It has $9.0\mathrm{m}$ in length and $6.0\mathrm{m}$ in width, and it is discretized in 46,589 number of acoustic elements. The mesh region adjacent to the ship was kept a consistent grid density to the ship surface mesh (shown in red square), and the mesh density was reduced outwards to the far field. Two boundaries were applied; a non-reflection boundary condition via a surface impedance for the outer surfaces of the domain to avoid the water reflection and a kinematic coupling boundary for the ship wet surface to ensure the displacement field in the structure was coupled with the fluid pressure field. The first three modal shapes of ship in wet frequency analysis were shown in Fig. 5.8.

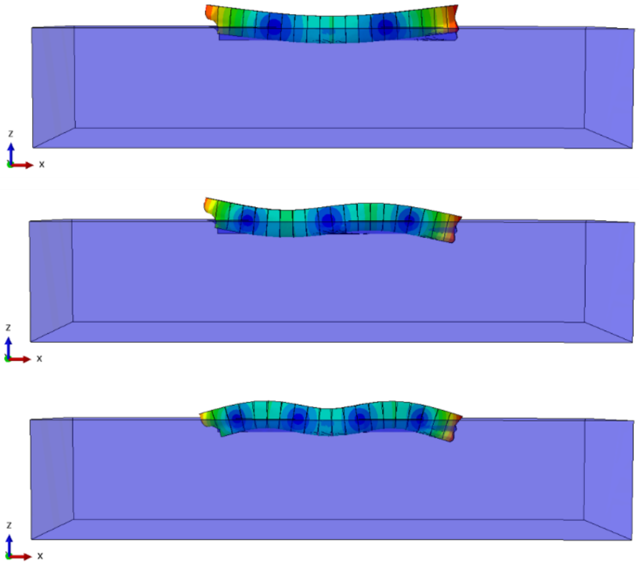

Figure 5.8: Wet ship natural frequency visualization.

Both dry and wet natural frequency models were solved using the SPOOLES solver. The results were shown in Table 5.2 and compared with the experimental results listed in Error columns. As expected, wet natural frequencies of the ship were significantly lower than dry natural frequencies due to the consideration of hydrodynamic added mass.

Table 5.2: Calibrate beam natural frequency properties and errors.

Order	Mode	Dry condition (Hz)	Error (%)	Wet condition (Hz)	Error (%)
1st	2-node	9.54	5.9%	8.17	7.6%
2nd	3-node	25.02	4.6%	21.28	6.6%
3rd	4-node	48.04	3.4%	40.70	5.9%

5.3 Results and Discussion

In this chapter, the flexible ship motions and corresponding hydroelastic behaviours of the S175 containership at wave length ($\lambda/L = 1.2$) with a forward speed of $F_n = 0.2$ were analysed. The case was run parallel using multi-nodes (80 cores) on HPC, the averaging time step was set as 0.002s. The simulation was run up to 5 complete wave periods for attaining stable results and the required physical time was about 300 hours.

5.3.1 Flexible ship motions in wave-structure resonant condition

The time series of flexible ship heave motions were monitored on the real-time displacement of the beam node close to the ship gravity centre, as shown in Fig. 5.9. The flexible ship responses of current ship-wave matching resonance case showed a slightly lower value at the peak by about 15% when compared to the rigid body cases.

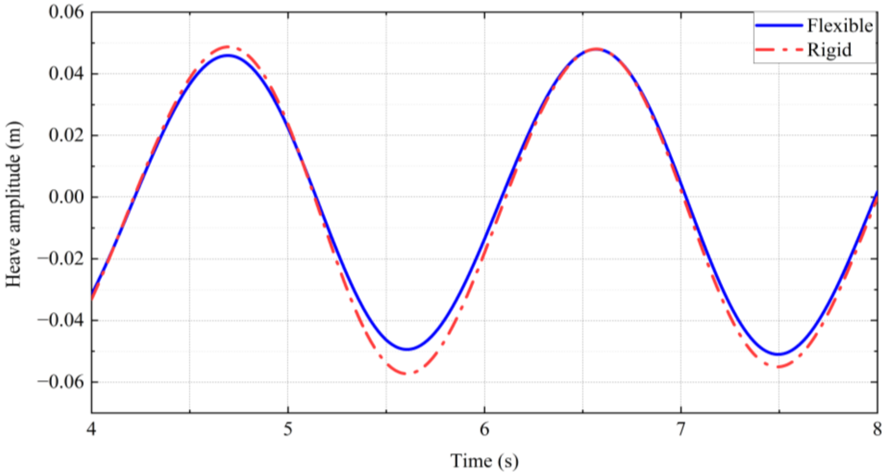

Figure 5.9: Calculated head motion at $\lambda/L = 1.2$.

In addition, the corresponding pitch motions of both flexible and rigid body cases were presented in Fig. 5.10. Both heave and pitch results were in regular and sinusoidal shapes, which indicated the suitability of the present solvers on seakeeping.

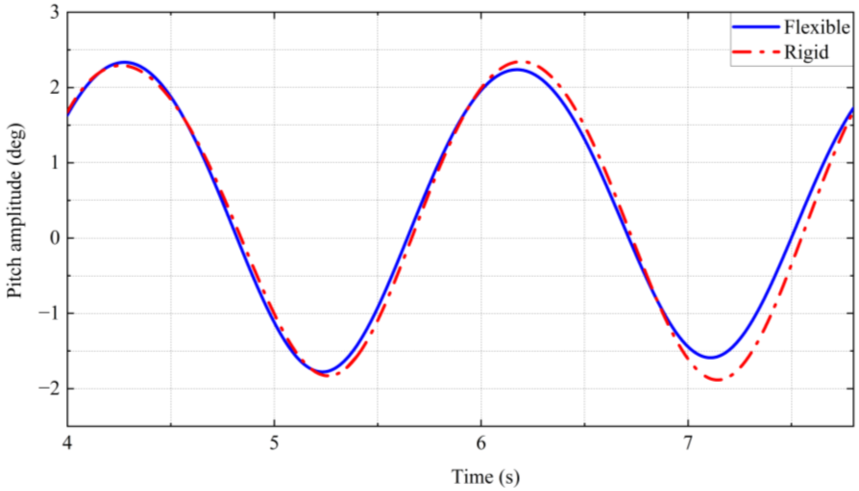

Figure 5.10: Calculated pitch motion at $\lambda/L = 1.2$.

It is worth mentioning that the structure solver CalculiX does not have an internal rotational degrees of freedom (Dhondt 2017). Therefore, the pitch angle was calculated using the relative difference ratio between two adjacent nodes of vertical and horizontal distances based on a linear approximation equation as given the Equation below.

$$\theta = \arctan\left(\frac{z_c - z_{c+1}}{x_c - x_{c+1}}\right) * \frac{180}{\pi} \tag{5.3}$$

where, θ is the pitch angle in degree, subscript c points to the beam node at ship gravity centre, and $c + 1$ means the corresponding adjacent node sequence. The raw pitch data is given in radians, therefore, a factor of $180/\pi$ is multiplied to convert it into degrees.

The RAOs of ship motions were estimated by using the motion data and wave amplitudes from the last two stable wave periods. These RAO results were then compared with the co-simulation results from (Jiao et al. 2021) and the experimental data from (Chen et al. 2001), as shown in Fig. 5.11. The heave (z) and pitch (θ) motions were non-dimensionalized by z/ξ and $\theta/k\xi$, where ξ was estimated wave amplitude. From Fig. 5.11, the present heave RAOs were found to be 16.3% lower than the co-simulation results and 18.0% lower than the experimental data. The deficiencies may be caused by the inconsistent selections of coupling methods, structure solver demonstrations, and the time step resolutions between the existing solvers and comparatives. A comprehensive convergence test including mesh densities and time step sizes will be studied in the future. Moreover, the calculated pitch RAOs presented a good agreement with the experimental data.

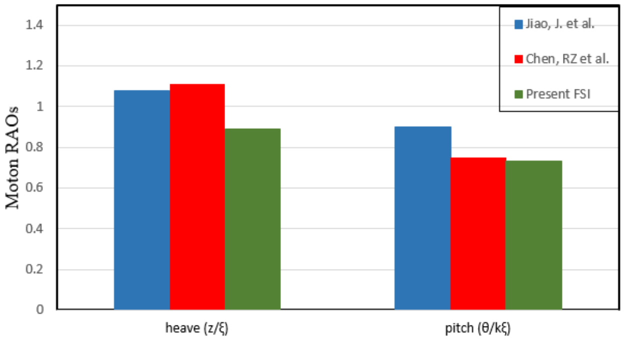

Figure 5.11: Ship RAOs at $\lambda/L = 1.2$ compared with literatures.

5.3.2 Flexible ship VBM in wave-structure resonant condition

The hogging and sagging peak values at each ship sections in the case of $\lambda/L=1.2$ were further compared with the co-simulation results (Jiao et al. 2021), as shown in Fig. 5.12. The VBM (M) was non-dimensionalized by $M/\rho g L^2 B\xi$. As can be seen in Fig. 5.12, the results indicated similar trends of the hogging and sagging curves between the present FSI model and the co-simulation model, except when the peak values were lower in general as noticed above. From Figure 15, both models successfully captured the asymmetry behaviour of hogging and sagging moments along the ship sections. The peak value of hogging VBM occurred at ship 10th section, which was evidenced from both the present FSI and co-simulation model. However, the position of the trough peak values of sagging VBM from co-simulation occur at 9th section compared with 10th section from the present model.

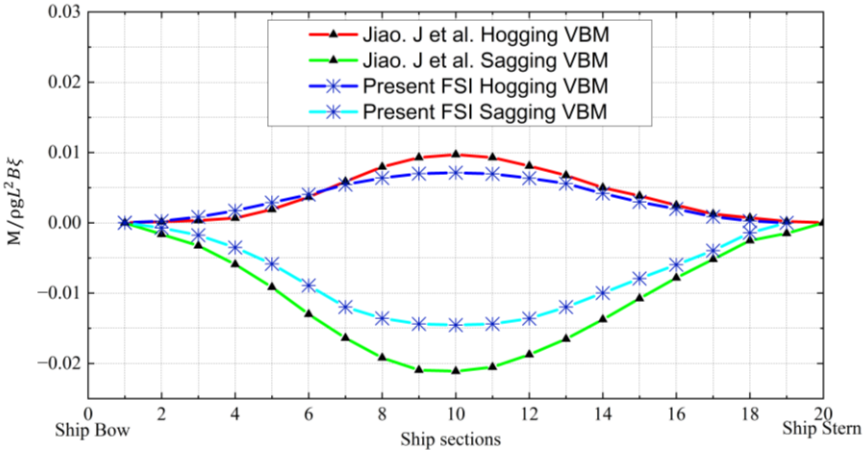

Figure 5.12: Comparisons of VBM at ship longitudinal sections.

The peaks VBM were extracted at the amidship section and compared with the results from co-simulation (Jiao et al. 2021), as shown in dashed lines in Fig. 5.13. In addition, the first harmonic of wave bending moment was extracted from the total VBM component by using low pass filtering, and its peaks were shown in solid lines in Fig. 5.13. Overall, the magnitudes of these peak values from the present FSI model were generally lower than the results from the co-simulation.

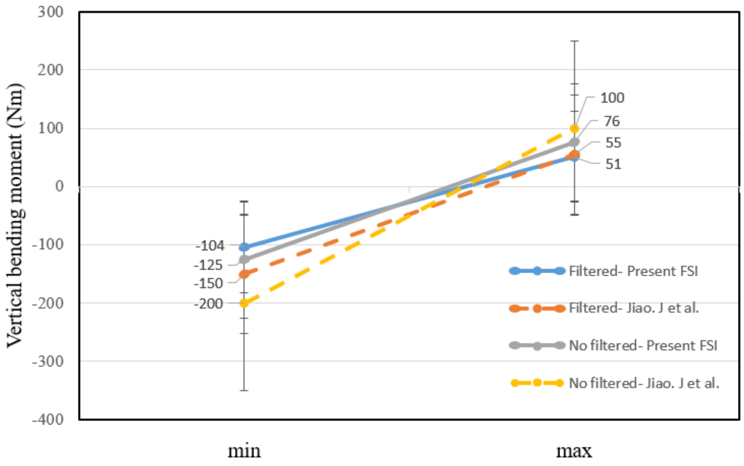

Figure 5.13: Comparisons of VBM peak values**.**

5.4 Concluding Remark

In this study the seakeeping and hydroelastic behaviour of a flexible S175 containership has been modelled through an open-source coupling FSI framework. The resonance case of the ship in question in head waves was investigated and validated by comparing the ship motions and VBM results with the experimental measurements (Chen et al. 2001) and co-simulation FSI packages results (Jiao et al. 2021). The vertical motions predicted by the present FSI model generally agreed well with experimental results, except the heave RAOs. The peak values of ship total VBM and hogging/sagging moments showed similar trends with the co-simulation results. In general, this study showed the present FSI codes capacity to predict the hydroelastic behaviour of a containership in heading waves. Future pieces of work will focus on more extensive studies on different wave conditions as well as ship forward speeds and on the extreme wave effects on flexible ship responses by performing the models in short-crested irregular waves.

It is believed that the present FSI model will exhibit more advantages over the traditional rigid-body methods currently used in the ship seakeeping field.

6 A Fully Coupled CFD-DMB Approach on the Ship Hydroelasticity of a Containership in Extreme Wave Conditions

The research using transient FSI simulations to investigate ship hydroelasticity in extreme wave conditions was very limited in number and scope. The reasons for this mainly stem from the computational burdens of determining maximum values of ship responses in irregular waves through direct simulation using Navier-Stokes equations. In this work, the dynamic motions and slamming loads of a flexible ship in extreme wave conditions were studied in focused wave conditions based on a fully coupled CFD-DMB model. It is expected that the results obtained from this improved and validated numerical tool can provide a precise and more detailed insight into the physical phenomena of the ship dynamic motions and its hydrodynamic loads in real sea states. The results proposed in this study could also help to access the structural integrity of the ship longitudinal strength, which serves an improved technique by which to evaluate unconventional ship designs.

The rest of this chapter is organised as follows: in Chapter 6.1, the numerical setting up and the methodology used in the present study are discussed. In Chapter, the verification and validation studies are presented for focused waves and the present CFD-DMB model. In Chapter 6.3.1, the numerical results of the study on the dynamic motions of a flexible S175 ship in regular wave conditions are presented. In Chapter 6.3.2, a comprehensive comparison of the ship global motion and hydroelastic behaviours between focused and regular waves is presented. The discussion and conclusion are drawn in the final section.

6.1 Model Description

The numerical simulations were performed using the same S175-type containership model as Chapter 5. Three-dimensional view of the ship is shown in Fig. 6.1. This type of ship geometry has been commonly used in the literature for ship hydroelasticity research. These studies include the BEM-FEM coupling research by (Kim et al. 2014), the CFD-FEA coupling research by (Takami et al. 2019, Lakshmynarayanana et al. 2020, Jiao et al. 2021, Jiao et al. 2021, Wei et al. 2022) as well as some experimental results as reported by (Chen et al. 2001). Only the bare hull was modelled for the seakeeping investigations in this study.

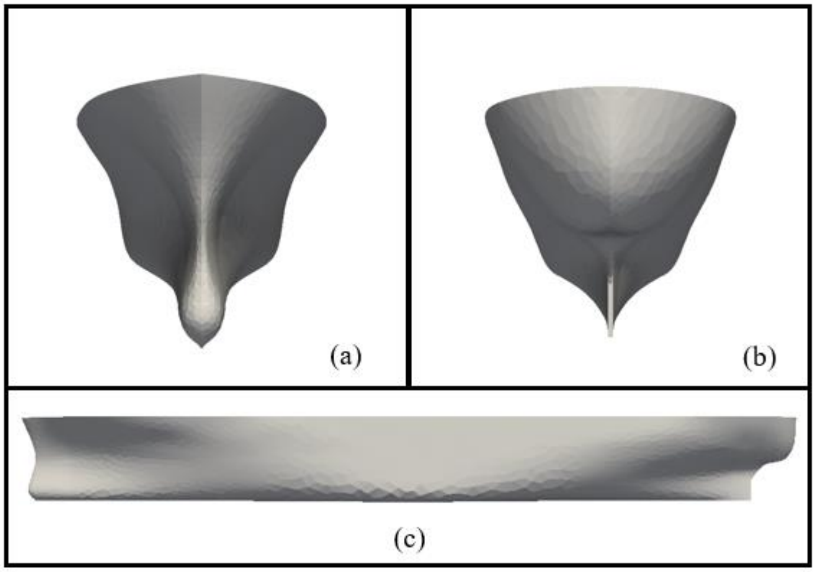

Figure 6.1: Three dimensional view of the S175 geometry: (a) Ship bow, (b) Ship stern, (c) Ship geometry.

In this research, an array of six pressure gauges (P1, P2, P3, P4, P7, P9) were placed on the bow flare and bow bottom areas for bow wave pressure measurement to investigate the impact wave loads on the ship when sailing in harsh weather conditions, as shown in Fig. 6.2(a). Moreover, an array of three pressure gauges (P5, P6, P8) were arranged at the side of the hull to measure the slamming pressure at the starboard, as shown in Fig. 6.2(b).

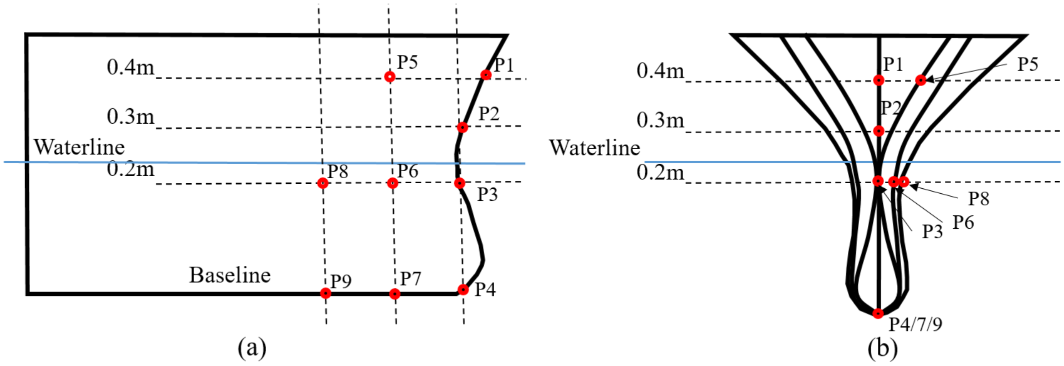

Figure 6.2: Pressure gauge arrangements: (a) Slamming pressure monitoring points at side view, (b) Slamming pressure at front view.

6.1.1 CFD Model

The finite volume mesh was generated using the OpenFOAM default mesh generation tool “SnappyHexMesh” based on cell splitting and mesh fitting techniques (Jasak et al. 2007). A uniform background mesh was initially generated and used to project and snap cells onto the geometry, and then the mesh refinements can flexibly be specified on edges, surfaces and volumes to obtain optimum geometry feature resolutions. The numerical domain used in this study simulates ship motions in deep-water conditions, which extends in the three dimensions, i.e., $-1.5L < x < 2L$, $-0.6L < y < 0.6L$ and $-1.5L < z < 0.5L$, where L refers to the ship length between perpendiculars. The grid density at the free surface is progressively refined until it fulfilled the guidelines from (ITTC 2017), in which a minimum of 100 cells per wavelength and 12 cells per wave height were used on the free surface modelling in this study, as shown in Fig. 6.3(a). To ensure that the high Reynolds number flow features are approximately captured, the grid density at the area around the ship hull is further refined several times with boundary layers, primarily maintains the adjacent wall layer-thickness coordinate $y+$ close to 30. It is worth noting that the proper wall functions were implemented for the hull patch surfaces to model the approximate wall behaviour when the adjacent layer thickness stayed in a log-law region. The numerical domain with a wave height of 0.12m and encounter wave frequency of 5.581Hz ($\lambda/L = 1.1$) is chosen as a representative case, which is displayed in Fig.6.3 with a general view of the computational mesh and mesh-refinement zones.

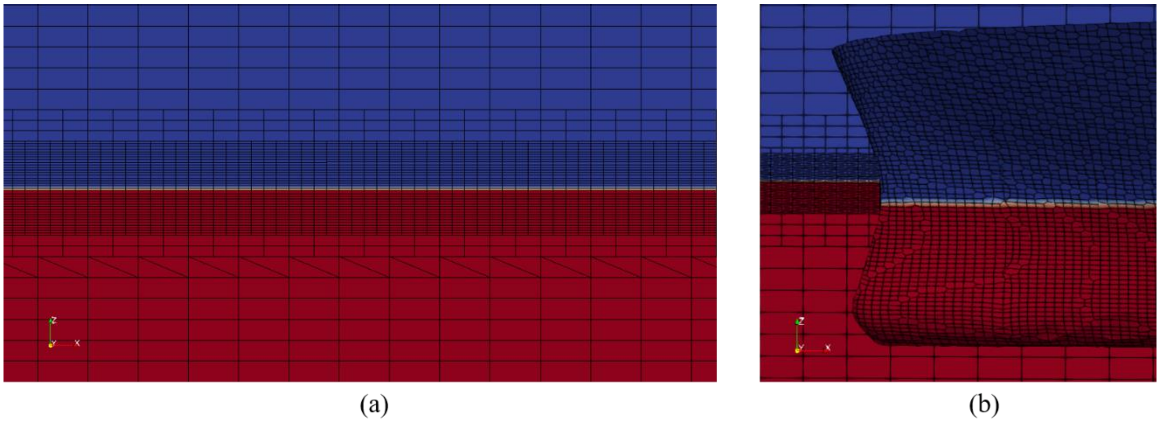
(a)
(b)

Figure 6.3: Mesh refinement: (a) Near the free surface, (b) Details at the ship bow.

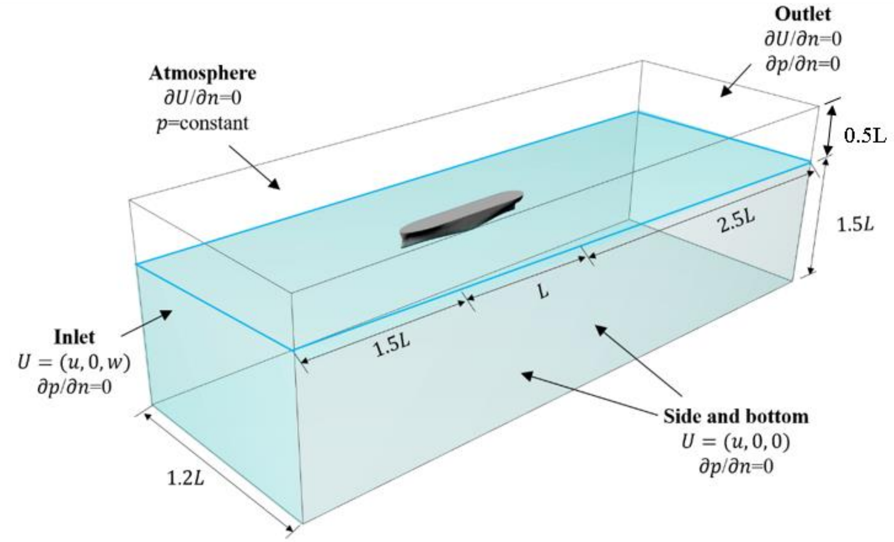

Figure 6.4: The numerical domain with the applied boundaries for the deep-water case.

The boundary conditions in the present CFD study are shown in Fig. 6.4 as follows: At the left boundary inlet, the velocity inlet was prescribed as the incident wave and current, while the pressure was set as zero gradient. At the right boundary outlet, the current velocity outlet was applied to preserve the conservative of flux inside the computational domain. The boundary condition of the domain top part was set as atmosphere. The lateral sides were set as symmetry planes to avoid wave reflection at the boundaries. The bottom boundary was set as a symmetry plane for deep-water modelling. The moving wall boundary condition with zero pressure gradient was defined on the surface of the ship hull.

The multiphase solver interFoam used in this study is based on a finite volume method that solves the unsteady RANS equations in an iterative manner. The density ρ and the kinematic viscosity ν of the fluid in simulation are reported in Table 6.1. In the numerical model, the convection terms were discretized with a Gaussian linear upwind scheme, whereas a second-order Gaussian linear corrected scheme was adopted for the diffusive terms. The turbulence model selected for the simulation is the shear stress transport (SST) model from Menter (1994), which blends the best features of the near-wall accuracy of the $k-\omega$ model and the free-stream accuracy of the $k-\varepsilon$ model. The temporal discretisation was performed with a first-order backward Euler scheme. PIMPLE (a combination of Pressure Implicit with Splitting of Operator (PISO) and Semi-Implicit Method for Pressure-Linked Equations (SIMPLE)) was utilised to solve the pressure velocity coupling equations.

Table 6.1: Physical properties.

	Water	Air
ρ	$998.8\ \mathrm{kg/m^3}$	$1.0\ \mathrm{kg/m^3}$
ν	$1.337\times10^{-6}\ \mathrm{m^2/s}$	$1.48\times10^{-5}\ \mathrm{m^2/s}$

6.1.2 Structural Model

The deformable ship hull was divided into 20 sections whereas a stiffness matrix based on the Euler-Bernoulli beam theory, equivalently representing the structure's stiffness, was employed to connect the neighbouring sections. In its numerical representation in MBDyn, the distributed mass of each ship sections was modelled as a lumped mass point located at its centre of gravity according to the mass distribution data from (Jiao et al. 2021), as shown in Fig. 6.5 and 6.6. A uniform beam stiffness was applied with vertical bending stiffness which is shown in Figure 8. The mass moment of inertia, I_{yy}^*, I_{zz}^* and I_{pp}^* of each ship section was calculated based on the simplified approach from Bakti et al. (2021). In their approach, the moment of inertia of each section (I_y, I_z, I_p) was calculated by the product of the first moment of area and the centroidal distance of the area from the give axis. The parallel axis theorem was applied when the centre of the ship cross-section was not coincident with the beam node. Afterwards, the moment of inertia can be calculated by using geometric properties of the cross-section by multiplying a factor of a, such that $I_{yy}^* = a * I_y$. The factor $a = 8.0$ was used in the study, which was determined by matching the first two natural frequencies of the vertical bending modes of the beam with the values calculated by FEM. The material property of the beam was defined as steel, i.e., elastic stiffness $E = 210\mathrm{Gpa}$ and Poisson ratio $\upsilon = 0.3$. In this study, the structural damping was estimated approximately as 1% of the critical damping, as recommended by (Bishop et al. 1986).

The DMB model in the present study was constrained for the y-axis (no sway) translation and rotation about the x-axis and z-axis (no roll and yaw) by imposing total joint elements among beam nodes. Moreover, another set of total joint elements was employed to restrict the DMB model in the direction of the x-axis to prevent the longitudinal drift caused by the wave and current. Based on the above design, the elastic deformation of the ship hull is affected by the equivalent beam properties and restricted by the constraint equations.

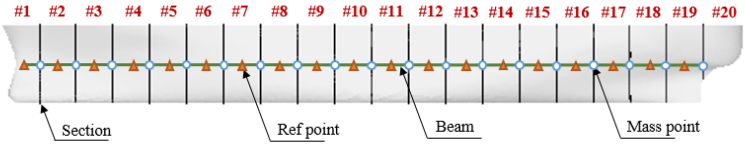

Figure 6.5: Arrangement of ship model view from middle longitudinal plane.

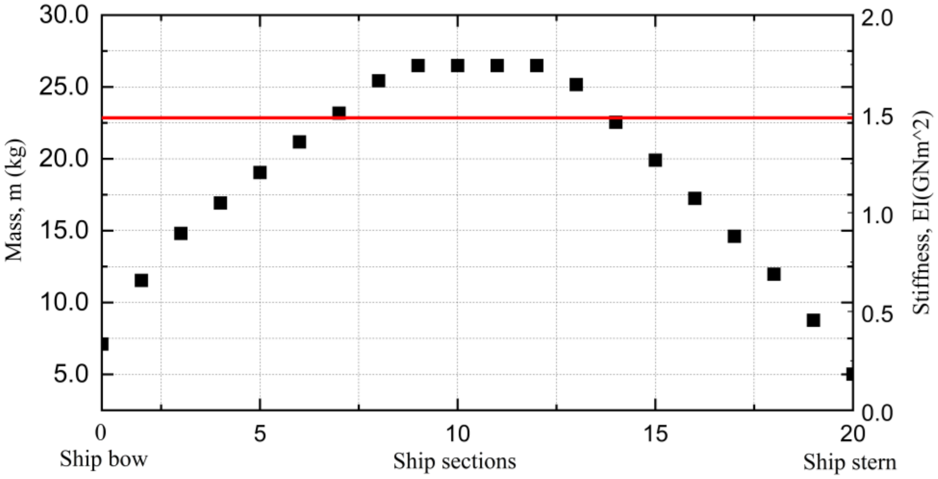

Figure 6.6: Longitudinal distribution of mass and uniform vertical bending stiffness.

6.1.3 Vibration characteristics

Before the hydroelastic computation, the modal analysis of the DMB beam model was conducted using Arpack solver in MBDyn software to provide information about beam vibration behaviours, such as the natural frequencies and modal shapes in the dry condition. The beam was assumed in a vacuum condition, and the elastic behaviours were considered by the multi-body dynamic beam theory with equivalent beam stiffness. The beam section profiles (including section dimensions and thickness) were calibrated by matching the first three modes' natural frequencies with the natural frequencies of the real ship from experiment (Jiao et al. 2021). The obtained natural frequencies for the first three orders of vertical bending mode of the model in dry condition are summarised in Table 6.2, and the corresponding mode shapes are shown in Fig. 6.7. After the calibration, the closed beam profile with a closed cross-section of $0.08m \times 0.05\text{m} \times 0.005\text{m}$ was used throughout all later cases in this study.

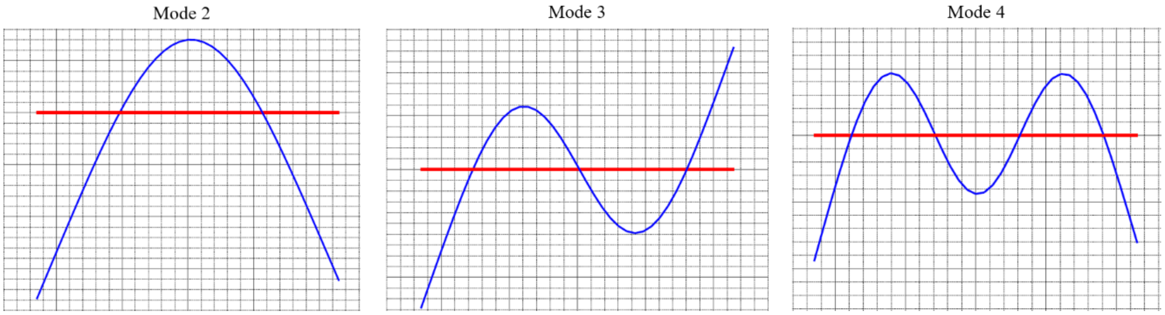

Figure 6.7: Modal analysis of the DMB beam model with modal shapes at 2nd, 3rd and 4th order.

Table 6.2: Calibrated beam natural frequency properties and errors.

Order	Mode	f_b(Hz)	f_s(Hz)	Error(%)
1st	2-node	10.140	10.154	0.112
2nd	3-node	26.116	26.241	0.482
3rd	4-node	49.136	49.747	1.246

where, f_b(Hz) denotes MBD beam natural frequency and f_s(Hz) is the ship natural frequency from experiment (Jiao et al. 2021).

6.2 Verification and Validations

The following chapters will present two verification studies. In Chapter 6.2.1, a sensitivity study is presented on the focused wave generation based on the "NewWave theory" (Chapter 3.1.3.2), and the numerical results are compared with the analytical solutions. In Chapter 6.2.2, a verification study is carried out on the effects of mesh grids and time-step sizes on the present CFD-DMB coupling method at the wave-ship resonance condition ($\lambda/L = 1.2, H = 0.12\text{m}$). The results including dynamic ship motions (heave and pitch) and vertical structural loads (VBMs), are analysed in order to justify the correctness and accuracy of the present FSI model.

6.2.1 Sensitivity Study of Focused Wave Generation

The presence of uniform flow poses additional difficulties in modelling focused wave groups in CFD due to the wave-current interaction. Similar numerical studies presented by Zhang (Zhang et al. 2014), Markus (Markus et al. 2013) and Li (Li et al. 2012) proved that currents significantly change the focused wave elevations, peak wave period, focal time and position. However, such wave-current coupling effects are not one of the aims of this study, the focused wave group with current was generated based on the modified "NewWave theory" and the focused wave height and peak wave period were then calibrated accordingly to meet the desired focused wave shape.

In this verification study, a 2D numerical wave domain extends into two dimensions of $-9\text{m} < x < 11\text{m}$, $-6\text{m} < z < 2\text{m}$. A focused wave group was generated with the significant wave height of $H_s = 0.12\text{m}$, and the wave peak period is chosen as $T_p = 1.78$s in the model-scale. The uniform current speed was applied at the boundary inlet with a value of 1.80m/s, which implies the ship's forward speed of $Fn = 0.275$. The focal position was set as $x = 0.0$m and the focal time was set to be 15.0s. The frequency band between 0.125Hz to 2.0Hz and 50 individual wave components were used to generate this focused wave group. The mesh information of the mesh convergence study was summarized in Table 6.3.

Table 6.3: CFD mesh details of three mesh densities on focused wave generation.

Mesh grid	Coarse	Medium	Fine
x axis	$\Delta x = L/80$	$\Delta x = L/100$	$\Delta x = L/150$
z axis	$\Delta z = H_s/8$	$\Delta z = H_s/10$	$\Delta z = H_s/18$
Aspect ratio ($\Delta x/\Delta z$)	3.209	5.135	6.419
Grid number	10,298	21,462	37,814

To verify the quality of focused wave modelling, the discretisation error from mesh grids and time steps are studied and summarised in Tables 6.4 and 6.5. The numerical results of wave elevations are further compared with the analytical solution of a focused wave group without current as shown in Fig. 6.8. The figure shows that the simulated focused wave preserves favourable wave shapes, and the peak wave elevation is focused at the focal position and time, as desired. With the consideration on the computational cost, it was concluded that the medium size of mesh and time step of 0.0015s was the optimum choice to generate the waves in this study.

Table 6.4: Grid convergence test studies with three mesh densities.

Mesh grid	Coarse	Medium	Fine	Analytical
Maximum wave height (m)	0.0770 (-6.67%)	0.0775 (-6.06%)	0.0789 (-4.36%)	0.0825
Trough to rough period (s)	1.620 (+6.54%)	1.615 (+6.19%)	1.595 (+5.07%)	1.514

$H_s = 0.12\text{m}$ $T_p = 1.78s, U = 1.80\text{m/s}$ and $\Delta t = 0.0015\text{s}$.

Table 6.5: Time convergence test studies with three time-steps.

Time step	0.001s	0.0015s	0.002s	Analytical
Maximum wave height (m)	0.0785	0.0775	0.0736	0.0825

	(-4.84%)	(-6.06%)	(-10.7%)	
Trough to rough period (s)	1.600 (+5.37%)	1.615 (+6.19%)	1.640 (+7.68%)	1.514

$H_s = 0.12\text{m}\ T_p = 1.78\text{s}, U = 1.80\text{m/s}$ and medium mesh.

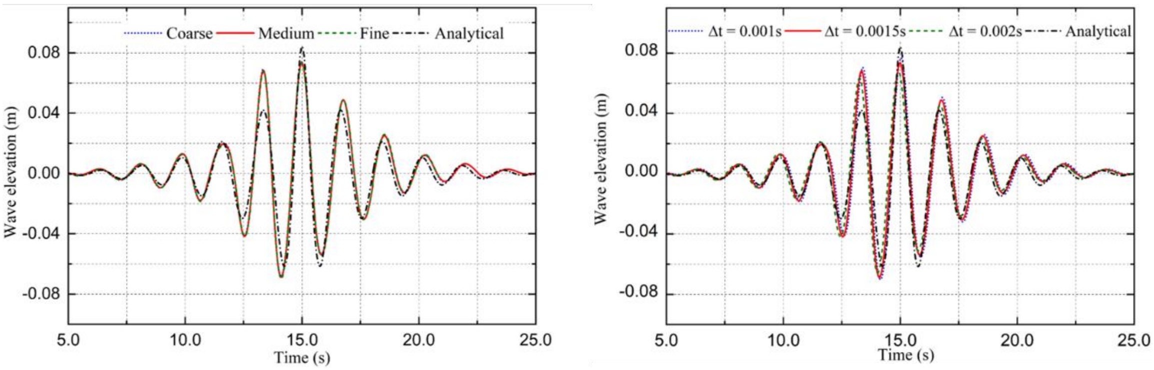

Figure 6.8: Mesh and time step convergence test of focused wave generation ($H_s = 0.12$ m $T_p = 1.78$ s): meshes(left), time steps(right).

6.2.2 Sensitivity Study on Flexible Ship in Regular Waves

Prior to present analysis of the CFD-DMB model of ship responses in different wave conditions, it is necessary to conduct related convergence and uncertainty analyses of the FSI model to verify the coupling framework performance. As Huang et al. (2022) pointed out, the uncertainties in the modelling of fluid dynamics by a CFD solver are generally much larger than the uncertainties associated with the structural responses by the structural solver. Therefore, in this chapter, a verification study is conducted in the CFD solver by changing three different mesh densities and three time-steps (details shown in Table 6.6).

The ship–wave resonant frequency condition ($\lambda/L = 1.2, H = 0.12\text{m}$) was studied because large motions and loads tend to cause the largest numerical errors (Tezdogan et al. 2015). It is worth mentioning that the change of gird resolution was only applied on the free surface region, whereas the mesh discretization was not altered in the background mesh.

Table 6.6: CFD mesh configuration of three mesh densities.

Mesh grid	Coarse	Medium	Fine
x axis	$\Delta x = L/120$	$\Delta x = L/120$	$\Delta x = L/120$
z axis	$\Delta z = H_s/6$	$\Delta z = H_s/11$	$\Delta z = H_s/20$
Grid number (million)	2.85	3.68	4.84

The simulated time series of the heave and pitch motions and the VBMs at the amidship section ($L/2$ from FP) by the three different grid densities and time steps are comparatively shown in Fig. 6.9-6.11. The time series of the flexible ship heave motions were monitored on the real-time displacement of the beam node on the ship at LCG. It is worth noting that the structure solver MBDyn does not have an internal rotational degrees of freedom (Masarati et al. 2014). The pitch angle is calculated using the relative difference ratio between two nodes, at ship bow and LCG, based on a linear approximation equation, as given in Eq. 6.1.

$$\theta = \arctan\left(\frac{z_c - z_b}{x_c - x_b}\right) * \frac{180}{\pi} \tag{6.1}$$

where θ is the pitch angle in degree, subscript c pointes to the beam node at ship LCG, and b denotes the front node of beam. The raw pitch data is given in radians, therefore, a factor of $180/\pi$ is multiplied to convert it into degrees.

Figures 6.9 and 6.10 show that the time-series of the heave and pitch signals from three different mesh densities and time-steps, respectively. The results by different grid densities are very close, although the medium and coarse meshes slightly underestimate the heave peaks. Figure 6.11 shows the simulated time histories of the ship VBMs among different mesh resolutions and time-steps. The data of wave-induced VBMs were filtered by the static still-water bending moment (SWBMs) from the total VBMs. The VBM signals in Fig. 6.11 have shown similar shapes with the numerical results from (Iijima et al. 2008), in which a strong asymmetry between sagging and hogging values exist due to the nonlinearity. To better understand the influence of waves on the high-frequency vibration characteristics, a fast Fourier transform algorithm (FFT) was applied to process the VBMs signals, and the results are shown in Fig 6.12. The main peak frequencies can be clearly observed from both figures, which implies the excitations from the encounter wave frequency, while the high frequency components can be captured up to ninth order, which is denoted as the springing effects. It has to be noted that the high frequency components are better recorded in fine mesh condition, but in general the extreme VBMs can be well estimated using medium mesh with less than 4.6% of difference, as compared to fine mesh.

All simulations were performed by using the Archie-West UK (HPC) facility with 40 Intel Xeon 2.0 GHz cores. The average time for the regular wave case to obtain 20 stable periods consumed approximately 120 physical hours, and it will increase while running for focused wave cases.

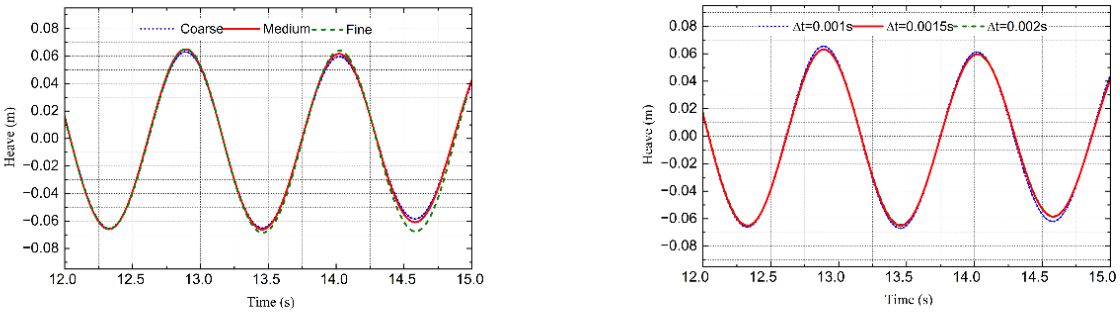

Figure 6.9: Time series of heave motions among: three mesh densities (left), three time-steps (right).

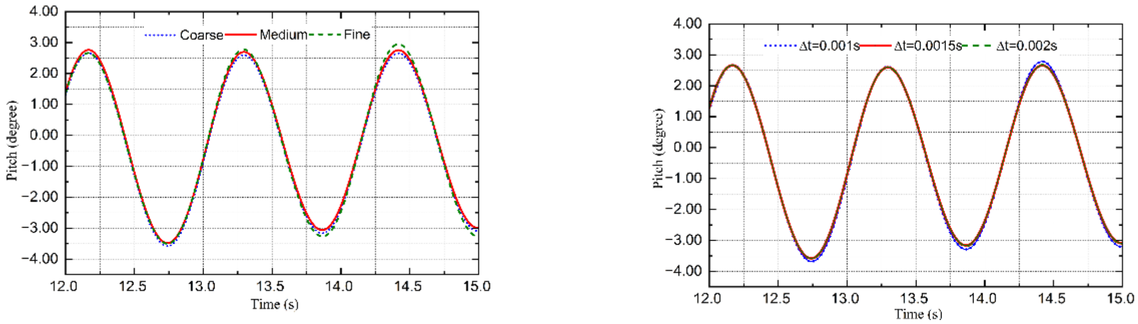

Figure 6.10: Time series of pitch motions among three mesh densities (left), three time-steps (right).

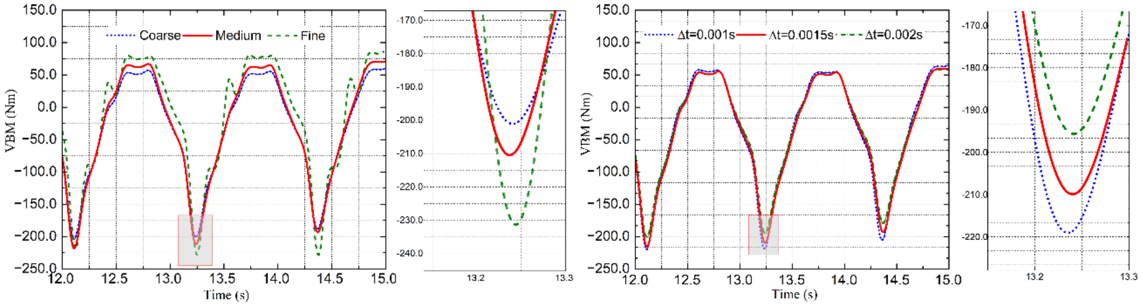

Figure 6.11： Time series of VBM components at amidship among: three mesh densities (left), three time steps (right).

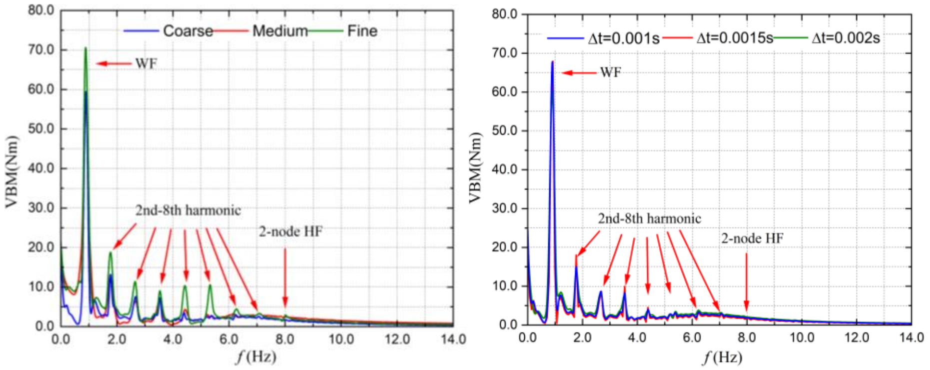

Figure 6.12: Frequency analysis of VBM components at amidship among three mesh densities (left), and three time-steps (right).

6.3 Results

6.3.1 Flexible ship behaviours in regular wave conditions

In this chapter, the predicted global ship motions i.e., heave, pitch and VBMs of the S175 ship model, are presented in different wave conditions based on the CFD-DMB method. The presentation of these results is fundamental for the subsequent focused wave analysis. There are five different incident wavelengths ranging from (λ/L=0.9 − 1.6) with a constant wave height of $H = 0.12$m, involved in this study. The detailed wave parameters are summarised in Table 6.7.

Table 6.7: Regular wave parameters.

Case IDs	1	2	3	4	5
Wave height (H, m)	0.12	0.12	0.12	0.12	0.12
Wavelength (λ/L,1)	0.9	1.0	1.2	1.4	1.6
Wave frequency ($\omega, rad/s$)	3.845	3.753	3.426	3.172	2.654
Speed (F_n, 1)	0.275	0.275	0.275	0.275	0.275
Encounter frequency ($\omega_e, rad/s$)	6.829	6.338	5.581	5.280	3.947
Wave steepness (H/λ, 1)	0.030	0.027	0.023	0.019	0.017

The encounter waves for the ship sailing in sea state 6 with different wavelengths (i.e., $\lambda/L = 0.9, 1.0, 1.2, 1.4, 1.6$) measured at P2 are shown in Figure 6.13. As seen from the wave results, the time series of the monitored waves preserved shapes well with less than 6.1% of wave height dissipation while propagation, which confirms the capability of the developed CFD wave generation technique.

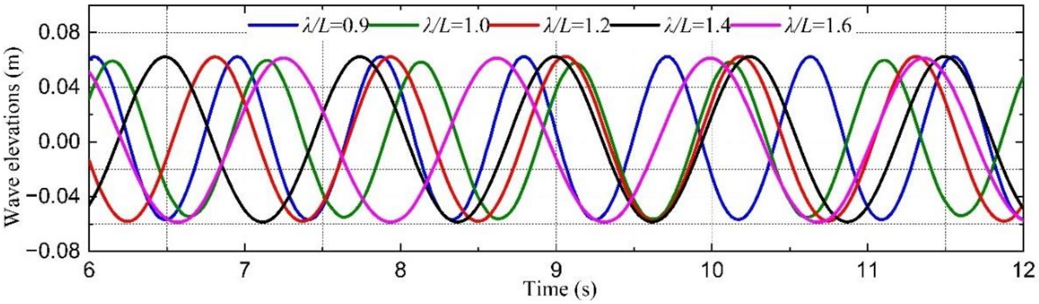

Figure 6.13: Time series wave elevations plots at different wavelengths, measured at P2.

6.3.1.1 Flexible Ship Motions

The original time series of the flexible ship motions including heave and pitch among different wavelengths are shown in Fig. 6.14 and 6.15. As can be seen in the figure, the vertical motion signals of the ship are all sinusoidal at any wave conditions which present the same sinusoidal characteristics of the induced waves. The largest heave and pitch motions is observed at the wave condition of λ/L=1.4.

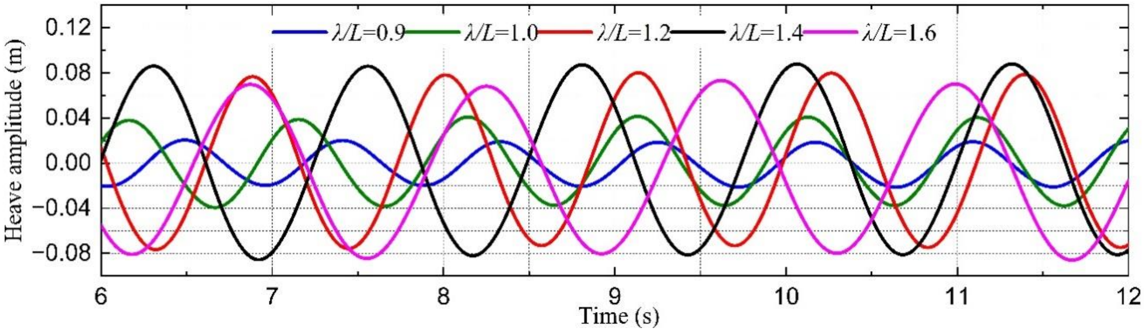

Figure 6.14: The time series of ship heave motions at different wavelengths.

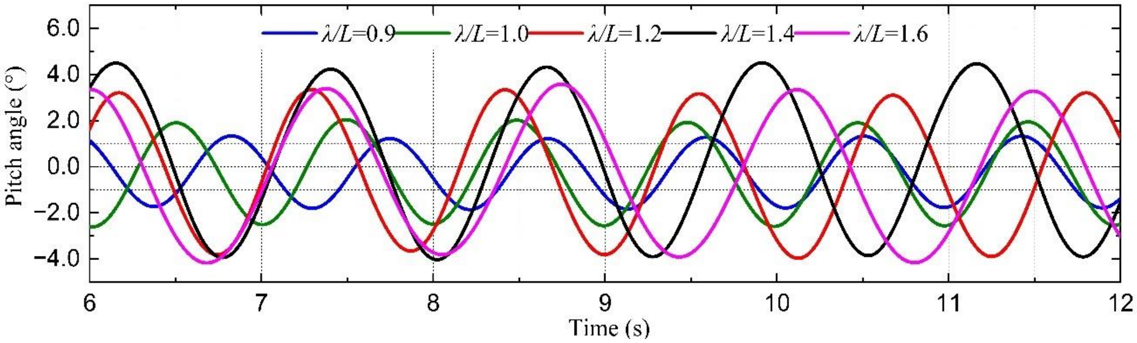

Figure 6.15: The time series of ship pitch motions at different wavelengths.

The heave and pitch motions are further calculated as response amplitude operators (RAOs) and plotted against the non-dimensional parameter of wave/ship length ratio λ/L in Fig. 6.16 and 6.17. To validate the numerical results, these RAOs are compared among different methods, including the numerical CFD-FEA models by Jiao et al. (2021) and Lakshmynarayanana et al. (2020), as well as experiments of Chen et al. (2001).

Figure 6.16 shows that the heave RAOs from the present CFD-DMB method generally show good agreement with the experiments by Chen et al. (2001) at short waves; however, the peak value at ship-wave matching resonance is captured at $\lambda/L = 1.4$ rather than $\lambda/L = 1.2$ as in the experiments. The correspondence between the present model and the CFD-FEA model is favourable in heave predictions except in the non-dimensional frequency range of $1.4 - 1.6$, where the magnitude of heave is over-predicted by about 25%. Such numerical error may cause by different numerical framework, structure models and mesh errors.

Figure 6.17 presents the pitch RAOs of the present method and the CFD-FEA model by Jiao et al. (2021), which produces small differences in the high-frequency region; however, there is an over-estimation in long waves by an average about 8.6%. Some differences in the pitch RAOs can be noted between the present model and the CFD-FEA model by Lakshmynarayanana et al. (2020) in long waves, especially with a peak difference at $\lambda/L = 1.5$ of approximately 15%. All numerical models overestimate the trim angle at long waves by about 25% compared with the experiments.

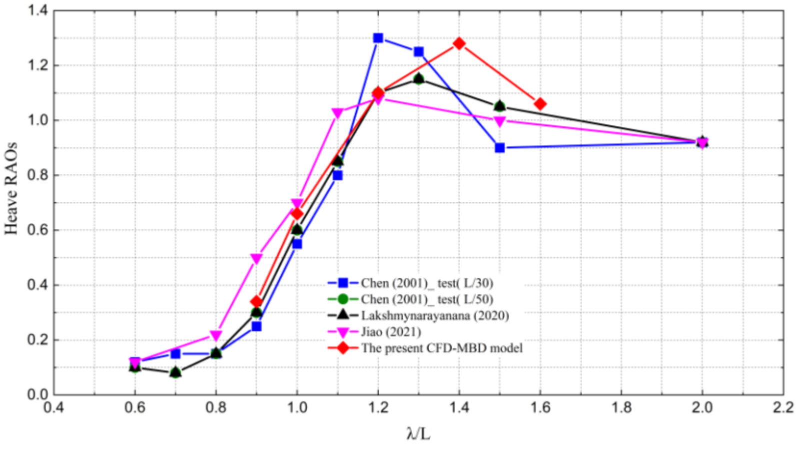

Figure 6.16: Non-dimensional heave RAOs calculated from the CFD-DMB method compared with co-simulation and experimental measurements.

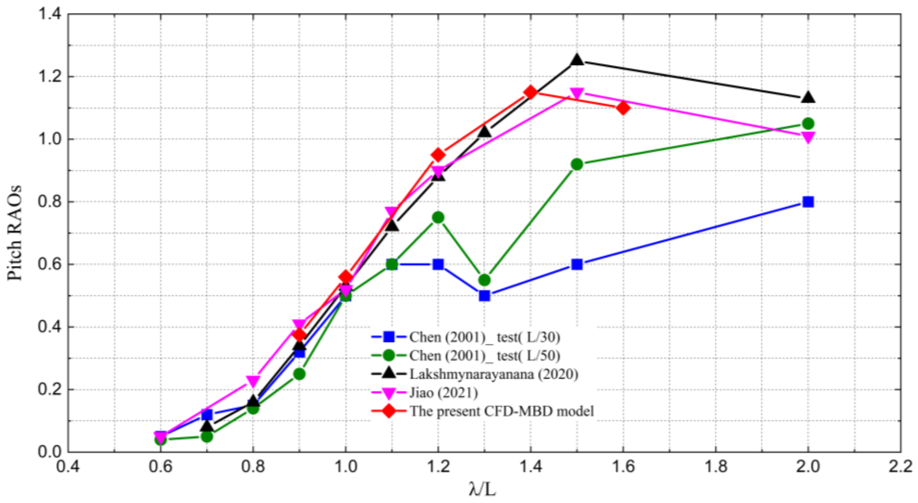

Figure 6.17: Non-dimensional pitch RAOs calculated from the CFD-DMB method compared with co-simulation and experimental measurements.

6.3.1.2 Regular Wave-induced Vertical Bending Moments

The longitudinal distributions of the total VBMs at each ship section estimated by the present CFD-DMB method are given in Fig. 6.18 for different wavelengths. The VBM values are non-dimensionalised by $M/\rho g L^2 B \xi$, where ξ is the monitored wave amplitude. As can be seen from the results, the distributed VBMs show similar trends for different wavelength cases, and the peak crest and trough VBM values are found at the wave-resonance condition ($\lambda/L = 1.2$), which implies most enormous bending moments occur at the wave-resonance condition. Both hogging and sagging VBMs show strong asymmetry behaviour along the ship longitudinal, the peak sagging VBM occurs at ship section 10, and the peak hogging VBM occurs close to ship section 12.

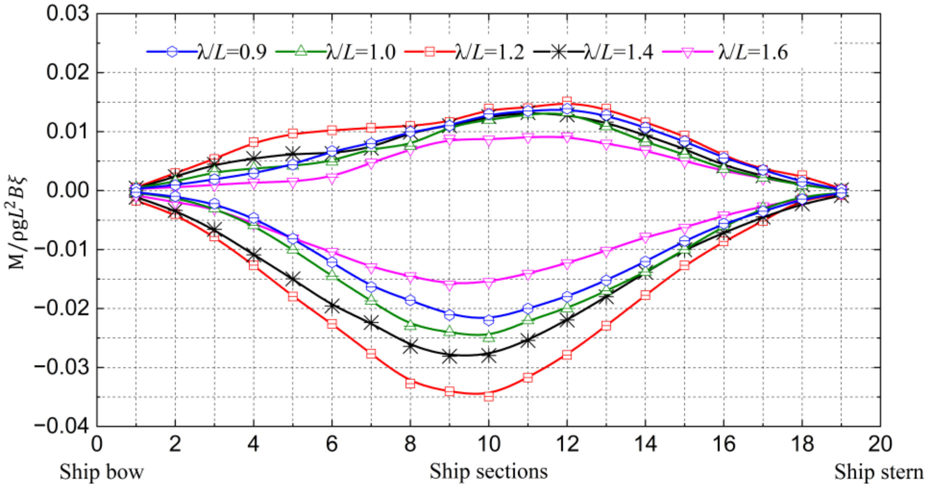

Figure 6.18: The distributed of VBMS amidship at different wave lengths.

The distributed VBMs at resonance condition (λ/L=1.2) are selected as a representative case to further compare with the numerical CFD-FEA results from (Jiao et al. 2021), as shown in Fig. 6.19. The results revealed that the VBMs predicted from the present method show a similar trend to the results from the CFD-FEA method, especially the excellent agreement of the total sagging moments. However, the peak crest value of the hogging VBMs is detected at ship section 12 in the CFD-DMB method, rather than at ship section 11 in the CFD-FEA method.

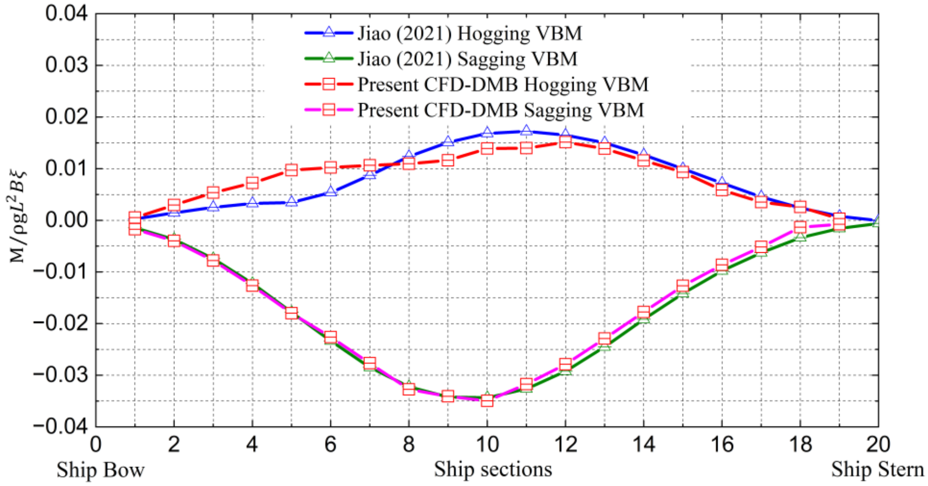

Figure 6.19: Comparison of the distributed VBMs at each ship section obtained by using the CFD–FEA method with those from Jiao et al. (2021). Adapted with permission from (Jiao et al. 2021).

The VBM RAOS at ship amidship is further compared among different numerical methods and experimental measurements. As shown in Fig. 6.20, there is an underestimation of the results from the present CFD-FEA model at some wave conditions, i.e., $\lambda/L = 1.0, 1.4$ by a maximum of about 15%, compared to the results from Lakshmynarayanana et al. (2020). These deficiencies may be caused by the implementation of a structural damping ratio, i.e., 0 in the CFD-FEA model and 0.01 in the CFD-DMB model. The damping effects on structural loads were studied by Lakshmynarayanana et al. (2020), which pointed out that the increase of structural damping from 0 to 0.01 may reduce the bending loads by about 25%. However, in the present study, applying the structural damping to stabilize the structural solver and represent the material’s real damping behaviours is necessary. Overall, the results give a fair depiction of structural loads of the flexible ship to different wavelengths, enabling a further facile step for the focused wave study.

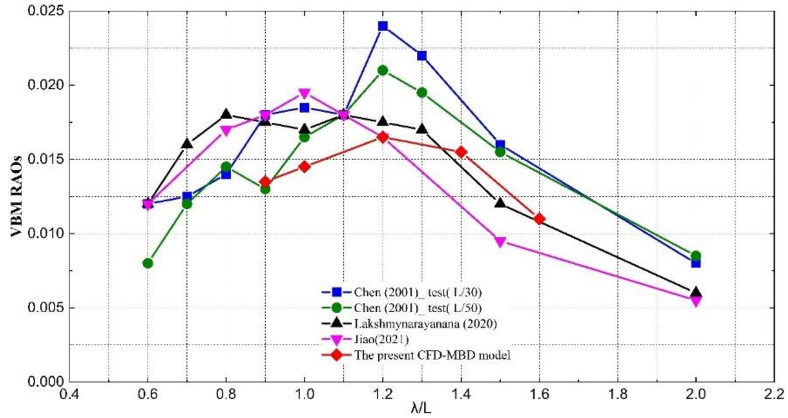

Figure 6.20: Non-dimenstional VBM RAOs admidsip calculated from CFD-DMB method compared among numerical and experimental measurements.

6.3.1.3 Green Water Visualization of flexible ship in regular waves

To better understand the green water phenomenon under different wave conditions, the physical views of the violated free-surface flow during slamming events at λ/L=0.9 and λ/L=1.2 are shown in Fig. 6.21 and 6.22, respectively. Both figures include two phases of the ship motion state with four time steps within one wave cycle, from ¼ T to T. A severe slamming and green water on deck can be observed when the ship is sailing in λ/L=1.2, however, such events are not noticeable at λ/L=0.9 because the vertical motion of the ship is relatively low.

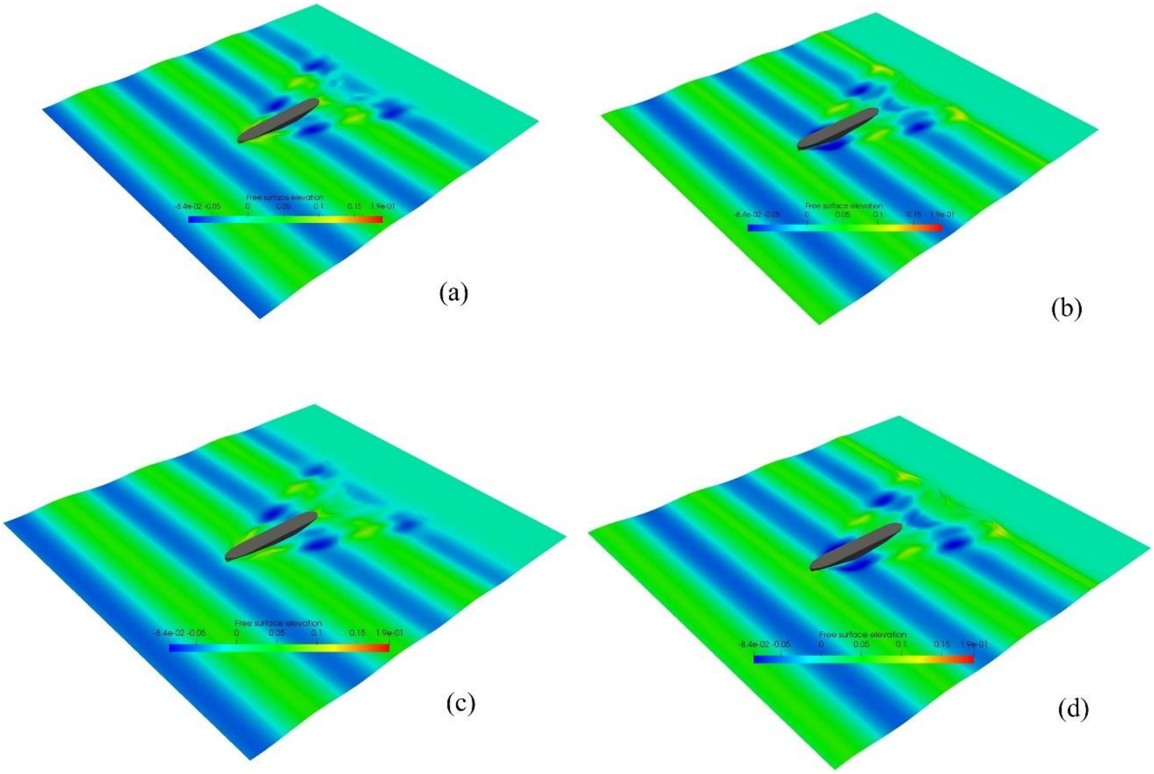

Figure 6.21: The green water phenomenon captured at one wave cycle in heading wave conditions with wave height H=0.12m, wavelength (λ/L=0.9): (a) ¼ T, (b) ½ T, (c) ¾ T, (d) T.

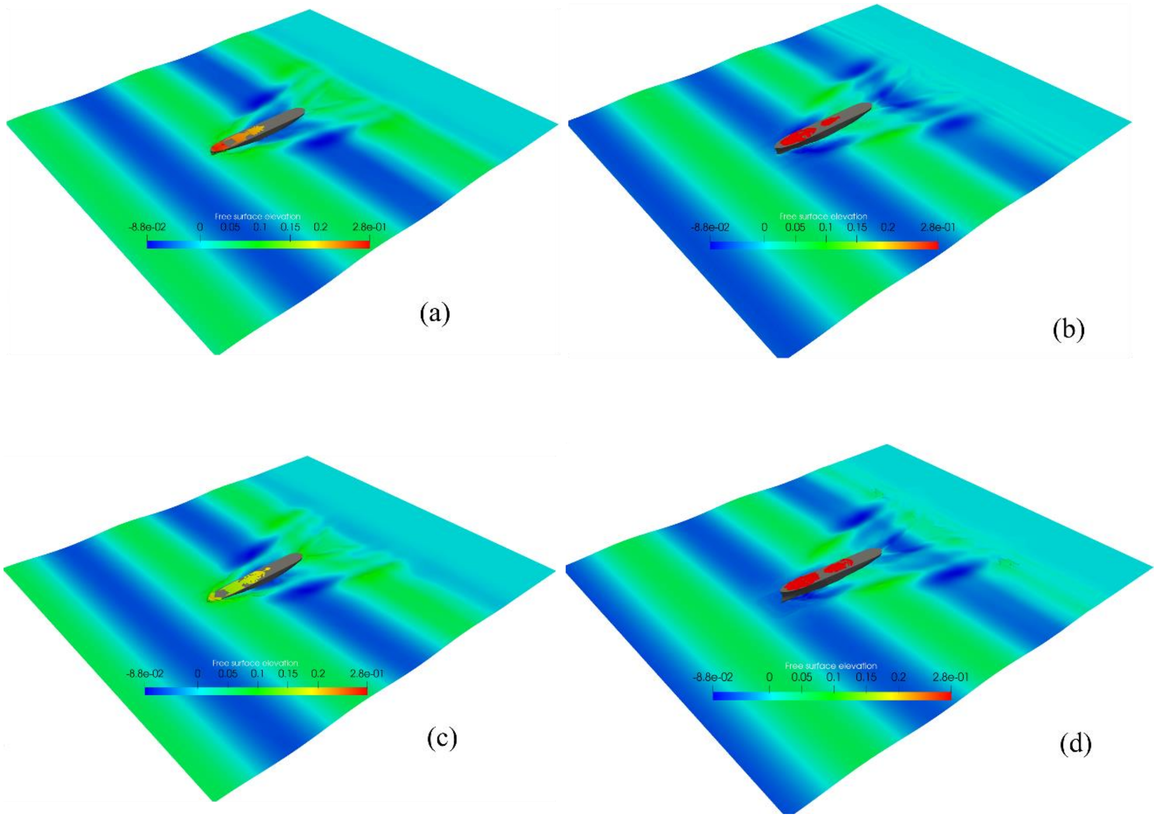

Figure 6.22: The green water phenomenon captured at one wave cycle in heading wave conditions with wave height $H=0.12$ m, wavelength (λ/L=1.2): (a) ¼ T, (b) ½ T, (c) ¾ T, (d) T.

6.3.2 Comparison of ship motions and impact wave loads in focused and regular waves

In this chapter, the wave elevations, global ship motions and impact wave loads of the S175 model in regular waves and focused wave groups are presented in a comparative manner. In order to control the variables, the wave parameters, including significant wave height and trough-to-trough period of the focused and regular waves are set as identical. Moreover, to better understand the slamming impacts and green water on deck at extreme wave conditions, the flow field around the ship is visualised with the impact pressure predictions.

Figure 6.23 compares the time-series free surface elevations of the focused wave group and regular waves ($\lambda/L = 1.6$) for the same significant wave height ($H_s = 0.12$m), trough-to-trough period ($T_p = 1.4$s) and uniform current speed of $U = 1.80\text{m/s}$. The focal location were predefined at the ship's LCG and the focal time was set to be 15s. These values were determined by considering the computational cost and arranging a sufficient time for wave propagations. The time records of 11.5s to 19.5s duration of the wave propagation were presented for comparison.

As the wave elevations are shown in Fig. 6.23, the focused wave shows good agreement with the theoretical theory; however, a slight front shift of the focal time can be observed. The trough-to-trough period of the simulated focused wave group and regular wave is almost similar. As can be seen from the figure, the focused wave group tends to superimpose a higher wave elevation at the focal time, raising the wave elevation by about 25% from 0.061m (regular wave) to 0.083m. It is known that the increased wave elevation contains higher energy, which implies that forces due to focused waves are expected to be larger than that in the regular wave condition. The enlarged fluid forces further violate the ship response and corresponding elastic behaviour, which will be in the following sections.

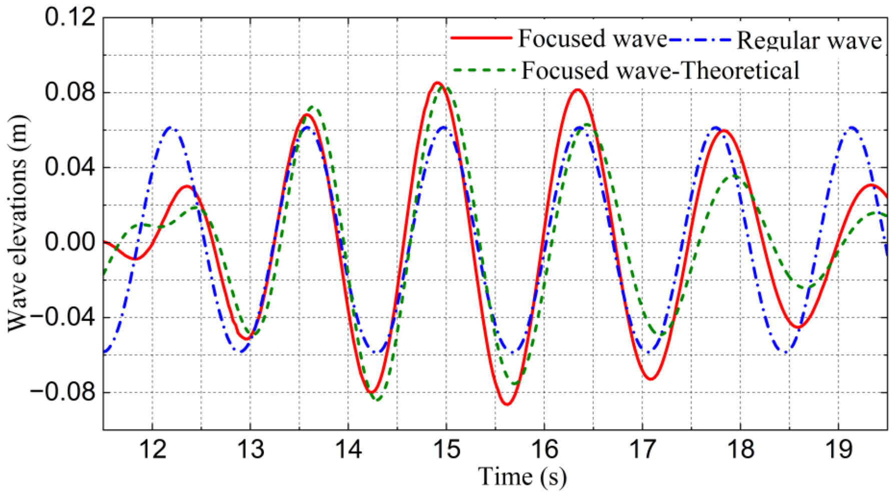

Figure 6.23: Comparison of the free surface elevations between the simulated/theoretical focused wave group and regular waves.

6.3.2.2 Flexible ship motions

The time histories of the heave motions induced by the focused wave are compared with that of the regular wave ($\lambda/L = 1.6$) as shown in Fig. 6.24. As can be seen from the figure, the ship in focused wave induced a significant motion response of the value of 0.095m at $t = 17.5$s, which increases the heave amplitude by about 25% compared with that in the regular wave. After the focal time, the heave motion decays progressively. The asymmetric behaviour can be noticed in heave signals, in which the trough of heave motion is generally much greater than the crest value, as the ship experienced obvious sinkage due to the forward speed and dynamic effects.

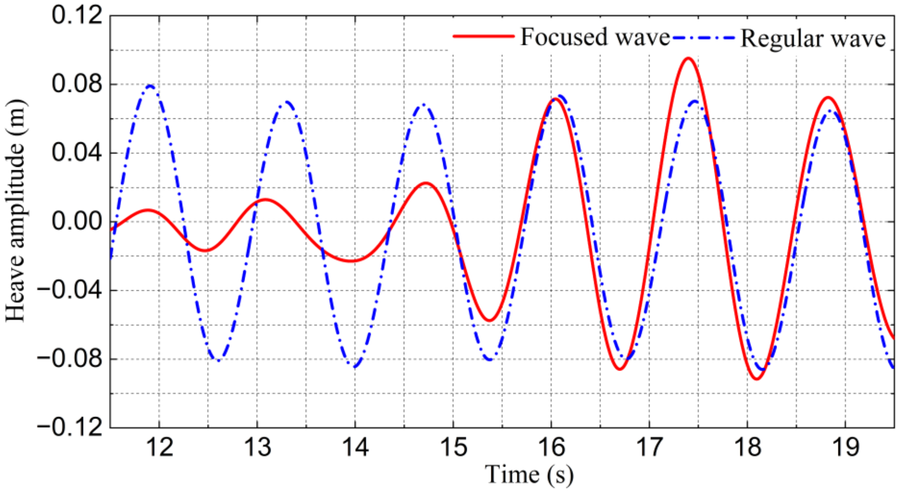

Figure 6.24: Comparison of the flexible heave motion between the focused wave group and the regular waves.

Figure 6.25 shows a comparison of the time series of the pitch motions between the focused and regular wave conditions. The pitch motion in the focused wave group shows a similar trend as the heave motion but with a phase shift, which reaches its peak after the focal time and decays progressively. As can be seen, the pitch amplitude increases by about 20% at the physical time of 18s compared to that in the regular waves. The enlarged trim may result in severe whipping effects, which may endanger hull girder integrity.

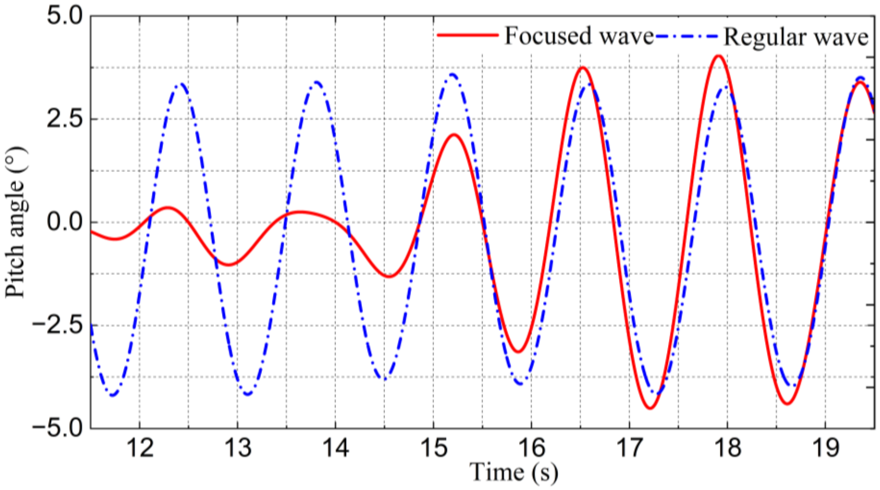

Figure 6.25: Comparison of the flexible pitch motion between the focused wave group and the regular waves.

6.3.2.2 Focused Wave-induced Vertical Bending Moments

The time histories of the total VBM at the ship amidship in the focused wave are compared to those in the regular waves ($\lambda/L = 1.6$), as shown in Fig. 6.26. The sagging moment reaches its lowest value at the time instant of 16.5s, with an increase of about 25% compared to that in the regular waves. The total VBM signal is further filtered using a low/high pass filter to extract the wave-induced VBM (green dot) and high-frequency VBM (pink dash-dot). It can be seen from the figure that the high-frequency components were more pronounced between 16s to 18s, which is right after the focal time, accounting for about 20% of the total VBMs. The high-frequency components are mainly attributed to the nonlinear components in the focused wave group and structures.

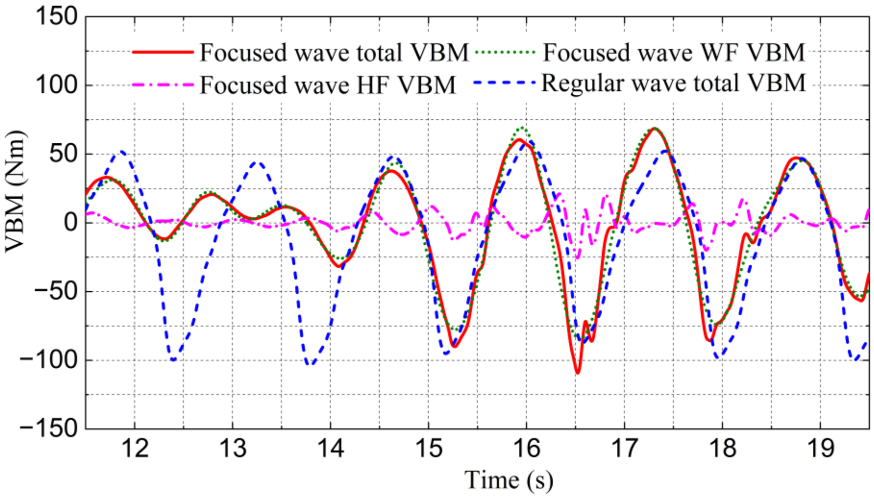

Figure 6.26: Comparison between the flexible ship VBM amidship in regular wave and focused wave group.

To better assess the VBMs of each section along the ship length, the longitudinal distribution of VBMs of focused wave and regular wave are displayed in Fig. 6.27. It is seen that the sagging VBM is generally much larger than the hogging VBM for both cases. The largest sagging VBM appears at section 10 in front of the largest hogging VBM due to the contribution of nonlinear whipping loads components, which is evidenced by Jiao et al. (2021). There is a noticeable increase by about 9.8% of sagging moments at section 10 in the focused wave compared to that in the regular waves. The largest hogging moment is shifted from ship section 12 (regular wave) to ship section 11 (focused wave).

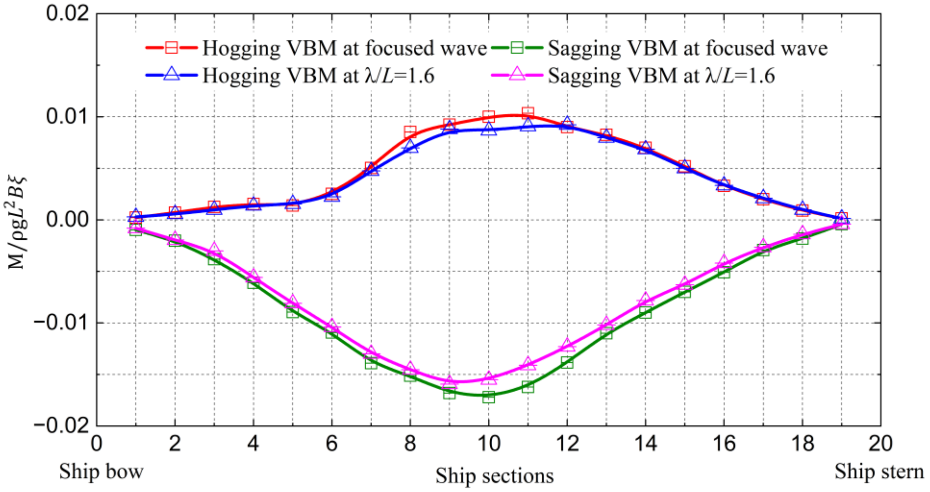

Figure 6.27: Longitudinal distribution of VBM along the ship length for regular waves and focused wave groups.

6.3.2.3 Slamming Loads and Green Water on Deck

In this chapter, the slamming loads and green water on deck phenomenon are analysed between regular and focused wave conditions. It should be noted that the time series of impact pressure data have a sampling frequency of about 667Hz associated with the selected time step of 0.0015s, which may not be sufficiently small to capture the instantaneous impact peak (Jiao et al. 2021); however, this sampling frequency is determined as a compromise between accuracy and the computational costs.

The time series of the impact pressure at front bow measurement points P1–3 are compared between the regular and focused wave as plotted in Fig. 6.28. The measurement points P1, P2 and P3, located at the centre line at the ship bow, capture the slamming impact loads and bow entry water pressure. The figure shows that the pressure signal at P1 generally has the sharpest peak due to its relatively small dead-rise angle compared with P2 and P3. However, the pressure signals contain high-frequency noises, which may be related to the ship ringing phenomenon. This part of the analysis will be carried out for future studies. The slamming pressure becomes higher and sharper in the focused wave at 15s to 17s compared to the regular waves, which indicates the ship experienced a severe slamming phenomenon.

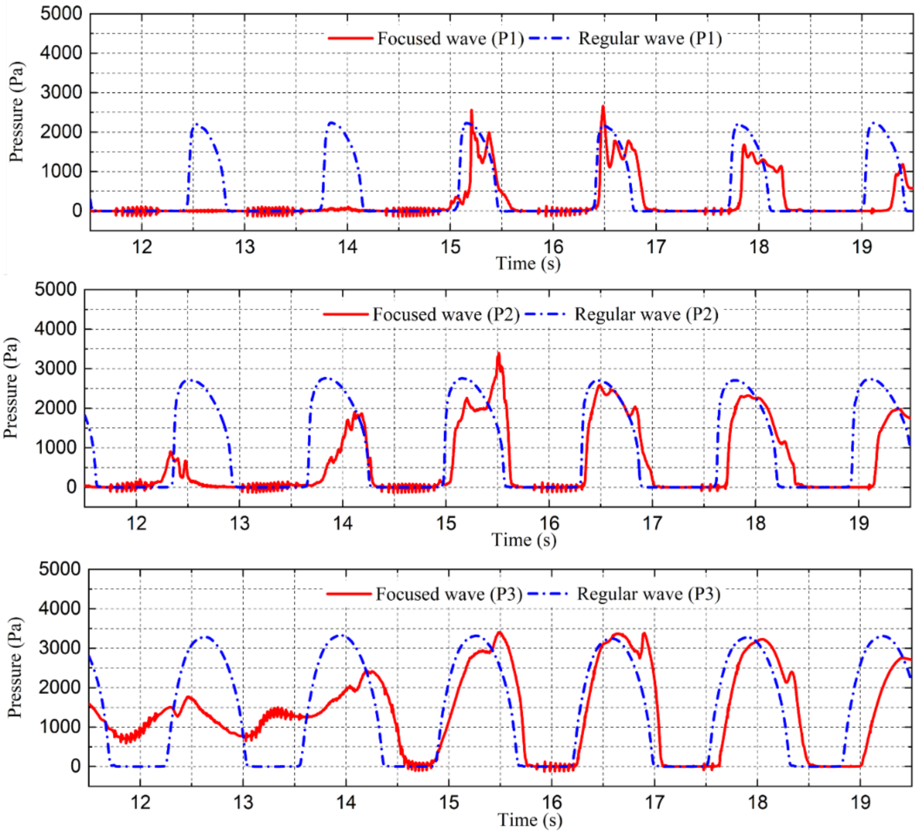

Figure 6.28: Comparison of the bow slamming pressure between the focused wave and regular wave with wave height 0.12 m, pressures probes located at P1, P2, P3.

The bow bottom gauges at P4, P7 and P9 are immersed in the water, which the hydrostatic pressure dominates. The pressure signals show general regular shapes with the occurrence frequency of slamming event equal to the wave encounter frequency (see Fig. 6.29). The peak values of the slamming pressure are found at the bow flare region (P4), and then the pressure decreases from the bow front to the backward. The magnitude of the peak slamming loads show favourable agreement with the co-simulation results from Jiao et al. (2021). As shown in Fig. 6.29, the impact loads in the focused wave are generally larger than those in the regular waves among these gauges, with an increase up to 9% of slamming pressure at the bow flare.

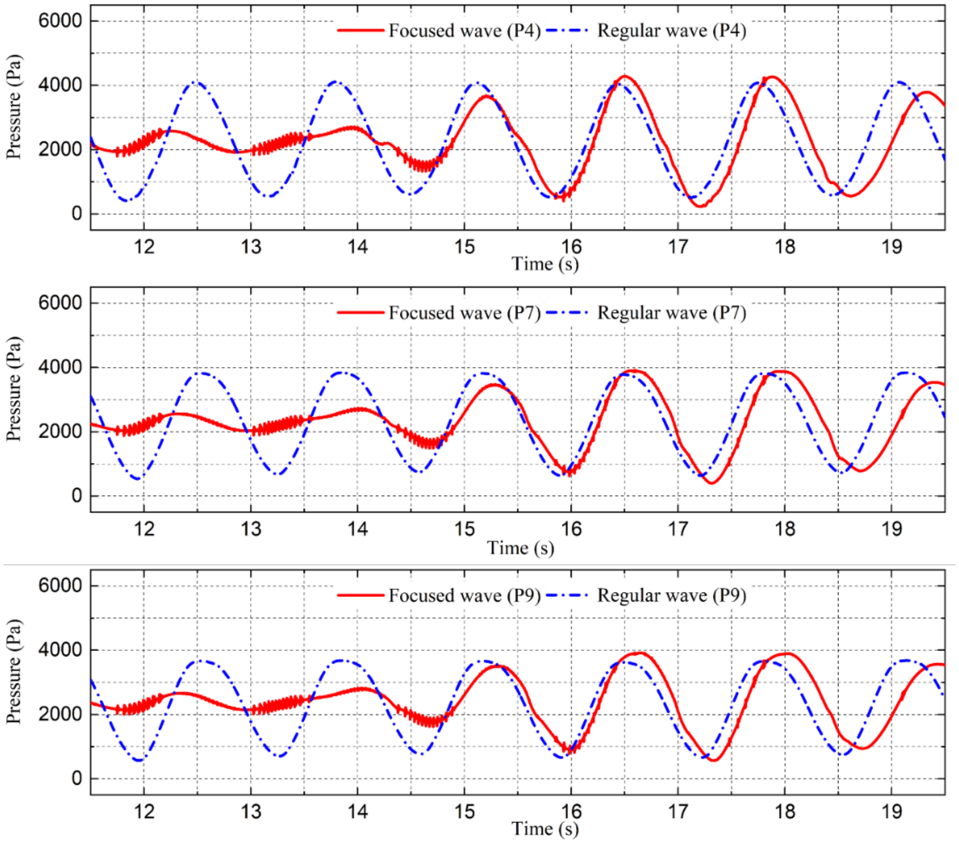

Figure 6.29: Comparison of the bow slamming pressure between the focused wave and regular wave with wave height 0.12 m, pressures probes located at P4, P7, P9.

Visual observation of slamming events obtained from the CFD analysis at a wave cycle ($t = 17s - 18s$) of the ship in regular and focused wave conditions are shown in Fig. 6.30. The pronounced slamming and severe wave overtopping phenomenon are captured well in the focused wave due to the severe ship responses, whereas they do not appear under regular wave conditions.

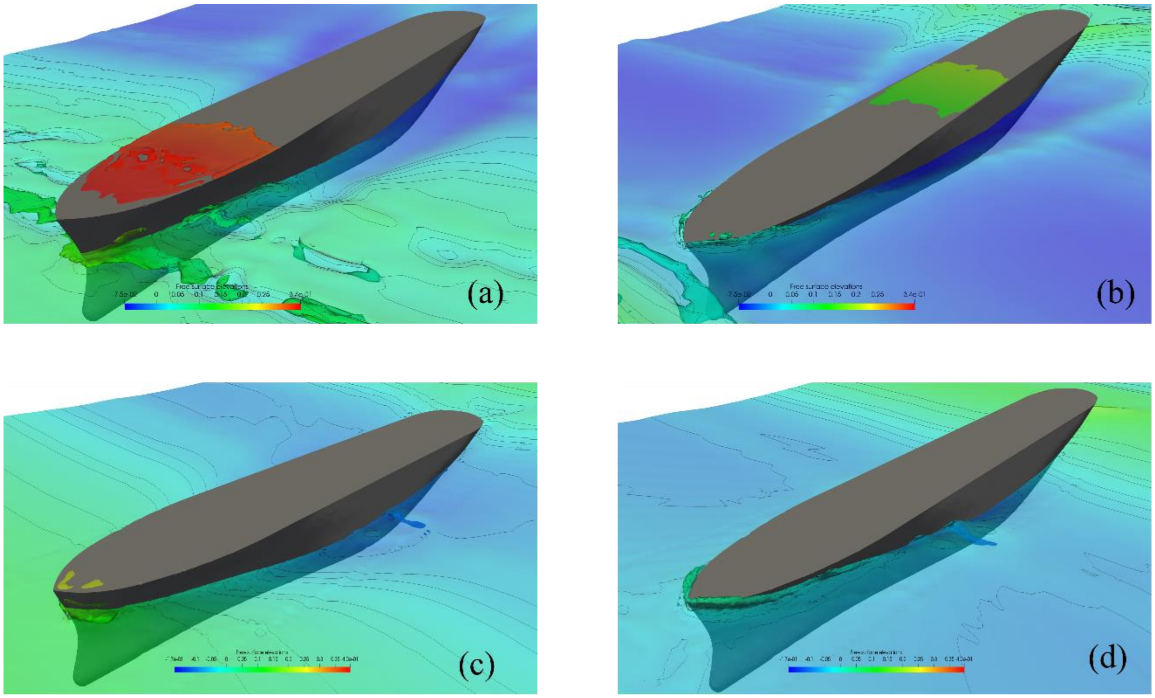

Figure 6.30: Comparison of the green water on deck phenomenon between the focused wave and regular wave: (a) Bow up in focused wave, (b) Bow down in focused wave, (c) Bow up in regular wave, (d) Bow down in regular wave.

6.4 Concluding Remarks

This paper adopts an efficient two-way FSI model coupled with an OpenFOAM solver and MBDyn to investigate the ship hydroelasticity of an S175 containership in regular and focused wave conditions with forward speeds. A series of validation and verification studies were presented to evidence that the present CFD-DMB method can accurately measure the ship responses and the peak VBM loads in waves, which is of prime importance to access ship hydrodynamic and hydroelasticity problems. This well-validated FSI framework is capable of extending its applications for various types of ships at any length. However, a dedicated beam frame needs to be designed for multihull marine structures, e.g., catamaran and trimaran, in reference to Lavroff et al. (2013). The present method can be further extended to study asymmetrical ship motions, e.g., coupled torsional and bending behaviour of a ship operating in oblique waves. The limitations should be illustrated here: The Euler–Bernoulli beam is not applicable for modelling large open-section bulk carriers or similar cases with ships experiencing huge torsional effects. To do so would require a full three-dimension structural model or a high-order beam, e.g., Vlassov beam.

Determining the extreme values of ship responses in irregular waves through FSI simulation based on Navier–Stokes equations is almost impossible. Here, the focused wave theory is used to represent expected maximum responses from the JONSWAP sea spectrum, i.e., wave events tailored to generate this response. A critical attribute presented by this paper is the comparison of the numerical results, including the ship global motions, ultimate structural strength, slamming and green water loads between focused and regular wave conditions. These data give hints of the significant influence of focused waves on the ship structures, which found that the heave and pitch amplitudes rise by about 15–20% compared to those in regular waves. The VBMs are extracted from the beam profile in the structure solver and compared between the focused and regular wave with time-history data in Chapter 6.3.1. These results show that the focused waves have a maximum increase of 8.5% and 9.8% of total hogging and sagging VBMs, respectively, compared to regular waves. The high-frequency components are contained in total VBM signals, which are attributed to the nonlinearity of the response and wave process. In addition, the significant nonlinearities of the response are found as hogging/sagging asymmetry and vibrations from slamming impacts. The slamming impacts between focused waves and regular waves are compared in Chapter 6.3.2. The impact pressure signals in focused waves generally show larger and sharper shapes than in regular waves. Moreover, the physical observations of the ship sailing in focused waves clearly show that severe bow slamming and green water on deck occurred; however, it is not noticeable in the regular wave condition.

The main conclusions obtained are:

1.Taking the S175 containership as an example, the accuracy of this integrated CFD-DMB modelling tool was demonstrated for the predictions of dynamic ship motions and slamming wave loads with the hydroelastic effects within a range of wave frequencies. A comprehensive comparison between the present method against the CFD–FEA method and the experimental results show that the CFD–DMB method accurately measures the peak VBM loads, which is persistent in the problems associated with ship hydroelasticity.

2.The focused wave group was generated based on the modified “NewWave” theory, considering the current effects. The simulated wave elevations were found in favourable agreement with the theory.

3.The extreme ship motions and hydroelastic responses of the S175 containership were further studied in a focused wave condition to investigate the extreme sea conditions that a ship may experience in a real sea state. Numerical results demonstrated that the flexible ship would experience larger ship motions, vertical bending moments and slamming loads in focused waves than in regular waves, in which case, the design of the hull girder should leave enough of a margin to resist the high loads expected in real sea operations. The future work will present an experimental study on the flexible ship in focused wave conditions.

7 A Hydroelasticity Analysis of a Damaged Ship Based on a two-way Coupled CFD-DMB Method

Nowadays, safety is the top priority in the shipping industry. Despite many efforts to improve ship design in recent years, accidents caused by collisions and groundings continue to occur.

Hull damage openings frequently occur during collisions or ship contacts, allowing seawater to flood into the damaged tank and hit the inner tank wall. This can cause sloshing, a phenomenon that poses a serious risk to the ship's stability and may even lead to capsizing (Manderbacka et al. 2019). This mechanism becomes even more complicated when the ship sails in waves, as the flooding water inside the tank can reduce the ship's wet natural frequency towards the wave-structure resonance frequency range. A slight motion can trigger violent sloshing when the excitation frequency matches the natural frequency of the wave components (Gao et al. 2015). In such conditions, predicting the ship's seakeeping behaviour and hydrodynamic loads can be difficult due to the nonlinear interaction between the intake and outer water of the damaged compartment.

This study establishes a novel Fluid-Structure Interaction (FSI) model, which fills the gap left by the majority of numerical models on damaged ship studies in the open literature that assumes the ship is a rigid body and do not consider hydroelastic loads on the hull girder for a damaged ship. In this study’s proposed FSI framework, a two-way CFD-DMB method was applied, where the intake flooding water pressure and hydrodynamic loads exported from the CFD calculations were used to derive the structural responses in the DMB solver, and the structural deformations were fed back into the CFD solver to deform the mesh. To communicate data between the CFD and multibody solver, a two-way coupling algorithm was implemented to transfer the fluid loads and structural deformations effectively. The previous study (Wei et al. 2022) evaluated the performance and accuracy of the coupling solvers on an elastic-demonstrated containership in regular and focused wave conditions. This paper extends the authors’ previous studies by investigating the seakeeping and hydroelastic behaviour of the S175 containership in both intact and damaged conditions with considerations of the dynamics of flooding water, motion effects and the elastic ship deformations.

The number of damaged compartments and positions were studied based on the proposed FSI model to investigate the effect on flexible ship seakeeping and hydroelastic behaviour. This will help to gain more insight into the understanding of the dynamic damaged ship behaviour in waves, including the interactions between the flexible ship and flooding water, the violent free surface phenomena (e.g., sloshing) and longitudinal structural load distributions. This study will be valuable in better assessing the damaged ship behaviours and the wave-induced global and local loads with the consideration of ship hydroelasticity, which assists in rapid decision-making relevant to post-damaged evacuation and maintenance. The results of this paper will also shed some light on improving the current legislation on the safety of ships in damaged condition by the international SOLAS (Safety of Life at Sea) convention.

The rest of this chapter is organised as follows: in Chapter 7.1, the numerical methodologies, the detailed problem statements and the model testing set-up are discussed. In Chapter 7.2, the verification and validation studies are presented. In Chapter 7.3, the numerical results of the study on the dynamic motions of the flexible ship in intact and two damaged scenarios are illustrated. A series of numerical results, including dynamic flooding water, flexible ship motions and structural loads are also analysed. Virtual observations of the free surface elevations inside the damaged tank are shown accordingly. The conclusions and future recommendations are drawn in Chapter 7.3.3.

7.1 Model Description

7.1.1 Intact and damaged ship

This study used the standard S175 containership with a 1:40 scale ratio as a case study for both intact and damaged conditions. The ship model did not include any appendages. The longitudinal body shape of the intact ship model is shown in Figure 7.1.

Since ship damage may occur in many ways, this study only focused on the side damage type of hull openings where the ship may experience a collision with ice or other marine structures. The damaged parameters (e.g., damaged tank numbers and locations) were generally random quantities that may be described by the probability distribution. Such probability distributions in the cases of collision damages were regulated by the International Maritime Organization (IMO 2003). The numerical model developed by Parunov et al. (2015) defined credible damaged scenarios based on Monte Carlo (MC) simulation according to IMO probabilistic models. In his model, a set of 1000 random samples were drawn according to the IMO recorded accidental models. The results showed that in the cases of collision damage, the probability of single-tank damage or double-tank damage is the highest, followed by three tanks damage which comes second. Based on these considerations, plausible damage scenarios were defined for the purpose of the present study. For the damage of collision case studies, damaged tanks at the ship starboard were assumed in this study, resulting in asymmetrical damage, as shown in Figure 7.1(a, b). The damage at the amidship (ship section 10) was shown as a representative image in Figure *2.5* 7.1(c) where the damaged opening in this scenario has a uniform rectangular shape of 0.22m x 0.11m on the starboard side, accounting for

5% of the total ship's length and 22% of the ship depth. Each damaged compartment had a ventilation hole to minimise the effects of spurious entrapment of air between the intake water and the inner hull. The main particulars of the intact and damaged ship models are summarised in Table 7.1.

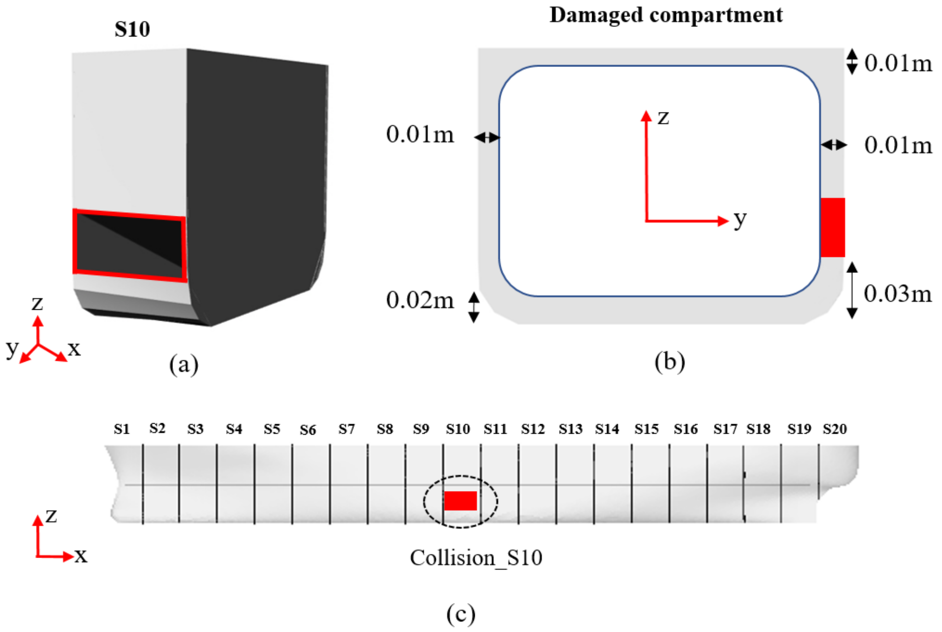

Figure 7.1: Damaged tank specifications.

Table 7.1: Principal particulars of the intact and damaged S175 containership.

Main particular	symbol	Full scale	Model
Scale	C	1:1	1:40
Length between perpendiculars	L(m)	175	4.375
Breath	B(m)	25.4	0.635
Depth	D(m)	19.5	0.488
Draft	T(m)	9.5	0.238
Displacement	Δ(kg)	23,711	370
Block coefficient (C_b)	C_b	0.562	0.562
Longitudinal centre of gravity (LCG) from aft perpendicular (AP)	x_g(m)	84.98	2.125
Vertical centre of gravity (KG) from base line	z_g(m)	8.5	0.213
Transverse radius of gyration	k_{xx}(m)	9.652	0.241
Longitudinal radius of gyrations	k_{yy}(m)	42.073	1.052

Damage opening area	$S_d(\mathrm{m}^2)$	0.952	0.0238
Damage opening length	$L_{Dl}(\mathrm{m})$	8.8	0.22
Damage opening height	$L_{Dh}(\mathrm{m})$	4.32	0.108
Damage opening compartment (S10) from FP	$L_{S10}(\mathrm{m})$	81.8	2.045

The positions of all pressure gauges are depicted in Figure 7.2. An array of 4 pressure gauges (P0-P3) were placed on the bow flare and bow bottom areas of the ship to investigate the wave-induced impact pressure of the ship during the water enter of bow.

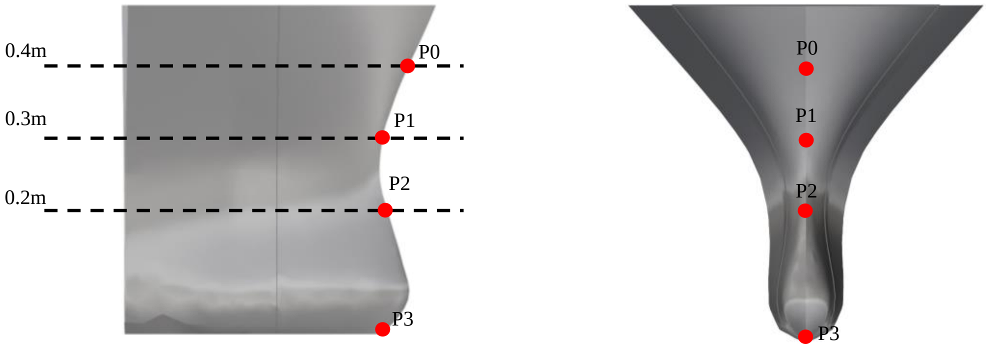

(a) (b)

Figure 7.2: An overview of the pressure gauge placements on the ship bow section: (a) ship starboard, (b) ship front view.

7.1.2 CFD model

The computational domain was established in the CFD computations to simulate ship sailing in head waves. The domain was extended in three dimensions, i.e., $-1.75L < x < 2.5L$, $-1.2L < y < 1.2L$ and $-1.5L < z < 0.5L$, where L refers to the ship length between perpendiculars. A general view of the wave domain (for the ratio of the wavelength to the ship length of $\lambda/L = 1.2$) is shown in Figure 7.3. The three-dimensional ship model was applied, but only the centre line plane of the ship was shown in the figure. It can be seen that the aside boundaries were placed far away from the shipboard sides to reduce the influence of wave reflection from numerical boundaries. Inside the numerical domain, the global Cartesian coordinate system was set at the same height level with the calm water surface, coinciding with the aft-perpendicular and the ship's centreline. The global reference frame with the positive directions of the x, y, z pointed to the ship stern, port side and the domain atmosphere, respectively. Damage was modelled in a way that damaged tanks are flooded up to the still water level corresponding to the ship's initial draft in case of significant transient responses caused by the sudden influx of flooding water.

The boundary conditions applied to the numerical wave tank are summarised in Table 7.2. At the inlet boundary, the wave velocity was prescribed for the superposition of wave and current speeds, while the pressure was set as fixed flux pressure that adjusts the pressure gradient. At the outlet boundary, the inlet-outlet boundary provided a zero-gradient outflow condition to remain the flux inside the domain. The domain bottom was set as type of wall to model deep-water seabed.

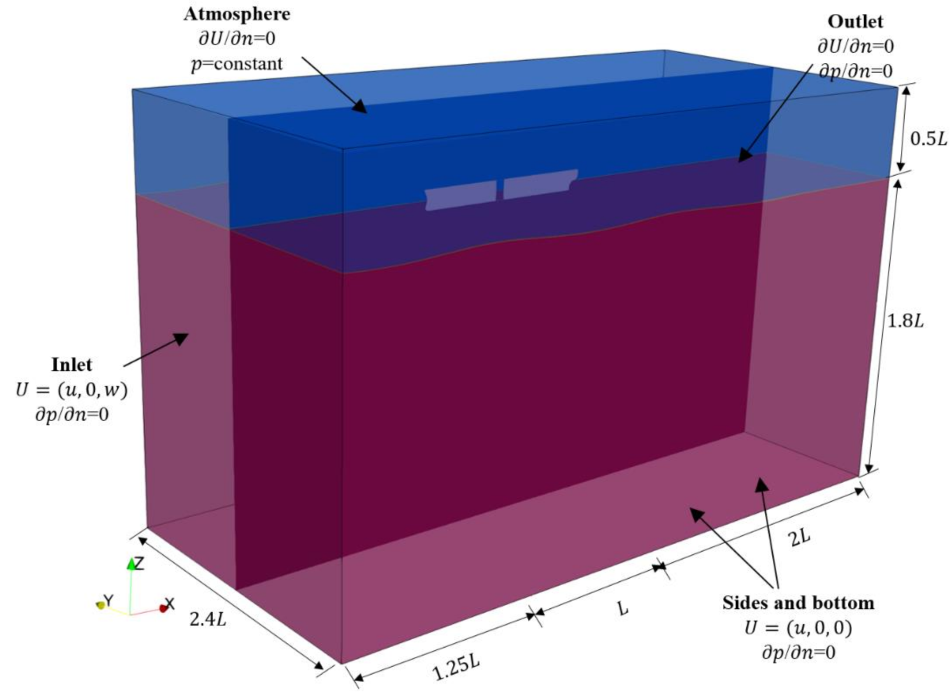

Figure 7.3: Computational domain and boundary conditions.

Table 7.2: Summary of the boundary conditions in OpenFOAM.

	Inlet	Outlet	Atmosphere	Hull
U	WV	OPMV	PIOV	MWV
P_rgh	FFP	ZG	TP	FFP
alpha.water	FV	VHFR	IO	ZG
K	FV	IO	IO	kqRWF
Nut	FV	ZG	ZG	nutkRWF
Omega	FV	IO	IO	omegaWF

where WV is wave velocity, OPMV is outlet phase mean velocity, PIOV is pressure inlet outlet velocity, MWV is moving wall velocity, FFP is fixed flux pressure, ZG is zero gradient, TP is total pressure, IO is inlet-outlet. kqRWF, nutkRWF and omegaWF are turbulence wall functions.

7.1.3 Structural model

A discrete module beam model (DMB) in conjunction with a multi-segment partitioning technique was employed in MBDyn to formulate the structural models of the selected ship model, as shown in Figure 7.4. The development of such a beam model for the intact S175 containership was explained in the authors' previous paper (Wei et al. 2022). In its numerical representation, the hull surface was divided into 20 sections, each section was served as a structural node and attached to a body element, as shown in Figure 7.4. It is seen that a series of 19 beam elements, equivalently representing the structure's stiffness, were employed to connect the neighbouring body elements. It is worth noting that the beam was restraint to have torsional and horizontal bending effects, therefore, the total-joint type (TJ) of elements were applied. A number of 39 total joints were used to connect the beginning node N1 with every other node (N2-N20, N1'-N19'), imposing constraints where the free-free beam was permitted only deformed in the vertical direction. Another set of total joint element (CJ1) was applied between the midship node (N11) and the background node (N0) to suspend the surge motion of the ship beam from the drift force. As a result, the DMB ship beam design in this study was allowed to have heave and pitch motions and experience the vertical bending effects. The detailed configuration of the DMB beam model was summarised in Table 7.3.

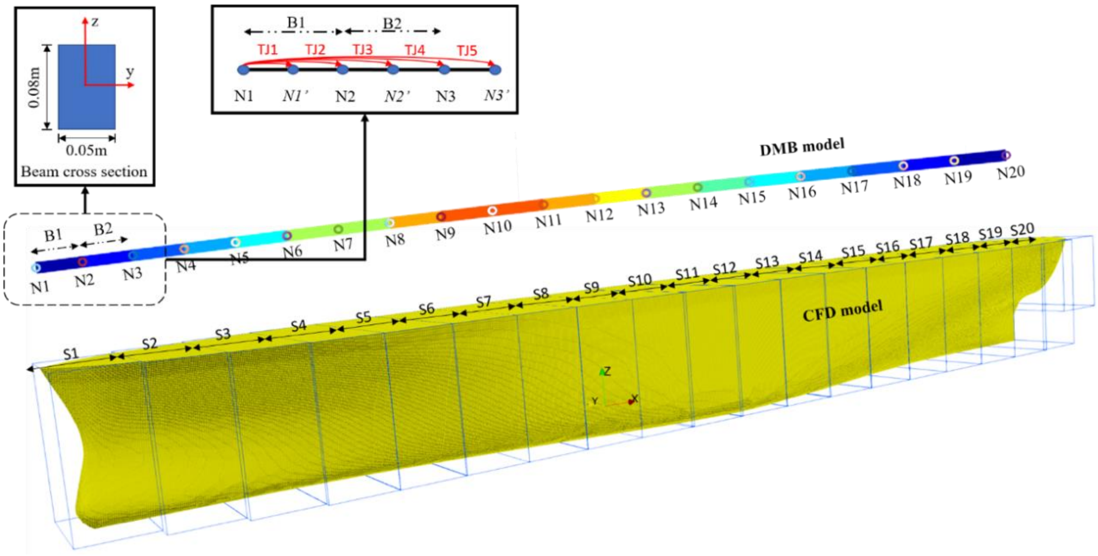

Figure 7.4: DMB ship-beam model demonstration in MBDyn.

Table 7.3: Detailed demonstration of DMB beam model.

MBDyn settings	Functions	Number
Structural nodes	Background node (N0)	1
	Beam node (N1-N20, N1’-N19’)	39
Body elements	(Body1-Body20)	20
Beam elements	(B1-B19)	19
Joint elements	Clamp joint elements (C1)	1
	Total joint elements (T1-T39)	39

As mentioned above, the DMB method provides an efficient method to define the local structure characteristics of the ship by using the equivalent beam element stiffness. To check the hull girder residual strength for damaged ships, it is important to determine the damage forms and the main parameters to characterise the damaged degree. In this study, the stiffness loss of the side-damaged containership was assessed using Zhang et al. (2021)’s method based on the calculation of the loss of section modulus and the stiffness loss of the structure. This method reduces enormous modelling efforts and computing time against other methods, e.g., the simplified progressive collapse method (Smith 1977) and nonlinear finite element analysis (FEA). The authors validated the model's applicability on 13 types of ship damage scenarios with favourable agreement compared to the results of FEM. In their approach, the stiffness loss of the hull girder with side opening type of damages (symmetric about the neutral axis) was approximately 1.28% to 1.69% of total beam stiffness. It is worth highlighting that if the ship’s double bottom loses its capacity to withstand the longitudinal stress, the hull girder residual strength will reduce significantly, i.e., 14.8% to 38.3% of the overall stiffness based on the predictions from Zhang et al. (2021). Therefore, in this study the residual strength of the hull girder was accounted by applying a 2% structure loss on the local stiffness of beam elements at the damaged tank position.

7.1.4 Modal analysis (intact ship)

The vibration behaviour of the DMB ship-beam model for an intact containership was earlier examined by (Wei et al. 2022). To give a brief summary, the eigenvalues f_b of the free-free beam up to the fourth order were estimated in dry condition using the Arpack solver in MBDyn as listed in Table 7.4. Although MBDyn does not support the wet modes analysis, the wet-mode eigenvalues of the ship-beam model have previously been investigated using a commercial FEA software Abaqus (Wei et al. 2022). It is seen from Table 7.4 that the dry-mode beam eigenvalues were shown in favourable agreement with the experimental results f_s by Jiao et al. (2021). The beam cross-section profiles, including the height and width, were modulated by matching the natural frequencies with the real ship vibration (mainly 2nd mode). The closed beam profile with a rectangular cross-section of 0.08m x 0.05m was selected and applied in this study's later cases.

It is worth pointing out that the predictions on the eigenvalues of the damaged ships pose difficulties since the load distributions of a damaged ship change in time and space due to the fluctuation of the dynamic flooding water. One possible method is to calculate the damaged ship eigenvalues in a steady state, i.e., the damaged ship floats in still water, therefore, the mass of flooding water is treated as a static lump mass.

Table 7.4: Calibrated beam natural frequency properties and error (f_b denotes MBD beam dry-mode natural frequency and f_s is the ship natural frequency from experiment) (Jiao et al. 2021).

Order	Mode	f_b (Hz)	f_s (Hz)	Error (%)
1st	2	10.140	10.154	0.112%
2nd	3	26.116	26.241	0.482%
3rd	4	49.136	49.747	1.246%

7.2 Verification and Validation

7.2.1 Sloshing tank

The first validation case was presented for a 2D sloshing problem in order to test the performance of the CFD solver in solving nonlinear free surface flow and capturing the sloshing effects. In this validation study, a two-dimensional moving tank extends into two directions, i.e., $0 < x < 0.57$ m, $0 < z < 0.3$ m. Three free surface probes (P1-P3) were placed in the middle and two sides of the domain, as shown in Figure 7.5. Two-turbulence models, $k - \omega$ SST and $k - \varepsilon$ were tested with the turbulence wall functions applied at wall tanks. The tank is moving periodically with a speed amplitude of a = 0.005m and shaking frequency w_0= 6.0578 s^{-1}, which is consistent with the experimental settings of (Liu et al. 2008). The time step size was selected to be 0.005s. The numerical model runs up to 20s with 40 cores and consume about 0.3 CPU hours. The numerical results of free surface displacement (η) obtained in all three wave probes are shown in Figure 7.6 and further compared to the experimental data of Liu et al. (2008) with a reasonably well agreement.

It can be concluded that the selected multi-phase solver is successful in solving the complex physics inside the sloshing tank and it is applicable for further damaged ship seakeeping analyses.

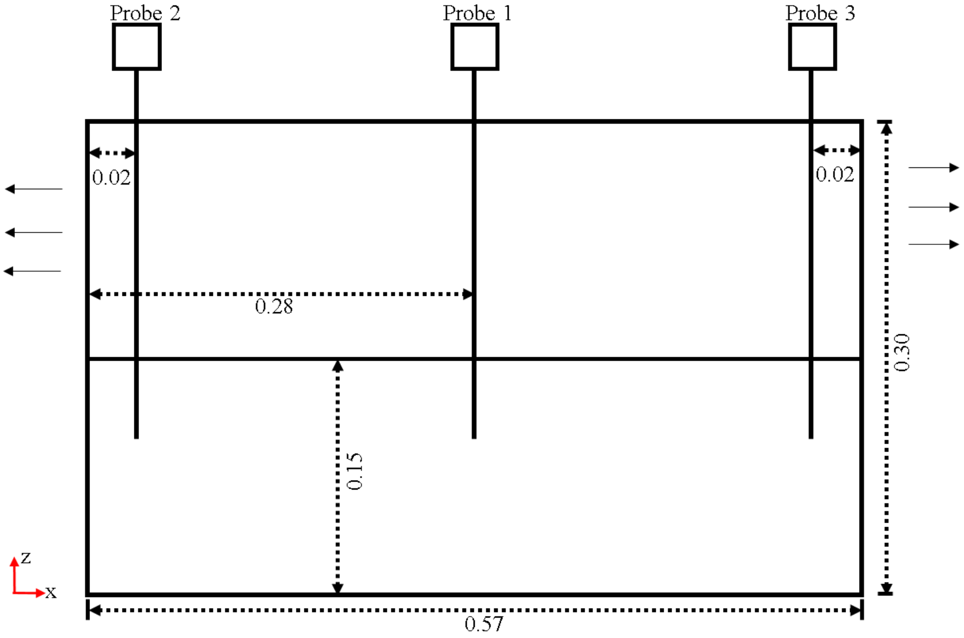

Figure 7.5: The two-dimensional (2D) sloshing tank layout.

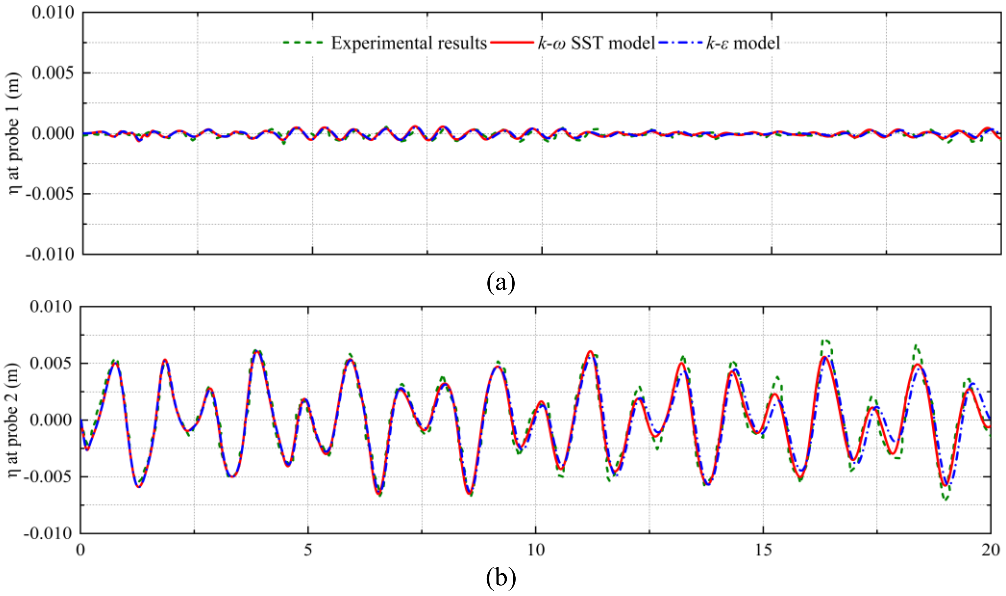

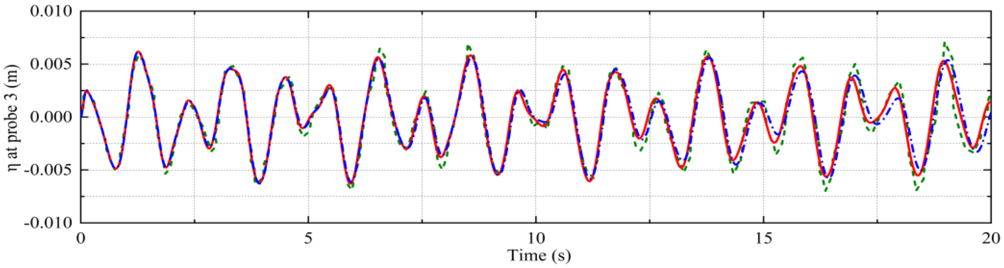

(c)

Figure 7.6: The numerical results extracted from wave probes compared to the experimental results and analytical results: (a) Wave elevation monitored at probe 1, (b) Wave elevation monitored at probe 2, (c) Wave elevation monitored at probe 3.

7.2.2 Free surface waves

Wave modelling is of prime importance for the wave-structure interaction problems. In this study, the presence of ship forward speed was modelled by implementing an additional uniform current at the boundary inlet and coupled with the waves based on the combined wave-current function. The encounter wave frequency was used to generate the desired the wave group. A series of regular head waves were generated ranging from ($\lambda/L = 0.9\text{-}1.6$), with a constant wave height (H=0.12m) and uniform flow speed (U= 1.80m/s). The wave shapes monitored at the wave probe WP2 were plotted in Figure 7.7. As can be seen from the figure, the CFD simulated waves (λ/L_N) are in very good agreement with the theoretical values (λ/L_T) among all wave frequencies. The decay in wave amplitude is less than 7% over time for most wave conditions. It can be concluded that the CFD method can provide reliable wave generations for the subsequent predictions of ship motion responses. The averaged wave amplitudes over the last five stable wave periods were used to further calculate the motion response amplitude operators (RAOs) in the following sub-chapters.

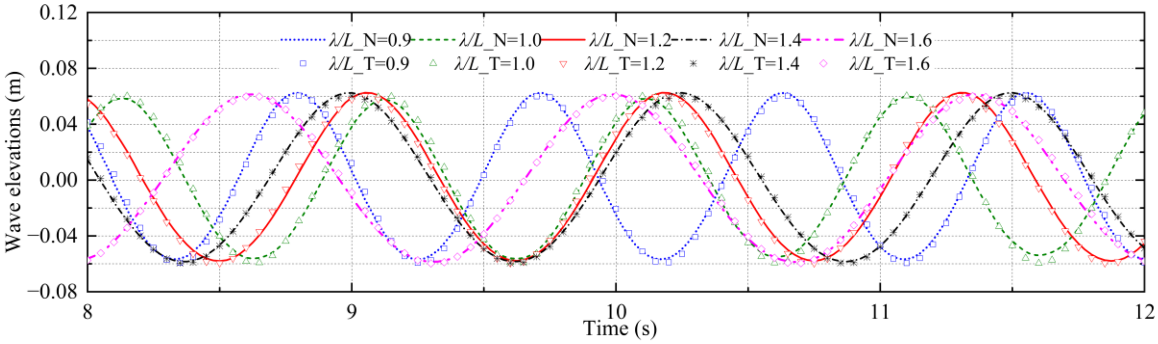

Figure 7.7: Time-series wave elevation monitored at WP2 and compared to the theoretical wave shapes.

7.2.3 Flexible ship in waves

The uncertainty study caused by the modelling and simulation of fluid dynamics by a CFD solver are generally much greater than the uncertainties associated with the structural responses by a FEA solver (Huang et al. 2022). Therefore, a verification study was undertaken on the CFD solver following the Grid Convergence Index (GCI) method (Stern et al. 2006) to assess the simulation numerical uncertainty of the flexible ship with intact condition in waves. The numerical simulation error and uncertainty U_{SN} mainly includes the accumulation from iterative error U_I, grid size error U_G and time step error U_T. It is known that the uncertainty in iteration error U_I is negligible compared with the grid size and time step (Tezdogan et al. 2015). Therefore, only the grid and time step sensitivity studies were carried out following the GCI uncertainty procedure in the present verification study.

$$U_{SN}{}^2 = U_I{}^2 + U_G{}^2 + U_T{}^2 \tag{7.1}$$

Grid and time convergence studies are performed by means of three solutions which are refined systematically with refinement ratio. Define S_{k1}, S_{k2} and S_{k3} to be the solutions with fine, medium and coarse input parameters. The subscript *k* refers to the k^{th} input parameters (i.e., *G* for grid size and *T* for time step). Differences between medium-fine ε_{k21}= $S_{k1} - S_{k2}$, and coarse-medium ε_{k32}= S_{k3}-S_{k2} solutions are used to define the convergence ratio:

$$R_k = \frac{\varepsilon_{k21}}{\varepsilon_{k32}} \tag{7.2}$$

Four kinds of convergence can occur

- $0 < R < 1$ monolithic (MC)
- $-1 < R < 0$ oscillatory convergence (OC)
- $R > 1$ monotonic divergence (MD)
- $R < -1$ oscillatory divergence (OD)

The numerical error δ_k^* and order of accuracy P_k can be estimated by the generalised Richardson extrapolation

method:

$$\delta_k^* = \frac{\varepsilon_{k21}}{{r_k}^{p_k} - 1} \tag{7.3}$$

$$p_k = \frac{\ln\left(\varepsilon_{k21}/\varepsilon_{k32}\right)}{\ln\left(r_k\right)} \tag{7.4}$$

where, r_k is the refinement ratio between three solution in grid and time step convergence studies. The GCI uncertainty U_k can then be estimated from numerical error δ_k^* multiplied by a factor of $F_s = 1.25$ to bound the numerical error:

$$U_k = F_s * |\delta_k^*| \tag{7.5}$$

In the present uncertainty study, three sets of mesh grids (i.e., fine, medium and coarse) and three sets of time step sizes were prepared to evaluate the numerical uncertainties caused by the mesh grid and time step. The wave-structure resonance condition ($\lambda/L = 1.2, H = 0.12\text{m}, U = 1.8\text{m/s}$) was selected as a representative case because large motions and loads tend to cause greater numerical errors (Tezdogan et al. 2015).

For mesh convergence study, the mesh region at free surface was refined progressively while with the mesh discretisation not altered in the background mesh. The medium time step size was selected of 0.0015s throughout all mesh convergence studies, and the total running time up to 15s with an approximate computational cost 72 CPU-hour. The detailed mesh refinement information were summarised in Table 7.5.

The time step convergence study was conducted with triple solutions using three lessened time step sizes ranging 0.001s, 0.0015s, 0.002s. The medium mesh condition G_2 was selected of representative case and the computational time consumed from the T_1 to T_3 were 96, 72 and 60 CPU-hours, respectively.

The uncertainty parameters of the amplitude values (heave, pitch and wave-induced VBMs) and the bow slamming pressure peaks (P_1 and P_2) for the mesh grids and time-step convergence were listed in Table 7.6 and Table 7.7, respectively. Moreover, the time-series of motion and pressure loads signals were plotted in Figure 7.8 between physical time of 12s to 15s. It is seen that reasonably small levels of uncertainty levels were achieved for the heave and pitch responses in both time-step and grid dependence tests. However, relatively large uncertainties U_G was estimated for the VBMs and slamming loads in mesh convergence study, mainly triggered by the numerical error from the coarse mesh. This implies that the wave and structure loads in the resonant case are very sensitive to the grid size resolution. Based on the considerations of the numerical accuracy and modelling effort, the medium mesh G_2 and medium time step T_2 were selected through all simulations in this study.

Table 7.5: Mesh gird information for convergence test.

Grid name	Hull form	Mesh	$\lambda/\Delta x$	$\lambda/\Delta z$	Gird number (million)

G_1	Intact	Fine	120	8	2.55
G_2		Medium	120	12	4.71
G_3		Coarse	120	16	6.83

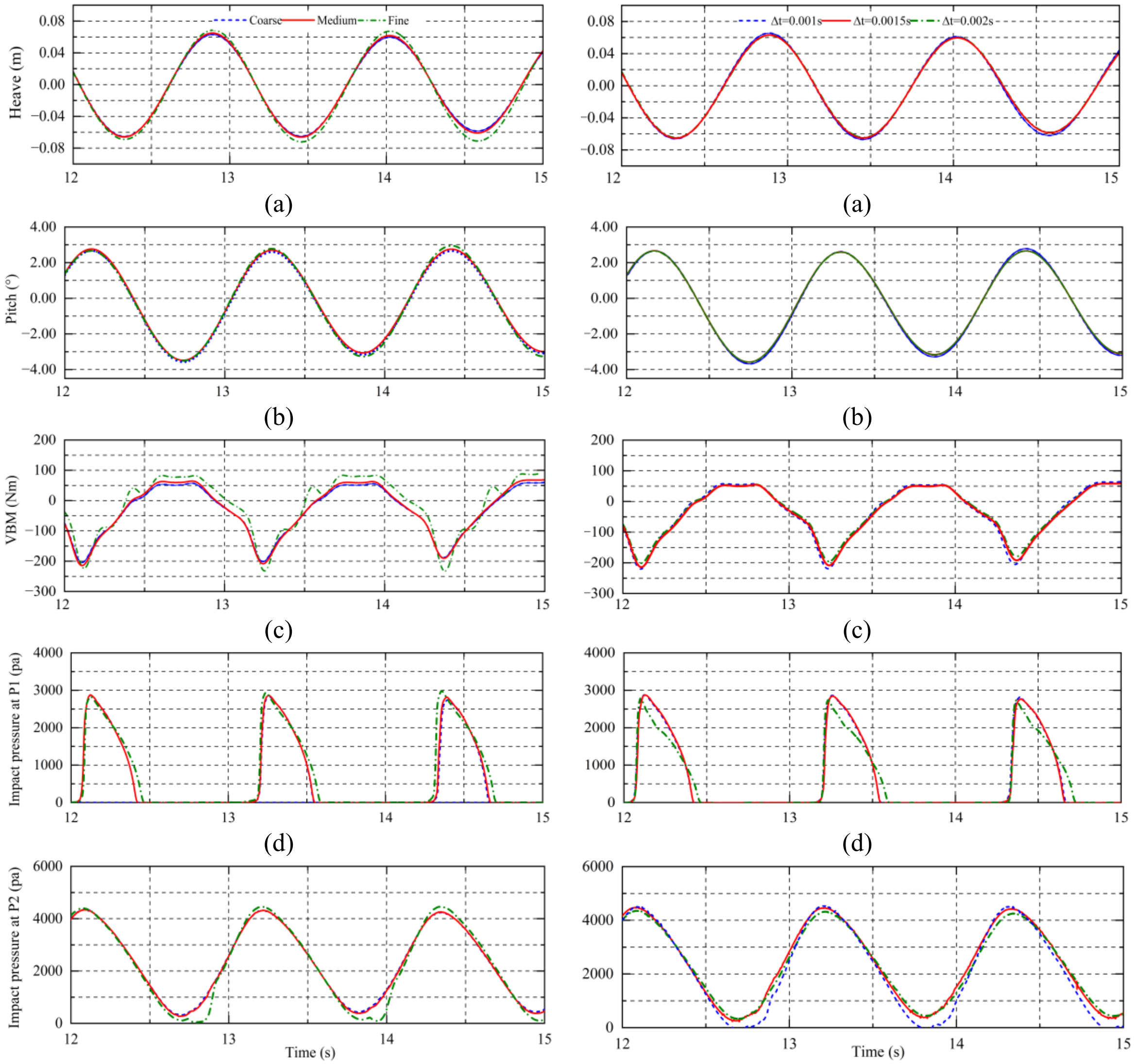

(a) (a)

(b) (b)

(c) (c)

(d) (d)

(e) (e)

Figure 7.8: Time series signals of the vertical motions, loads and slamming loads for the GCI uncertainty test.

Table 7.6: Convergence study for motions and loads by different grid schemes.

Parameter		Amplitude value			Pressure peaks	
Description	Symbol	Heave (m)	Pitch (°)	VBMs (Nm)	P_1 (pa)	P_2 (pa)
Fine solution	S_{G1}	0.0620	3.41	-234.6	2946.2	4306.0

Medium solution	S_{G2}	0.0615	3.36	-214.3	2916.1	4222.8
Coarse solution	S_{G3}	0.0608	3.28	-202.5	2907.2	4250.2
Refinement ratio	r_{G21}	1.45	1.45	1.45	1.45	1.45
Refinement ratio	r_{G32}	1.85	1.85	1.85	1.85	1.85
Convergence ratio	R_G	0.67	0.625	3.5	3.38	-3.04
Convergence type	-	MC	MC	MD	MD	OD
Order of accuracy	P_G	0.33	0.54	-0.76	5.97	-
Numerical error	δ_G^*	4.56	6.21	12.79	0.12	-
GCI uncertainty	U_G	5.97	8.27	18.33	0.16	-

Table 7.7: Convergence study for motions and loads by different time steps sizes.

Parameter		Amplitude value			Pressure peaks	
Description	Symbol	Heave (m)	Pitch (°)	VBMs (Nm)	P_1 (pa)	P_2 (pa)
Fine solution	S_{T1}	0.0619	3.39	-219.6	2969.8	4250.5
Medium solution	S_{T2}	0.0615	3.36	-214.3	2916.1	4222.0
Coarse solution	S_{T3}	0.0610	3.31	-195.5	2822.0	4206.0
Refinement ratio	r_{T21}	0.67	0.67	0.67	0.67	0.67
Refinement ratio	r_{T32}	0.75	0.75	0.75	0.75	0.75
Convergence ratio	R_T	0.57	0.60	0.30	0.56	1.75
Convergence type	-	MC	MC	MC	MC	MD
Order of accuracy	P_T	-2.44	-2.30	-4.29	-2.48	-0.32
Numerical error	δ_T^*	0.38	0.57	0.54	1.02	1.58
GCI uncertainty	U_T	0.48	0.72	0.68	1.29	5.99

7.3 Results and Discussion

In this chapter, the well-validated CFD-DMB method was further applied to understand the seakeeping and hydroelastic behaviours of the damaged ship with two damage scenarios, i.e., damaged tank numbers and tank positions. A series of time history results, including the volume of dynamic flooding water, global ship motions and structural loads of the damaged ships were presented. The virtual observations of the interactions among flooding water, seawater and the damaged ship were shown and analysed. The numerical results were then compared with the intact ship solutions and general suggestions for ship primary design and post-accident decisions were made.

7.3.1 The influence of the number of damaged tanks

In this chapter, a series of ship collision damage conditions (D1 to D3) were carried out for a systematic analysis of the damaged ship seakeeping and hydroelastic responses in head waves, as shown in Figure 7.9. As mentioned in Chapter 7.1.1, the ship collision cases were investigated by having physical openings at ship's starboard and the three damaged positions were selected with the information given in Figure 7.9. As mentioned before, all numerical investigations were performed in regular head waves with a wave height of *H*=0.12m. The ship-wave resonance frequency ($\frac{\lambda}{L} = 1.2$) was adopted to obtain pronounced motion and load responses. A typical ship speed of *Fn*=0.275 was selected to be consistent with that in the validation case.

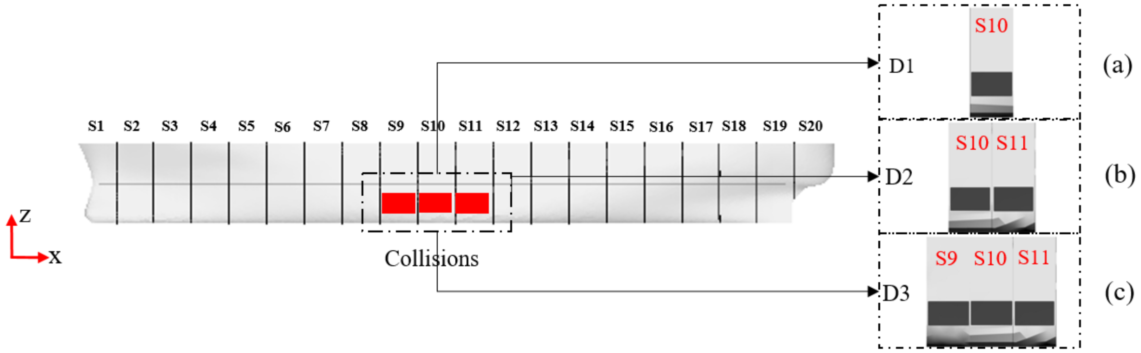

Figure 7.9: Collision damaged ship layouts at front view with three damage opening conditions: (a) D1, (b) D2 and (c) D3.

Table 7.8: Damage tank positions among damage conditions (D1, D2 and D3).

	Symbol	Full scale	Model scale
Damage opening compartment (S9) from FP	L_{S9} (m)	73	1.825

Damage opening compartment (S10) from FP	L_{S10} (m)	81.8	2.045
Damage opening compartment (S11) from FP	L_{S11} (m)	90.6	2.265

7.3.1.1 Damaged tank and flexible ship motions

The time-series of the mass of the flooding water inside the damaged ship tanks were calculated for the prescribed three collision cases (D1 to D3), as shown in Figure 7.10. It is seen that the dynamic flooding water exhibits strong nonlinearity and a certain period. The mass of flooding water rises when severe sinkage occurs due to the increase in the ship draft. It is noticeable that the signal of the flooding water mass has subtle vibration areas (shaded in the figure). This phenomenon may occur by the interactions of the internal and the external sea water when damage openings emerge to the free surface due to the ship motions.

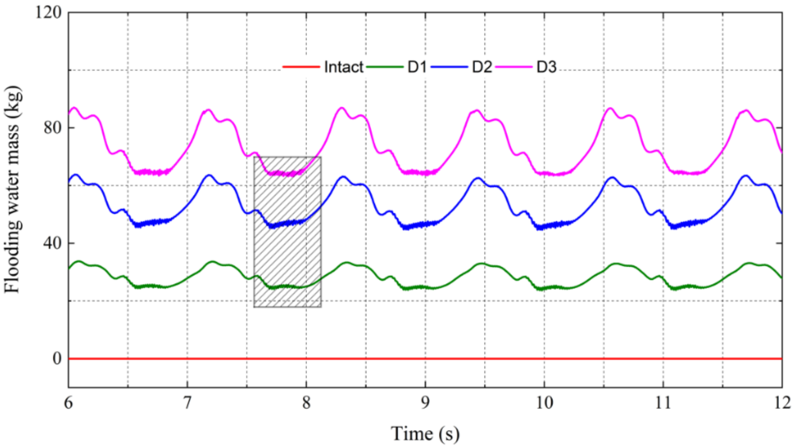

Figure 7.10: Time series of dynamic flooding water mass volume in the case of ($\lambda/L = 1.2, H = 0.12$ m) of the intact ship and compared to three damaged conditions (D1 to D3).

Physical views of the dynamic flooding water during green water events for three damaged ship cases in resonant wave condition ($\lambda/L = 1.2, H = 0.12$ m) are shown in Figure 7.11. The figure includes four snapshots inside a wave cycle, which shows the transient behaviour of the flooding water under the influence of ship motions. As it is seen that the dynamic flooding water sloshes (left and right) and heave/pitch (up and down) mildly inside the damage tanks. Meanwhile, the green water on deck phenomenon is violent through all cases, and the green water loads becomes another important issue which will further affect the responses of the hull.

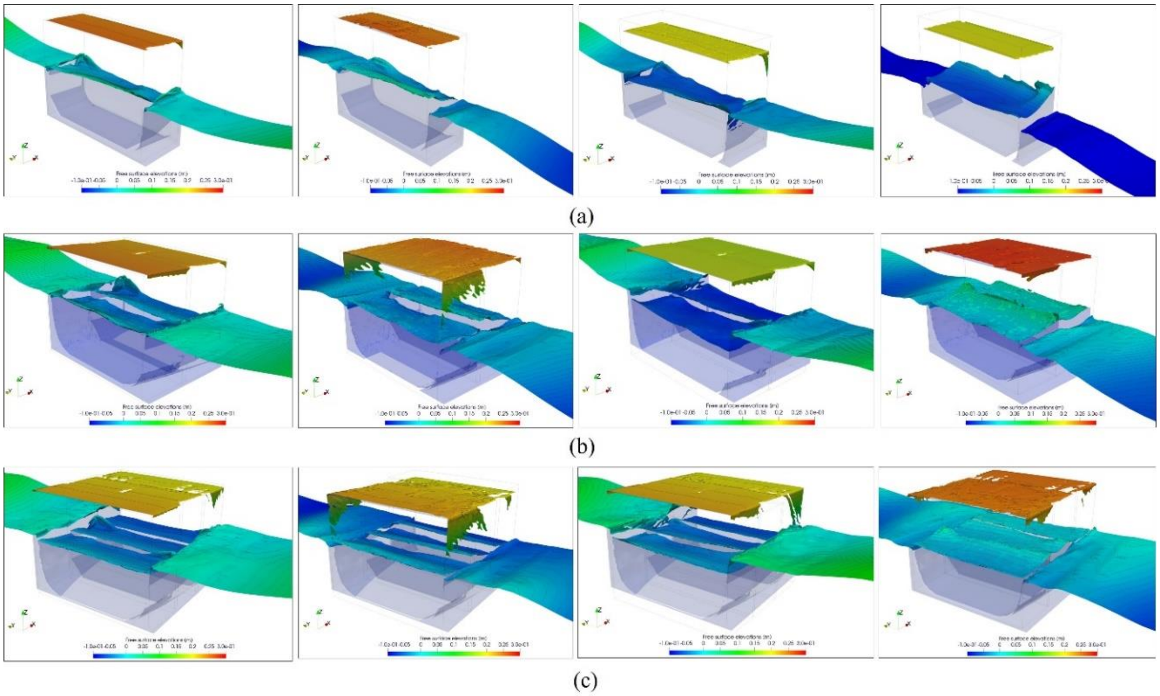
(a)

(b)

(c)

Figure 7.11: Comparison of the dynamic flooding water inside the damaged tanks in the case of $(\lambda/L = 1.2, H = 0.12$ m) among three damaged conditions: (a) D1, (b) D2, (c) D3.

The vertical ship motions (heave and pitch) for the ship at intact and damaged conditions are studied in this chapter. The motion responses were measured on the beam node which is close to the ship's centre of gravity at a longitudinal position x = 2.125m from the aft perpendicular, corresponding to 0.486L. The original time-series of the heave and pitch motions of the ship in intact and three damaged conditions are shown in Figure 7.12. For heave and pitch signals, the positive sign represents the emergence of the ship and its trim by bow, respectively. It can be seen from the figure that the vertical motion signals of the intact and damaged ship at steady run region are in good accordance with standard sinusoidal signal in shape, which presents the same sinusoidal characteristics of the induced wave. The obvious ship sinkage can be found in the heave signals of the damaged ship conditions, due to the additional loads acting from the flooding water inside the damaged tank, i.e., hydrostatic and sloshing loads and thus changes the seakeeping behaviour of the ship.

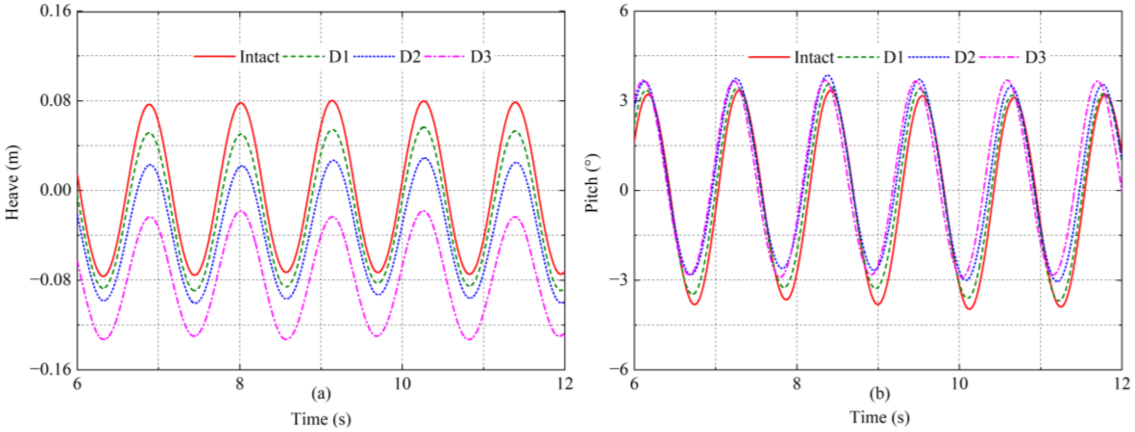

Figure 7.12: Time series of vertical ship motion responses in the case of ($\lambda/L = 1.2, H = 0.12$ m) of the intact ship compared to three damaged conditions (D1, D2 and D3): (a) heave motion, (b) pitch motion.

The peak and trough values of the intact and damaged ship motions and their RAOs are summarised in Figure 7.13, which show the effects of damaged tank numbers on the damaged ship vertical motions. As can be seen from the results, it can be concluded that the heave and pitch responses reduced gradually from the intact ship condition to D3 with the growth of the intake water volume and the damage tank numbers. Similar results were also found by Fols∅ et al. (2008) and Lee et al. (2012) which supports the findings. In this case, the trough heave RAO value is much greater than the crest which indicates that the damaged ship was subjected to an obvious sinkage due to the added weight effects of the intake water inside the damaged tanks. For pitch motions, it can be seen that the intact ship initially experiences trim by bow motion and gradually shift towards to stern motion due to the changes of the longitudinal load distributions caused by the dynamic flooding water.

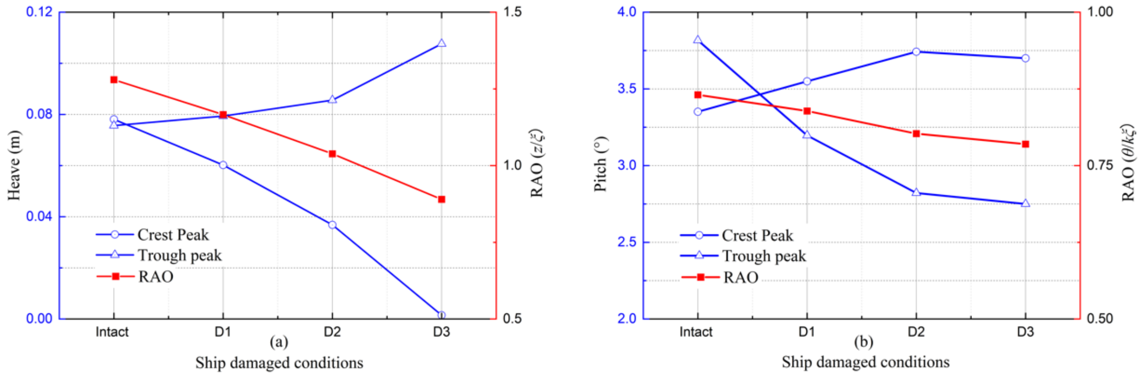

Figure 7.13: Peak value distribution of ship motions in the case of intact ship and three damaged conditions (D1 to D3) (a) heave motions (b) pitch motions

7.3.1.2 Still water VBMs of the ship

The calculated beam sectional loads for a damaged ship include the contributions of still water loads (S_VBM), wave-induced loads and flooding water loads. It is necessary to estimate the hull girder bending moments in still water primarily since it expresses the structural loads that a ship may experience during the vast majority of her service at sea. As aforementioned in Chapter 7.13, the sectional loads at each ship section ranging from S1 to S19 were monitored for the intact and damaged ship in still water at a steady state and the peak values were extracted and shown in Figure 7.14. The literature data (Jiao et al. 2021) for longitudinal distributions of still water VBM for the intact ship are also presented in the same figure for comparison and validation. The positive and negative of VBMs denote hogging and sagging loads, respectively. It can be seen that the S_VBM estimated by the present CFD-DMB method shows a similar trend with the results from the CFD-FEA method (Jiao et al. 2021), although the presented results slightly overestimate the hogging magnitudes of about 8.6% near the amidship sections. This deficiency may stem from the selections of different numerical methodologies and time steps. It can be seen from Figure 7.14(b) that the intact ship stays in a perpetual hogging condition in still water and the maximum magnitude is achieved at Section 10 with a value of 256Nm. Similar findings were also obtained by Bouscasse et al. (2022)'s experimental study which found a 6750-TEU ship experiences perpetual hogging condition in still water. The magnitude of S_VBM reduced significantly at the damaged ship sections; the most obvious reduction can be found at the amidship section, i.e. Section 9.

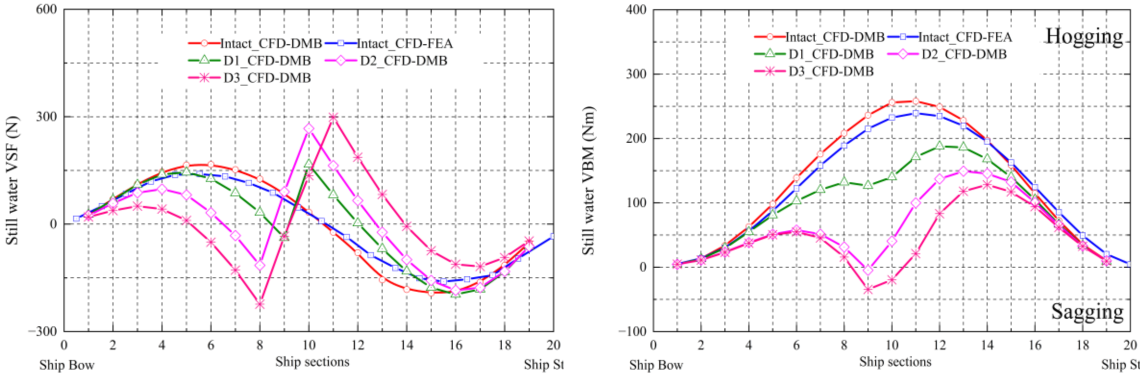

(a) (b)

Figure 7.14: Hull girder loads of the ship at intact and damaged conditions with a comparison to the FSI simulations by Jiao et al. (2021): (a) Still water vertical shear forces (S_VSF), (b) Vertical bending moments (S_VBM).

7.3.1.3 Wave and flooding water induced vertical bending moments (W_VBMs)

The wave and flooding water induced VBMs (W_VBMs) were calculated by subtracting the S_VBM from the total vertical bending moments (T_VBM). The time-series signals of both intact and three damaged ship conditions are summarised in Figure 7.15. It can be seen that all W_VBMs show strong nonlinearity and asymmetric behaviours in which the sagging moments are dominant due to the vertical ship motions in waves.

An interesting finding is that as the number of damaged tanks and the volume of intake water increases, the trough of sagging moments basically does not change, however, a noticeable increase can be found in the peak hogging moments. A low pass filter was applied to divide the W_VBMs data into two parts: the WF component (1st order harmonic wave loads) and HF components (includes high-order structure loads and nonlinear flooding water-induced loads). The time-series of the WF and HF components are plotted in Figure 7.15 and their peak and trough values are summarised in Table 7.10. The results indicated pronounced HF components at the midship hull girder, and the magnitude of the HF components increased with the number of the damaged tanks from 57.2Nm (intact) to 91.4Nm (D3). The relevant frequency spectra of the W_VBMs of the ship at intact and damaged conditions were shown in Figure 7.16. It is seen that the first-order harmonic wave encounter frequency and the springing frequency (up to 7th harmonic) showed good agreement between the target and calculated values. However, the peak value of the 2-node whipping frequency was generally lower than the values presented by coupled CFD-FEA models from (Jiao et al. 2021). This deficiency may be caused by three potential reasons: 1) Multibody formulation of three-node beam elements in MBDyn. The constraint equations were applied on beam elements as boundary conditions, which may introduce additional spurious eigenmodes related to the Lagrange multipliers. Usually, these eigenvalues related to those spurious modes may have a high damping value. 2) The implementation of structural damping in MBDyn. The damping effects on structural loads were studied by Lakshmynarayanana et al. (2020), which pointed out that the increase of structural damping from 0 to 0.01 may cause the reduction of the bending loads by about 25%. However, in the present study, it is necessary to apply structural damping to stabilize the structural solver and represent the material's actual damping behaviours. 3) Coupling algorithm inside the CFD-DMB framework. The implemented two-way loose coupling algorithm may cause deficiencies in capturing high-frequency components by comparison with a two-way strong coupling scheme. In general, the high-frequency components ($f > 8.0$ Hz) contributed less than about 5% of the total VBMs. The peak and trough values of the W_VBMs predicted by the present CFD-DMB method were shown generally acceptable agreements with both co-simulation results from Jiao et al. (2021) and experimental results from Chen et al. (2001). A systematic analysis of these potential issues will be presented as a future study.

Both WF and HF components of W_VBMs are non-dimensionalised by $M/\rho g L^2 B \xi$ and their peak values are plotted in Figure 7.17. The numerical results show that the damaged tank numbers have less effects on the trough sagging moments, however, a growth of WF and HF hogging moments by about 26.9% and 31.5% can be noticed at three tanks damaged condition (D3) compared to that in intact ship. Similar results were also achieved by Begovic et al. (2013) and Begovic et al. (2017)'s experiments, in which a 28% of W_VBMs increase was reported for a damaged ship in head seas compared to the intact ship.

Table 7.9: Numerical results of ship with intact and damaged ship conditions (D1, D2 and D3).

	Heave RAOs	Pitch RAOs	Peak Hogging moment (Nm)	Trough Sagging moment (Nm)	S_VBM (S10) (Nm)	Initial draft (m)
Intact	1.28	0.87	93.2	-233.6	256.5	-0.025
D1	1.16	0.84	115.4	-234.0	147.0	-0.035
D2	1.04	0.80	131.9	-228.6	40.5	-0.050
D3	0.89	0.78	145.0	-230.0	-19.59	-0.075

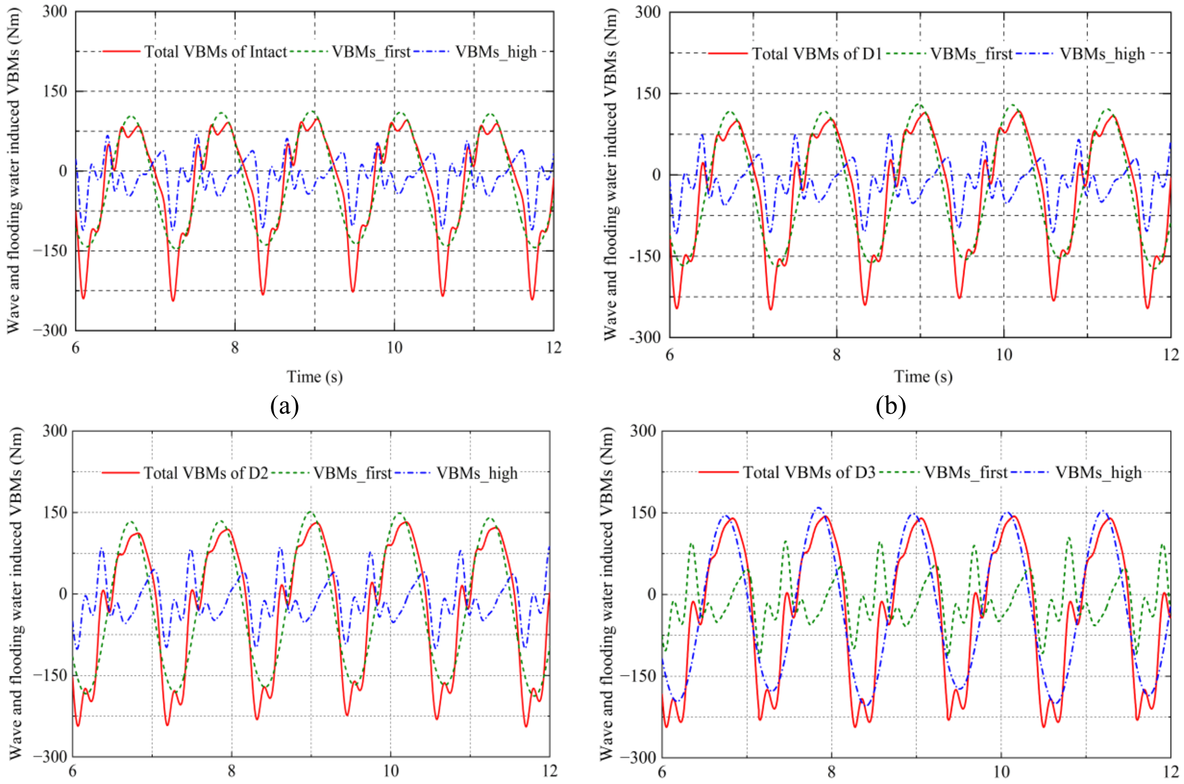

(a) (b) (c) (d)

Figure 7.15: Wave and flooding induced vertical bending moments in the case of ($\lambda/L = 1.2, H = 0.12$ m) of the (a) intact ship, (b) D1, (c) D2, (d) D3.

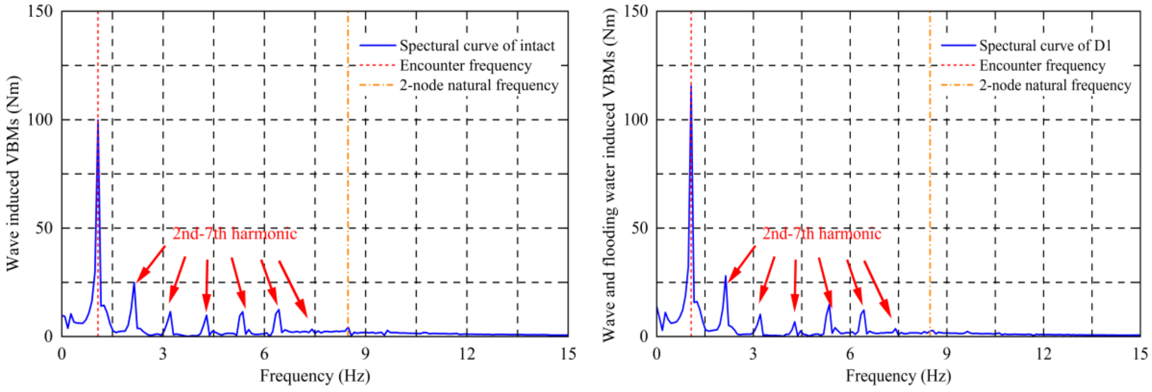

(a) (b)

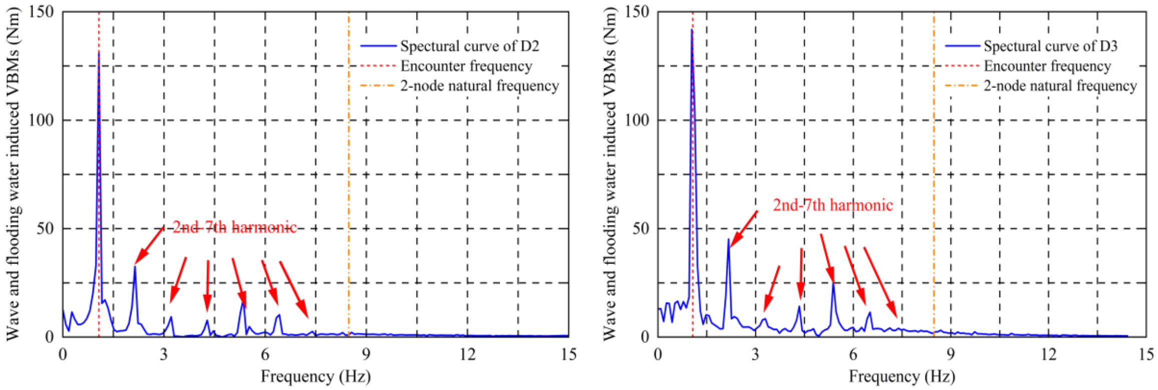

(c) (d)

Figure 7.16: The frequency spectra analysis of the wave and flooding induced VBMS in the case of $(\lambda/L = 1.2, H = 0.12$ m) of the (a) intact ship, (b) D1, (c) D2, (d) D3.

Table 7.10: Peak and trough values of the first harmonic and high frequency of the W_VBMs.

	VBM_first harmonic (WF)		VBM_high frequency (HF)	
Ship conditions	Peak	Trough	Peak	Trough
Intact	112.1	-138.1	57.2	-105.5
D1	125.3	-165.3	67.5	-104.2
D2	142.2	-173.2	82.6	-98.6
D3	153.5	-185.2	91.4	-106.8

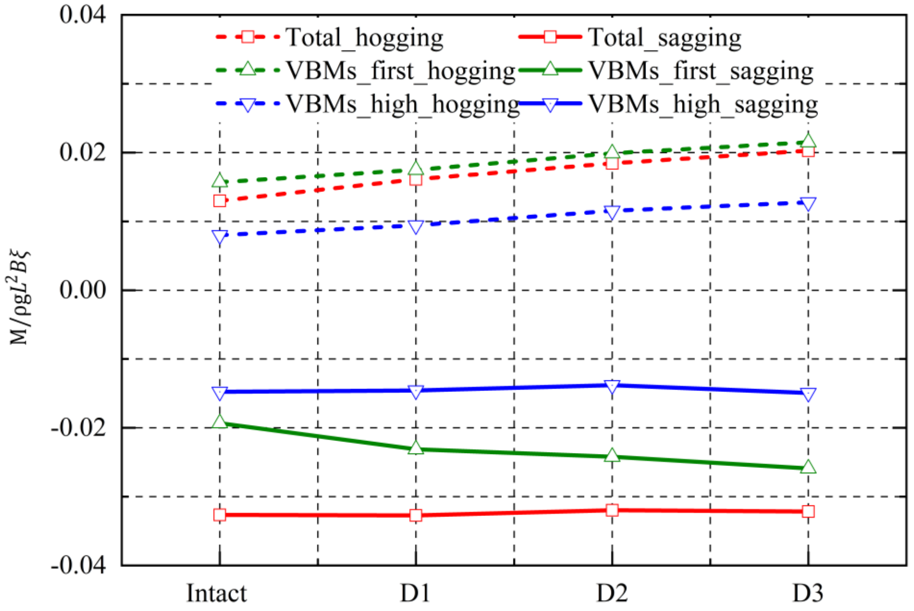

Figure 7.17: Non-dimensional W_VBMs in the wave condition $(\lambda/L = 1.2, H = 0.12$ m) of the intact ship and the damaged conditions (D1 to D3).

The predicted W_VBMs of the damaged ship at the cases of (D1-D3) were further compared to the new longitudinal strength standard for containerships URS11A issued by the International Association of Classification Societies (IACS,2005), as shown in Figure 7.18. It can be seen that the URS11A regulation (Black solid line in figure) preserved large margin for the negative sagging moments due to the contributions of slamming-induced loads for ship in extreme waves, however, a very limited margin is reserved for the positive hogging moments. As can be found in Figure 7.18, the predicted hogging moments at certain damaged ship sections exceed the limits proposed by the regulations, i.e., ship section 9 in the case of D2 and ship sections 8-10 in the case of D3. The excessive local W_VBMs may accelerate ship hogging deformation, which may result in the material buckling and further structural damages. This phenomenon may be one reason of MOL comfort accident, when buckling deformation occurs on the bottom shell plating, the intake water flushes inside the damaged tank and forces ship hogging until structural failure occurs. Although, a partial safety factor γ_{DB} for the hull girder hogging capacity was introduced in URS11A as 1.15, this factor may not be sufficient since the structure failure and buckling may occur while ship operates at ultimate strength. On the basis of the above results, this factor is recommended to be increased to be above 1.35 (shown in Figure 7.18 with purple line) for damaged ship design in order to leave a safe margin of hogging moments to reduce the risk of secondary damages.

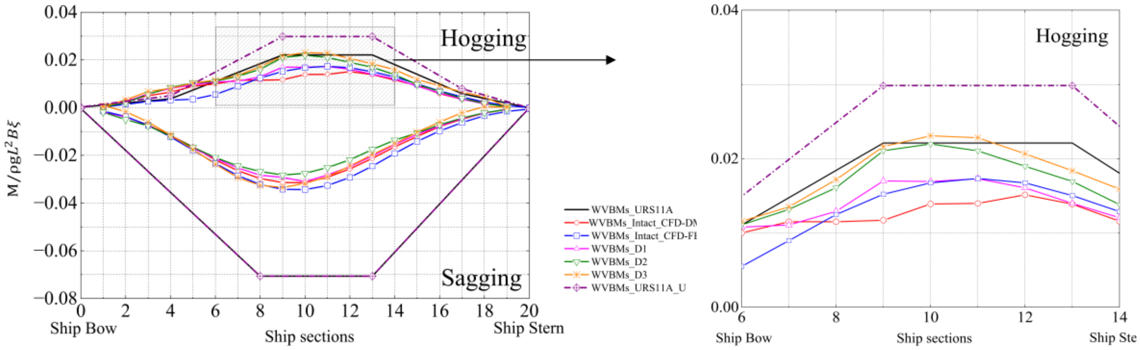

(a) (b)

Figure 7.18: Longitudinal distributions of W_VBMs for the intact, damaged ship conditions (D1, D2 and D3) and URS11A regulation: (a) Normal version, (b) Zoomed version.

7.3.2 Analysis of the positions of damaged tanks

The influences of the damaged tank positions on the damaged ship seakeeping and hydroelastic responses were carried out in this sub-section utilising the present CFD-DMB method. Three different damaged tank positions were analysed and shown in Figure 7.19, i.e., the damaged opening located at 5th, 10th and 15th stations from the bow in the cases of D4, D1 and D5, respectively. The detailed positions of each damage tank were summarised in Table 7.11. The same environment setting up as adopted in Chapter 7.3.1. The model description was preserved in the CFD solver, in which the damaged ship operated in the ship-wave resonance frequency ($\frac{\lambda}{L} = 1.2, H = 0.12m, U = 1.8\text{m/s}$).

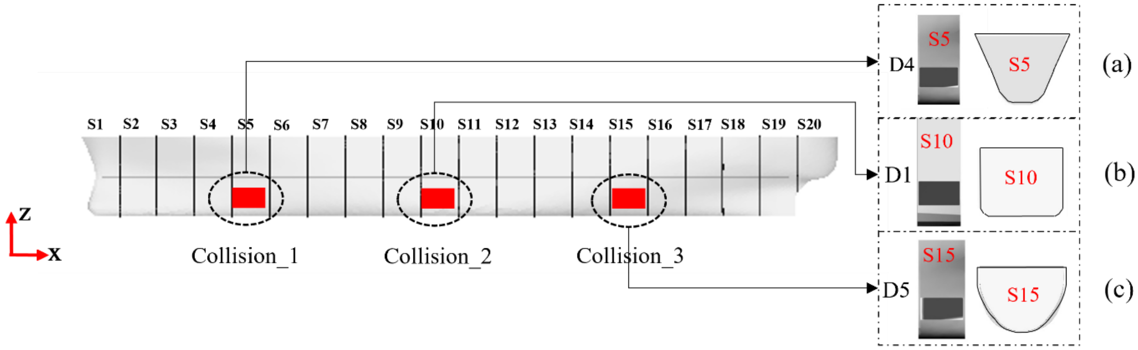

Figure 7.19: Collision damaged ship layouts at front view with three damage opening conditions: (a) D4, (b) D1 and (c) D5.

Table 7.11: Damage tank positions among damage conditions (D4, D1 and D5).

	Symbol	Full scale	Model scale
Damage opening compartment (S5) from FP	L_{S5}(m)	35.8	0.895
Damage opening compartment (S10) from FP	L_{S10}(m)	81.8	2.045
Damage opening compartment (S15) from FP	L_{S15}(m)	127.76	3.194

7.3.2.1 Flooding water mass and vertical ship motions

The estimation of the flooding water inside the damaged tank is significant, it mainly depends on the responses of the damaged ship; in return, the ship responses are also affected by the dynamic flooding water. The mass of the dynamic flooding water of the three damage conditions (D4, D1 and D5) were calculated and shown in Figure 7.20. It is seen that the flooding water volume was greatly related to the damage locations. The maximum mass of flooding water was found in D1 due to the largest cross-section of the tank among the others. Meanwhile, the intake flooding water shows high nonlinearity for each damage condition; no certain period exhibited among these signals due to the complex interaction among the intake water, seawater and damaged ship.

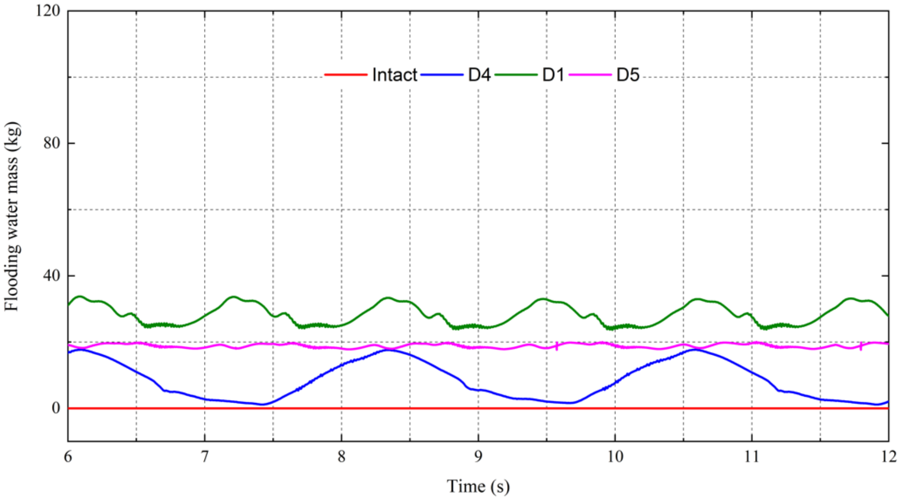

Figure 7.20: Time-series signal of the mass of the dynamic flooding water of the intact and damaged ships.

Virtual observations of the flooding water profile inside the damaged tank are compared among three damaged conditions (D4, D1 and D5), as shown in Figure 7.21. It can be found that the damaged positions lead to different patterns of flooding water motions. In the case of D4, the water level rises and drops periodically in a sudden way due to the large amplitude of the pitch bow motions, while in D1 the water level changes much more smoothly. It is clear to see that the nonlinear sloshing effects are stronger in D5, in which the flooding water climbs up and impacts on the inner wall of the tank. For future studies, the region inside the damaged tank will apply a high-level mesh refinement to capture the local violent sloshing phenomenon.

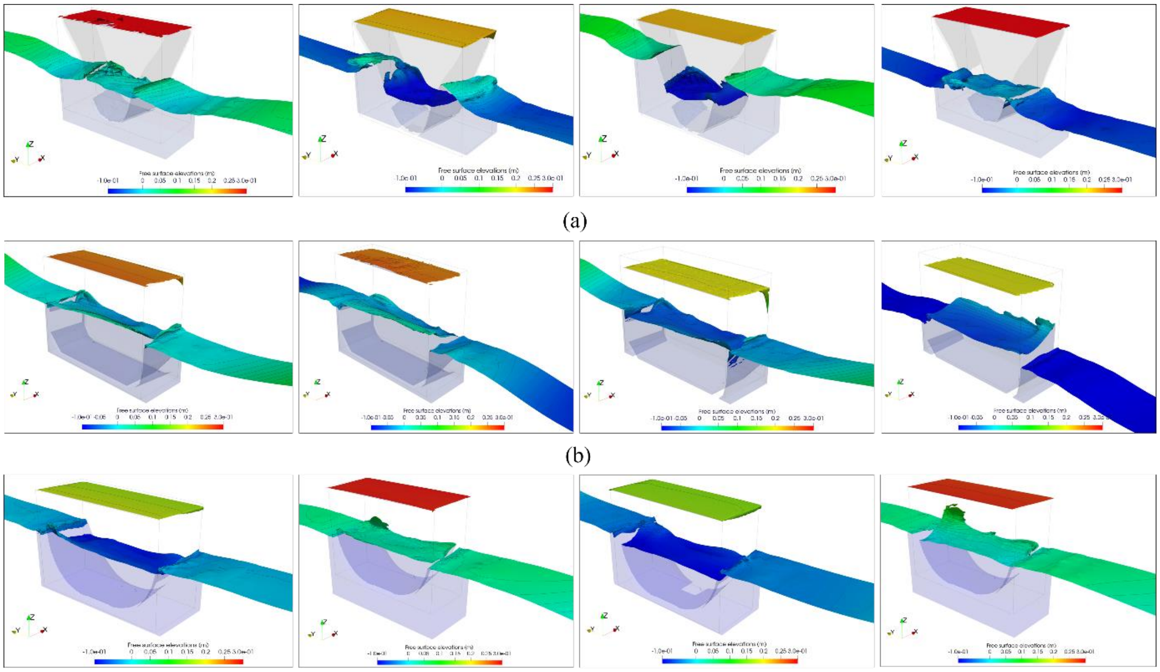

(a)

(b)

(c)

Figure 7.21: Dynamic flooding water inside the damaged tanks comparison in the case of ($\lambda/L = 1.2, H = 0.12$ m) among three damaged conditions: (a) D4, (b) D1, (c) D5.

To investigate the effects of damaged tank locations on ship motions in head waves, the peak, trough values of the heave and pitch responses and their RAOs at three damaged ship conditions were shown in Figure 7.22 and compared to the results in the intact condition. It can be seen that the peak values of the heave and pitch motions are varied due to the fluctuations of the loading distributions among the three damaged conditions; accordingly, the KG and draft of the ship are modified so that the natural resonance periods of motions are shifted accordingly. It can be found that the damage opening at the amidship (D1) reduces both heave and pitch responses compared to the damages at ship section 5 (D4) and section 15 (D5). Meanwhile, the damaged tank position shifts the pitch from the bow motion (D4) to the stern motion (D5).

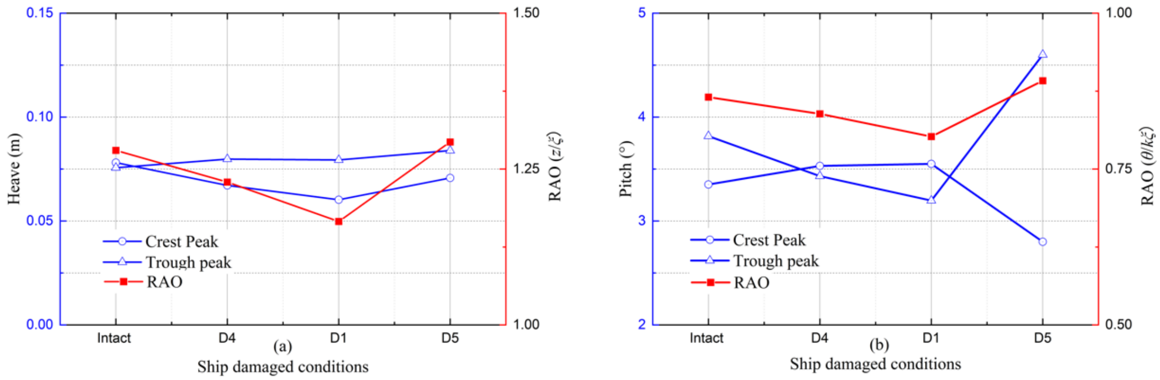

Figure 7.22: Peak value distribution of ship motions in the case of intact ship and three damaged conditions (D4, D1 and D2): (a) heave motions, (b) pitch motions.

7.3.2.2 Vertical bending moments

The longitudinal distributions of the wave and flooding water-induced VBMs are non-dimensionalised at different ship sections for the intact ship and damaged conditions (D4, D1 and D5), as shown in Figure 7.23. It can be seen that for the cases with only one damage tank, the peak and trough values of W_VBMs do not change significantly. However, the peak value of the hogging moments is found to shift along the ship longitudinal from ship section 9 (D4) to section 12 (D5). The peak hogging values of the intact and damage conditions are further compared with the URS11A regulation in Figure 7.23(b), from which it can be concluded that the W_VBMs of the ship with a single damage tank regardless the damage tank position stay within the regulation limits.

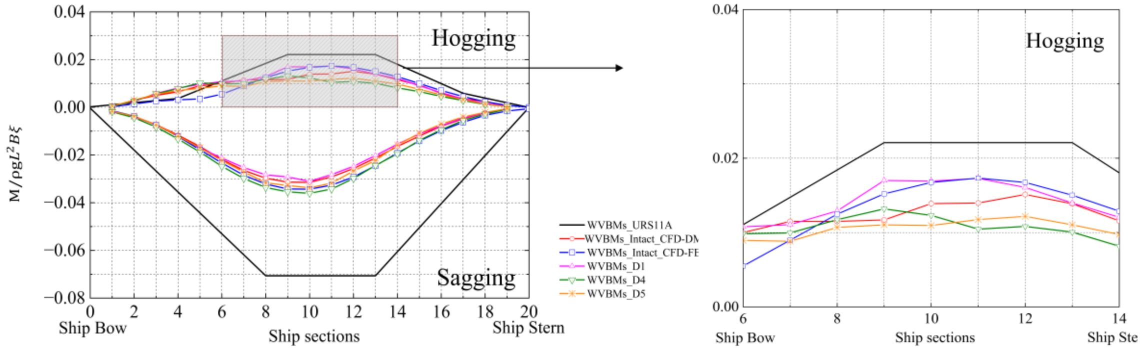

(a) (b)

Figure 7.23: Longitudinal distributions of W_VBMs for the intact, damaged ship conditions (D4, D1 and D5) and URS11A regulation: (a) Normal version, (b) Zoomed version.

7.4 Conclusion Remarks

This paper presents a two-way coupled FSI framework to investigate the hydroelasticity of an S175 containership at intact and two damaged scenarios in regular heading waves with operational speeds. The coupled CFD-DMB numerical tool was established, and in particular, OpenFOAM was chosen as the fluid solver, while the MBDyn was selected as the structure solver to solve the deformation of flexible structures. A two-way implicit algorithm was implemented for robust coupling and allow data communication between the fluid and structure solvers.

Two validation studies were presented first to evaluate the free surface capture capability of the multi-phase solver under severe sloshing conditions and wave-current generation conditions. The numerical results, including the measurements of the free surface elevations inside a 2D sloshing tank and the Stokes 2^{nd} wave profile were shown in good agreement with the experimental results and the theoretical values. Later, a GCI uncertainty test was carried out for CFD solver on the seakeeping behaviours of a deformable intact ship in the wave-resonance ($\lambda/L = 1.2, H = 0.12$ m) condition. The influences of the mesh grids and time step sizes which configured in CFD solver were evaluated by a series of numerical results, which including the vertical ship motions (heave and pitch), structural loads at the midship section (VBMs) and slamming impact loads of the containership.

Afterwards, the seakeeping and hydroelastic analysis of the flexible ship with three damaged conditions (D1 to D3) in heading waves are carried out using the present CFD-DMB method. The flooding water sloshing inside the damaged tanks and the exchange with the surrounding sea water was considered, detailed information, i.e., the time-varied volume flux and the virtual observations were drawn in Figure 7.20 and 7.21, respectively. According to the numerical results, the heave and pitch motions at the case with three damaged tanks (D3) reduces about 30.5% and 10.3% compared to the intact ship. Meanwhile, it is seen that clear sinkage and the shift of trim from bow to stern motion in time-series result (shown in Figure 7.13) due to the variations of damaged loading conditions caused by the flooding water. The ultimate strength of the hull girder for a damaged hull was calculated in this study by reducing the equivalent beam stiffness and applying strength reduction factors to account for loss of structural stiffness. The main finding is that the total VBMs at D3 is 30.3% larger than that of the intact ship, similar result found by experiments (Begovic et al. 2017) for a DTMB 5415 ship model was 28%. In addition, the dynamic flooding water inside the damaged tanks was found to have a significant effect on the still water VBMs. The W_VBMs are calculated from subtracting the S_VBMs from T_VBMs. The results show that the peak hogging components of W_VBMs rises with the increase of mass of flooding water, however, the trough sagging moments experienced less effects. The W_VBMs further compared to the new legislation of USR11A, which pointed out the hull girder hogging moments may less predict by the regulation. The local W_VBMs at ship mid sections at the cases of D2 and D3 have been found to exceed the regulations limits by about 0.65% and 4.7%, respectively. In such circumstances, the structure may experience buckling and failure due to frequently operating in ultimate strength condition, which may result in secondary damage to the ship. Therefore, a safety factor of 1.35 is recommended in this paper based on the safety considerations which accounts for the increase of hogging moment induced by the dynamic flooding water.

The dynamic analysis was further carried out on the damaged scenarios with three damaged positions (D4, D1 and D5) to interpret the ship's elastic behaviours after collision damages. Virtual observations such as profile of flooding water surface, green water on deck and various hydrodynamic components were available in the numerical simulations. This information greatly facilitates analysis of the interactive dynamics of damaged ship, sea wave and flooding water. The ship hydroelasticity was studied based on the present FSI model with some important outputs, i.e., when damage opening located at amidship (D1), the ship responses of the heave and pitch became smaller, but the T_VBMs was found the largest among the intact and other damage positions (D4 and D5). Meanwhile, the peak W_VBMs will shift along ship longitudinal direction based on the flooding tank position, i.e., section 9 at D1 and D4, section 12 at intact and D5. It can be further concluded that the damage of a single tank regardless its location will not cause the local VBMs exceeded than that in regulation (IACS 2015), therefore, in such condition, the captain can prevent secondary accidents through the ascertainment of its cases and circumstance to make post-accident decision with less consideration of ship hydroelastic effects. Future work will present an experimental study on the flexible damaged ship with different damage scenarios in regular heading waves.

8 Conclusions and Future Research

8.1 Introduction

This chapter will present a summary of the main outcomes of the studies discussed in this thesis, along with a clear demonstration of how the research aims and objectives have been achieved. Following this, a brief discussion on the FSI methods will be given. Finally, recommendations will be presented for relevant fields of future research which are related to the work presented in the main chapters of this thesis.

8.2 Conclusions

The first research objective listed in Chapter 1 was as follows:

> *"To review the available literature on ship hydroelasticity and to investigate the advantages and drawbacks through various prediction techniques."*

The 'Critical Review' in Chapter 2 addressed this research aim. It began with an overview of wave-ship interaction problems and hydroelasticity methods, starting from models with a rigid ship and progressing to state-of-the-art flexible ship simulations. A comprehensive literature review on developing numerical methods of ship hydroelasticity was illustrated , followed by a discussion of the strengths and weaknesses of each theory. The chapter also provided a literature survey on the specific applications, such as, the influences of global ship elastic behaviour on the dynamic ship motions and vertical loads in Chapter 2.3, the prediction of hull girder stress at extreme wave conditions in Chapter 2.4 and the estimation of damaged ship hull girder stress with the consideration of hydroelasticity in Chapter 2.5. Finally, the conclusion of the chapter listed the gaps detected during the literature review.

The following two objectives were achieved in Chapter 4.

> *"To evaluate the optimal setting-ups in OpenFOAM by conducting a CFD application of a CTV operating in heading waves."*
> *"To evaluate the performance of 1D beam modelling among FEA, DMB and theoretical methods and discuss their capabilities of extending to the ship applications."*

The global ship structure was represented as a three-node beam with equivalent stiffness throughout the project. Two different beam demonstrations based on the finite element method (FEM) and multi-body dynamics (MBD) were evaluated using a fixed end cantilever beam. The numerical results were compared to the experiments, and a discussion followed.

Afterwards, the numerical setup of the OpenFOAM was explained in detail. Before providing the CFD results, validation and verification studies were carried out. A low-draft catamaran was used as a case study, providing service without forward speeds in regular wave conditions. Its operability indices were calculated based on predetermined human comfort seakeeping criteria. Overall, the presented CFD method accurately predicted the motion responses and hydrodynamic loads of a ship in regular head waves.

The OpenFOAM and MBDyn solvers were coupled together for FSI simulation. The benchmark flexible barge model in waves was utilized for the representation cases. By taking advantages of the proposed FSI simulation, the displacements at each barge segment were predicted and compared to the experimental results with favourable agreement. Finally, the sectional loads obtained at barge amidship were compared with the other methods (such as EFD and co-simulation between StarCCM+ & Abaqus). The comparison clearly showed that the present CFD-DMB method accurately predicted the midsection load values over various wave frequencies.

The following objectives were achieved in Chapter 5.

> *"To establish an open-source CFD-based FSI coupling approach to predict the dynamic motions and sectional loads of a containership operating in head seas."*
> *"To demonstrate the sensitivity and uncertainty of the adopted CFD-FEA model for a flexible containership sailing in regular waves."*

In Chapter 5, fully coupled CFD-FEA simulations were performed to predict the dynamic motions and hull girder stress of a selected S175-type containership operating in heading seas. Only the resonant case, when the encounter frequencies of these harmonics were close to the natural frequency of the wet two-node vibration mode, was analyzed to elaborate on the influences of higher harmonics to the vertical bending moments in regular waves. The predicted flexible ship motions were compared to those from rigid body models to show the contributions of ship hydroelasticity on structural responses. Then, the predicted hull girder stress was compared with the values from the co-simulation (Jiao et al. 2021) and experimental results. However, one drawback of the present CFD-FEA model on ship hydroelasticity was the large computational burden induced by the FSI algorithm and data mapping scheme. As an alternative, a novel FSI coupling approach between the CFD-DMB method was applied for the dynamic ship motions and hull girder stress of a containership under wave excitations. A general discussion of the strengths and weakness of the proposed two FSI frameworks: CFD-FEA and CFD-DMB methods, was presented at the end of this chapter.

The next objective was address in Chapter 6.

> *"To tackle the huge computational burdens which induced by the CFD-FEA coupling method, an efficient CFD-DMB framework is established using an efficient two-way loose coupling algorithm."*
>
> *"To predict the extreme wave loadings on a flexible containership, the CFD-DMB approach was carried out on the applications in response-conditioned waves for short-term nonlinear analysis."*

The research reported in Chapter 6 concerned the ship's hydroelastic behaviour and slamming loads in extreme waves based on a fully coupled CFD-DMB framework. First, a series of verification and validation studies of the present CFD-DMB method on a flexible containership in regular waves were presented. Next, extreme ship behaviours were studied in focused wave conditions to represent extreme sea conditions that a ship may experience in a real sea state. The irregular sea states used in the investigation were representative of North Atlantic Sea spectrum. Later, the paper presented the short-term time history curves of the vertical sagging and hogging bending moments of the flexible ship in focused wave condition. With this, the paper illustrated the asymmetry behaviour between the sagging and hogging moments and how much these moments were affected due to hull flexibility. The results obtained from these improved and validated numerical tools can provide a clearer and more detailed insight into the physical phenomena of the ship's dynamic motions and its hydrodynamic loads in real sea states. The results proposed in this study also help to access the structural integrity of the ship longitudinal strength, which serves an improved technique to evaluate unconventional ship designs.

The following objectives were achieved in Chapter 7.

> *"To investigate the influences of the surface hull damages on damaged ship motions and residual hull girder stress considering ship hydroelasticity."*
> *"To better understand of the local flooding water dynamics inside the damaged compartment."*

This chapter studied the number of damaged compartments and their positions based on the proposed CFD-DMB model to investigate their effect on flexible ship seakeeping and hydroelastic behaviour. Similar numerical settings as Chapter 6, yet the results included values for the influences of damage openings on the flexible ship motions and vertical bending moments. This will help to gain more insight into the understandings of the dynamic damaged ship behaviour in waves, including the interactions between the flexible ship and flooding water, the violent free surface phenomena (e.g., sloshing) and longitudinal structural load distributions.

This study will be valuable in better assessing the damaged ship behaviours and the wave-induced global and local loads with the consideration of ship hydroelasticity, which assists in rapid decision-making relevant to post-damaged evacuation and maintenance. The results of this paper will also shed some light on improving the current legislation on the safety of ships in damaged condition by the international SOLAS (Safety of Life at Sea) convention.

8.3 Discussion

This work focused on the numerical developments of transient CFD-based FSI simulations to investigate various ship hydroelasticity problems. Two elaborated coupling frameworks, the CFD-FEA and CFD-DMB methods, were established in the time domain, and the numerical results were validated well with experiments. The main results drawn from this work were summarised and discussed in detail in the previous chapters. This chapter elaborates on a general discussion of the problems that may arise in numerical simulations.

Wave-structural interaction problems involve some level of coupling between different physical fields (e.g., structural deformation, fluid flow, temperature, etc.). In the past, due to insufficient computational capabilities, these coupling effects were ignored or approximated. However, with the ever growth computational power, the elastic behaviour of the structure under fluid excitation is taken into account in this study. While pursuing such coupling system, each partner inside the FSI system should take with care. A general summary of issues that have arisen during the simulation is discussed below.

Generating a finite volume mesh is a challenging issue. In this work, the mesh generation utility SnappyHexMesh, supplied with OpenFOAM, is used to generate an unstructured mesh. The process of generating a mesh using SnappyHexMesh involves three steps: castellatedMesh, snap and addLayers. It is recommended to ensure that mesh has good quality at each step before moving on to the next.

The mesh motion solver, displacementLaplacian, is a generic mesh technique in OpenFOAM that solves the cell-centre Laplacian for motion displacement and morphs the mesh to accommodate structural deformations. However, this dynamic mesh technique may not be appropriate for cases with large motions, as the cell grids can be distorted by large deformations, resulting in a crushed model. In general, sliding mesh or overset mesh should be used as an alternative and should cooperate with the displacementLaplacian motion solver, allowing cells to have relative motion and deformations.

The time-step size is a significant numerical parameter for a transient FSI simulation. In the coupled analysis, time integration involves solving the partial differential equations for both the fluid and structure solvers. To ensure convergence, a convergence test should be performed to determine the appropriate time-step size. If the time step size is too large, an error due to temporal discretization can cause numerical instability in implicit integration schemes. In the presented FSI frameworks, the time-step size must be set the same as in the fluid and structure solvers; otherwise, the simulation may diverge due to asynchronism.

The implicit coupling stabilizes strongly-couple problems by applying features like subcylings. In OpenFOAM, the PIMPLE iterations sub-iterate each time step multiple times until a convergence threshold is reached. The number of iterations strongly affects the simulation stability and the computational time, which should be determined through a convergence test. User experience can help reduce the burden of these tests. The authors have suggested that using five iterations may be appropriate for ship hydroelasticity problems.

For the time being, the CFD-based FSI simulation is restricted to existing computational frameworks. Without access to the HPC system at the University of Strathclyde, the work presented in this thesis could not have been performed. While an FSI model is undoubtedly a handy tool, it does take much longer to obtain results compared to potential flow-based or rigid body models.

When it comes to structural solvers, a beam model is used to represent the ship structure. However, it should be noted that the beam idealizations, which are based on mathematical formulations assuming slow variation of properties along the structure, may not be suitable for dealing with discontinuities occurring at the transition between closed and open-deck regions of vessels with large deck openings.

Prior to conducting the coupled analysis, modal analysis of the structural model hull should be conducted to obtain information about the ship model’s vibrational behaviours, such as natural frequencies and modal shapes in both dry and wet conditions.

Nonetheless, with continuous technological advancements, it is now possible to use more complex simulations to model the multi-physics world. In specific field such as marine seakeeping, where elastic behaviour needs to be considered, the use of CFD-based FSI methods is becoming more prevalent compared to potential flow-based or rigid body models. The presented work demonstrated two fully coupled FSI frameworks for ship hydroelasticity problems, which overcome the typical limitations of similar computational approaches and provide insight for future work by open-community users.

8.4 Recommendations For Future Work

This chapter suggests several research directions that can be conducted based on the accomplishments of this work:

1. The study presented in Chapter 4.1 restricted the rigid ship responses in heave and pitch directions, therefore, only symmetrical responses and loads are evaluated. Future studies are recommended for free moving ship condition (including 6 DOFs motions), where strong viscous, asymmetrical and hence nonlinear coupled effects are expected to be observed.
2. The study performed in Chapter 4.2 has provided a very useful starting point for hydroelasticity investigation by implementing a simple barge geometry in wave conditions, specifically takes a prior step for following containership hydroelaticity analysis. The numerical dependencies are noticed, because the present CFD-DMB model only focus on the vertical bending deformations, with different setting ups compares to the experiments by (Senjanović et al. 2009). In future, this study should be extended of flexible barge in oblique waves with the concerns of torsional effects. It is worth noting that the low order beam theory, including Euler-Bernoulli and Timoshenko beam, may not accurate while torsional effects are considered. Therefore, high order beam, i.e., Valsov beam could be implemented in FEA model for anti-symmetrical loads analysis. This may provide a better understanding of the flexible barge motions under real operational conditions.
3. Beam model is extensively applied to represent the global ship characteristics in this project, i.e., Chapter 5, 6 and 7. However, the local deformation of hull surface cannot be captured, advanced structural model, for example full discretization of hull surface are recommended for the same studies for future. By comparison between the beam and full-ship model, the operability indices could be obtained to distinguish the advantages of using more advanced structural theory.
4. The research in Chapter 6 has shed some light to extend its applications to other conditions. (1) The research can be extended to investigate the asymmetric loads on the hull girder

while the ship is sailing in oblique wave and cross-wave conditions, e.g., coupled horizontal bending moments and torsional moments. (2) Shallow water wave condition is another research area to take for the investigation of hull girder vibrations induced by the nonlinearity of shallow wave components; however, the ship operational speed will not be as fast as in deep water due to squat effects. (3) The high-frequency vibration induced by the propeller and machinery is one of the primary sources of causing ship vibrations. A simplified propeller-shaft-ship system should be designed in MBDyn to investigate propeller induced high-frequency vibrations.

5. The work in Chapter 7 has pointed out a new direction for ship hydroelasticity analysis. Different ship damaged criteria are evaluated, which representing the most dangerous moment of a ship may occur in her life. Two recommendations were outlined below: (1) Another important damage scenario, i.e., damage openings at the keel which may be caused by grounding, are recommended to investigate to prevent and minimise such accident effects. However, the residual strength of the ship is significantly affected due to the loss of the structure, and it should be accurately estimated by the loss of section modulus and the stiffness loss of the structure. (2) The asymmetric structural loads, i.e., coupled horizontal bending moments and torsional moments induced by the flooding water, may lead to global ship roll motion and structural deformation, could be another research interest.
6. Since containership in still-water normally operate in hogging conditions, as the still-water load results achieved in Chapter 7.3.1. Any increase in the wave-induced hogging moment has an impact on the design loads for ultimate strength. Therefore, future research is recommended to find any specific conditions that may cause the ship hogging moments exceed the limitations which services for regulation formulations and marine design.

References

Abaqus, G. (2012). Abaqus 6.11. Dassault Systemes Simulia Corporation,. rovidence, RI, USA. **89:** v6.

Abbas, N., et al. (2015). "CFD prediction of unsteady forces on marine propellers caused by the wake nonuniformity and nonstationarity." Ocean Engineering **104**: 659-672.

Arai, M. (1998). "Numerical study of the impact of water on cylindrical shells, considering fluid-structure interaction PRADS." Practical design of ships and mobil units: 59-68.

Arai, M. and T. Miyauchi (1997). "Numerical simulation of the water impact on cylindrical shells considering fluid-structure interaction." Journal of the Society of Naval Architects of Japan **1997**(182): 827-835.

Bakti, F. P., et al. (2021). "Practical approach of linear hydro-elasticity effect on vessel with forward speed in the frequency domain." Journal of Fluids and Structures **101**.Baldock, T. E., et al. (1996). "A Laboratory Study of Nonlinear Surface Waves on Water." Philosophical Transactions: Mathematical, Physical and Engineering Sciences **354**(The Royal Society): 649-676.

Baquet, A., et al. (2017). "Numerical modeling using CFD and potential wave theory for three-hour nonlinear irregular wave simulations." International Conference on Offshore Mechanics and Arctic Engineering **57632**(American Society of Mechanical Engineers.).

Bauchau, et al. (2016). "Validation of flexible multibody dynamics beam formulations using benchmark problems." Multibody System Dynamics **37**(1): 29-48.

Begovic, E., et al. (2017). "An experimental study of hull girder loads on an intact and damaged naval ship." Ocean Engineering **133**: 47-65.

Begovic, E., et al. (2013). "Experimental assessment of intact and damaged ship motions in head, beam and quartering seas." Ocean Engineering **72**: 209-226.

Benra, et al. (2011). "A Comparison of One-Way and Two-Way Coupling Methods for Numerical Analysis of Fluid-Structure Interactions." Journal of Applied Mathematics **2011**: 1-16.

Bishop, et al. (1979). Hydroelasticity of ships, Cambridge University Press.

Bishop, et al. (1986). "A general linear hydroelasticity theory of floating structures moving in a seaway." Philosophical Transactions of the Royal Society of London. Series A, Mathematical and Physical Sciences **316**(1538): 375-426.

Bouscasse, B., et al. (2022). "Experimental analysis of wave-induced vertical bending moment in steep regular waves." Journal of Fluids and Structures **111**.

Bredmose, H. and N. G. Jacobsen (2010). "Breaking wave impacts on offshore wind turbine foundations: focused wave groups and CFD." International Conference on Offshore Mechanics and Arctic Engineering **49118**: 397-404.

Bungartz, et al. (2016). "preCICE – A fully parallel library for multi-physics surface coupling." Computers & Fluids **141**: 250-258.

Carrica, P. M., et al. (2007). "An unsteady single-phase level set method for viscous free surface flows." International Journal for Numerical Methods in Fluids **53**(2): 229-256.

Castiglione, T., et al. (2011). "Numerical investigation of the seakeeping behavior of a catamaran advancing in regular head waves." Ocean Engineering **38**(16): 1806-1822.

Ćatipović, I., et al. (2018). "Seakeeping experiments on damaged ship." Ships and Offshore Structures **14**(sup1): 100-111.

Celik, I. B., et al. (2008). "Procedure for estimation and reporting of uncertainty due to discretization in CFD applications." Journal of fluids Engineering-Transactions of the ASME **130**(7).

Chan, H. S., et al. (2003). "Global wave loads on intact and damaged Ro-Ro ships in regular oblique waves." Marine Structures **16**(4): 323-344.

Chen, et al. (2001). Experiment on extreme wave loads of a flexible ship model. Practical Design of Ships and Other Floating Structures. Proceedings of the Eighth International Symposium on Practical Design of Ships and Other Floating StructuresPRADS (Practical Design in Shipbuilding) Chinese Academy of Engineering, Chinese Society of Naval Architects and Marine Engineers, Chinese Institute of Navigation.

Chen, F., et al. (2019). "Vibration analysis of a submarine elastic propeller-shaft-hull system using FRF-based substructuring method." Journal of Sound and Vibration **443**: 460-482.

Chen, X., et al. (2016). "Computations of linear and nonlinear ship waves by higher-order boundary element method." Ocean Engineering **114**: 142-153.

Chourdakis, G. (2017). "A general OpenFOAM adapter for the coupling library preCICE."

Davis, et al. (1966). "Testing ship models in transient waves." David taylor model basin washington dc hydromechanics lab.

Degroote, J., et al. (2009). "Performance of a new partitioned procedure versus a monolithic procedure in fluid–structure interaction." Computers & Structures **87**(11-12): 793-801.

Demirel, Y. K., et al. (2017). "Predicting the effect of biofouling on ship resistance using CFD." Applied Ocean Research **62**: 100-118.

Dhinesh, G., et al. (2010). "Estimation of hull-propeller interaction of a self-propelling model hull using a RANSE solver." Ships and Offshore Structures **5**(2): 125-139.

Dhondt, G. (2017). "Calculix crunchix user's manual version 2.12." Munich, Germany, accessed Sept **21**: 2017.

Dietz, J. S. (2005). Application of Conditional Waves as Critical Wave Episodes for Extreme Loads on Marine Structures. Technical University of Denmark.

DNV, G. (2020). Rules for classification of high speed and light craft, January.

Draycott, S., et al. (2019). "Assessing extreme loads on a tidal turbine using focused wave groups in energetic currents." Renewable Energy **135**: 1013-1024.

El Moctar, O., et al. (2017). "Nonlinear computational methods for hydroelastic effects of ships in extreme seas." Ocean Engineering **130**: 659-673.

Elangovan, M. (2011). "Simulation of Irregular Waves by CFD." International Journal of Mechanical and Mechatronics Engineering **5**: 1379-1383.

Faltinsen, O. M. (1999). "Water entry of a wedge by hydroelastic orthotropic plate theory." Journal of ship research **43(03)**: 180-193.

Faltinsen, O. M. (2000). "Hydroelastic slamming." Journal of Marine Science and Technology **5(2)**: 49-65.

Featherstone, R. (2014). Rigid body dynamics algorithms, Springer.

Fols∅, L., et al. (2008). "Wave induced global loads for a damaged vessel." Ships and Offshore Structures **3**(4): 269-287.

G9 (2014). Offshore wind health and safety association, 2014 incident data report.

Gao, N., et al. (2016). "A numerical study on the nonlinear effects in focused wave modelling and forces on a semi-submerged horizontal cylinder." Ships and Offshore Structures **12**(4): 474-485.

Gao, Z., et al. (2013). "Numerical study of damaged ship flooding in beam seas." Ocean Engineering **61**: 77-87.

Gao, Z. and X. Tian (2021). "Numerical study on the wave-induced roll motion of a damaged ship in head seas." Applied Ocean Research **114**.

Gao, Z. L. and D. Vassalos (2015). "The dynamics of the floodwater and the damaged ship in waves." Journal of Hydrodynamics **27**(5): 689-695.

Gatzhammer, B. (2014). Efficient and flexible partitioned simulation of fluid-structure interactions (Doctoral dissertation, Technische Universität München).

Gerritsma, J. and W. Beukelman (1964). "The distribution of the hydrodynamic forces on a heaving andpitched shipmodel in still water." International Shipbuilding Progress **11**(123): 506-522.

Ghiringhelli, et al. (2000). "Multibody Implementation of Finite Volume C Beams." AIAA Journal **38**(1): 131-138.

Gu, M., et al. (1989). Time domain analysis of non-linear hydroelastic response of ships. International Symposium on Practical Design of Ships and Mobile Units (PRADS), 4th.

Han, F., et al. (2017). "Numerical investigation of wave-induced vibrations and their effect on the fatigue damage of container ships." Ocean Engineering **142**: 245-258.

Hashimoto, H., et al. (2017). "A numerical simulation method for transient behavior of damaged ships associated with flooding." Ocean Engineering **143**: 282-294.

Hasselmann, et al. (1973). "Measurements of wind-wave growth and swell decay during the Joint North Sea Wave Project (JONSWAP)." Ergaenzungsheft zur Deutschen Hydrographischen Zeitschrift, Reihe A.

He, X. D., et al. (2012). "Hydroelastic optimisation of a composite marine propeller in a non-uniform wake." Ocean Engineering **39**: 14-23.

Hess, J. L. and A. O. Smith (1967). "Calculation of potential flow about arbitrary bodies." Progress in Aerospace Sciences **8**: 1-138.

Hirdaris, S. and P. Temarel (2009). "Hydroelasticity of ships: Recent advances and future trends." Proceedings of the Institution of Mechanical Engineers, Part M: Journal of Engineering for the Maritime Environment **223**(3): 305-330.

Hirdaris, S. E., et al. (2014). "Loads for use in the design of ships and offshore structures." Ocean Engineering **78**: 131-174.

Hirdaris, S. E., et al. (2003). "Two- and three-dimensional hydroelastic modelling of a bulker in regular waves." Marine Structures **16**(8): 627-658.

Hirt, et al. (1981). "Volume of fluid (VOF) method for the dynamics of free boundaries." Journal of computational physics **39**(1): 201-225.

Hochbaum, A. C. (2002). "Towards the Simulation of Seakeeping and Manoeuvring based on the Computation of the Free Surface Viscous Ship Flow." In Proceedings of the 24th Symposium on Naval Hydrodynamics, Fukuoka, Japan.

Huang, S., et al. (2022). "Uncertainty analyses on the CFD–FEA co-simulations of ship wave loads and whipping responses." Marine Structures **82**.

IACS (2015). Longitudinal strength standard for container ships. UR S11A.

Iijima, K., et al. (2008). "Structural response of a ship in severe seas considering global hydroelastic vibrations." Marine Structures **21**(4): 420-445.

IMO (2003). "Interim guidelines for the approval of alternative methods of design and construction of oil tankers under Regulation 13F (5) of Annex 1 of MARPOL 73/78." Resolution MEPC **110**(49).

Islam, H. and C. G. Soares (2019). "Uncertainty analysis in ship resistance prediction using OpenFOAM." Ocean Engineering **191**.

ITTC (2011). Practical Guidelines for Ship CFD Applications.

ITTC (2017). ITTC Quality System Manual Recommended Procedures and Guidelines. Seakeeping committe of the 28th ITTC.

Jacobsen, N. G., et al. (2012). "A wave generation toolbox for the open-source CFD library: OpenFoam®." International Journal for Numerical Methods in Fluids **70**(9): 1073-1088.

Jasak, et al. (2007). "OpenFOAM: A C++ Library for Complex Physics Simulations." International Workshop on Coupled Methods in Numerical Dynamics **1000**: 1-20.

Jasak, H. (2009). Dynamic Mesh Handling in OpenFOAM. 47th AIAA Aerospace Sciences Meeting including The New Horizons Forum and Aerospace Exposition.

Jiao, J., et al. (2021). "Viscous fluid–flexible structure interaction analysis on ship springing and whipping responses in regular waves." Journal of Fluids and Structures **106**.

Jiao, J., et al. (2021). "Slamming and green water loads on ship sailing in regular waves predicted by coupled CFD–FEA approach." Ocean Engineering.

Jiao, J., et al. (2021). "A CFD–FEA two-way coupling method for predicting ship wave loads and hydroelastic responses." Applied Ocean Research **117**.

Karimirad, M., et al. (2011). "Hydroelastic code-to-code comparison for a tension leg spar-type floating wind turbine." Marine Structures **24**(4): 412-435.

Kashiwagi, M. (2000). "Research on Hydroelastic Responses of VLFS: Recent Progress and Future Work." International Journal of Offshore and Polar Engineering **10(02)**.

Kawamura, K., et al. (2016). "SPH simulation of ship behaviour in severe water-shipping situations." Ocean Engineering **120**: 220-229.

Kim, et al. (2014). "Numerical analysis on springing and whipping using fully-coupled FSI models." Ocean Engineering **91**: 28-50.

Kim, D. and T. Tezdogan (2022). "CFD-based hydrodynamic analyses of ship course keeping control and turning performance in irregular waves." Ocean Engineering **248**.

Korvin-Kroukovsky, B. V. (1955). Investigation of ship motions in regular waves. Stevens Institute of Technology, Experimental Towing Tank,, Hoboken, New Yersey, USA,, Annual Meeting of the Society of Naval Architects and Marine Engineers, SNAME Transactions.

Lakshmynarayanana, P. A. and P. Temarel (2019). "Application of CFD and FEA coupling to predict dynamic behaviour of a flexible barge in regular head waves." Marine Structures **65**: 308-325.

Lakshmynarayanana, P. A. and P. Temarel (2020). "Application of a two-way partitioned method for predicting the wave-induced loads of a flexible containership." Applied Ocean Research **96**.

Lakshmynarayanana, P. A. K. and S. Hirdaris. (2020). "Comparison of nonlinear one- and two-way FFSI methods for the prediction of the symmetric response of a containership in waves." Ocean Engineering **203**.

Larsson, L., et al. (2003). "Benchmarking of computational fluid dynamics for ship flows: the Gothenburg 2000 workshop." Journal of ship research **47**(01): 63-81.

Larsson, L., et al. (2013). Numerical ship hydrodynamics: an assessment of the Gothenburg 2010 workshop, Springer.

Larsson, L., et al. (2015). "Tokyo 2015: A workshop on CFD in ship hydrodynamics." Tokyo, Japan: National Maritime Research Institute (NMRI).

Lavroff, J., et al. (2013). "Wave slamming loads on wave-piercer catamarans operating at high-speed determined by hydro-elastic segmented model experiments." Marine Structures **33**: 120-142.

Le Touzé, D., et al. (2010). "SPH simulation of green water and ship flooding scenarios." Journal of Hydrodynamics **22**(S1): 231-236.

Lee, Y., et al. (2012). "Global wave loads on a damaged ship." Ships and Offshore Structures **7**(3): 237-268.

Li, J., et al. (2017). "Hydroelastic analysis of underwater rotating elastic marine propellers by using a coupled BEM-FEM algorithm." Ocean Engineering **146**: 178-191.

Li, J. X., et al. (2012). "Numerical investigation of the effect of current on wave focusing." China Ocean Engineering **26**(1): 37-48.

Li, X., et al. (2022). "Coupled CFD-MBD numerical modeling of a mechanically coupled WEC array." Ocean Engineering **256**.

Lin, H. J. and J. J. Lin (1996). "Nonlinear hydroelastic behavior of propellers using a finite-element method and lifting surface theory." Journal of Marine Science and Technology **1(2)**: 114-124.

Lin, W. M. and D. Yue (1991). "Numerical solutions for large-amplitude ship motions in the time domain."

Lin, Z. (2019). Experimental Investigation Regarding the Landing Manoeuvre of a Crew Transfer Vessel University of Strathclyde Department of Naval Architecture , Ocean and Marine Engineering.

Liu, D. and P. Lin (2008). "A numerical study of three-dimensional liquid sloshing in tanks." Journal of computational physics **227**(8): 3921-3939.

Liu, Y., et al. (1990). Comparison of higher-order boundary element and constant panel methods for hydrodynamic loadings. The First ISOPE European Offshore Mechanics Symposium, OnePetro.

Liu, Y., et al. (2019). "Aeroelastic analysis of a floating offshore wind turbine in platform-induced surge motion using a fully coupled CFD-MBD method." Wind Energy **22**(1): 1-20.

Liu, Y., et al. (2017). "Establishing a fully coupled CFD analysis tool for floating offshore wind turbines." Renewable Energy **112**: 280-301.

Lloyd's_Register (1996). World Casualty Statistics. Lloyd's Register of Shipping

Lu, et al. (2000). "Coupled analysis of nonlinear interaction between fluid and structure during impact." Journal of Fluids and Structures **14(1)**: 127-146.

Lu, D., et al. (2016). "A method to estimate the hydroelastic behaviour of VLFS based on multi-rigid-body dynamics and beam bending." Ships and Offshore Structures **14**(4): 354-362.

Ma, S. and H. Mahfuz (2012). "Finite element simulation of composite ship structures with fluid structure interaction." Ocean Engineering **52**: 52-59.

Maki, K. J., et al. (2011). "Hydroelastic impact of a wedge-shaped body." Ocean Engineering **38**(4): 621-629.

Manderbacka, T., et al. (2015). "Transient response of a ship to an abrupt flooding accounting for the momentum flux." Journal of Fluids and Structures **57**: 108-126.

Manderbacka, T., et al. (2019). "An overview of the current research on stability of ships and ocean vehicles: The STAB2018 perspective." Ocean Engineering **186**: 106090.

Markus, D., et al. (2013). "A CFD approach to modeling wave-current interaction." International Journal of Offshore and Polar Engineering **23**.

Masarati, P. (2017). "MBDyn Input File Format Version 1.7. 3." Politecnico di Milano.

Masarati, P., et al. (2014). "An Efficient Formulation for General-Purpose Multibody/Multiphysics Analysis." Journal of Computational and Nonlinear Dynamics **9**(4).

Méhauté, B. (1976). An Introduction to Hydrodynamics and Water Waves.

Mehl, M., et al. (2016). "Parallel coupling numerics for partitioned fluid–structure interaction simulations." Computers & Mathematics with Applications **71**(4): 869-891.

Menter, F. R. (1994). "Two-equation eddy-viscosity turbulence models for engineering applications." AIAA Journal **32**(8): 1598-1605.

Mikulić, A., et al. (2018). "Wave-Induced Vertical Motions and Bending Moments in Damaged Ships." Journal of Marine Science and Application **17**(3): 389-405.

Nakos, D. and P. Sclavounos (1991). "Ship motions by a three dimensional Rankine Panel Method."

Newman, J. N. (1979). "The theory of ship motions." Advances in applied mechanics.

Ning, D. Z., et al. (2009). "Free-surface evolution and wave kinematics for nonlinear uni-directional focused wave groups." Ocean Engineering **36**(15-16): 1226-1243.

Oberkampf, W. L. and T. G. Trucano (2002). "Verification and validation in computational fluid dynamics." Progress in Aerospace Sciences **38**(3): 209-272.

Paik, et al. (2009). "Strongly coupled fluid–structure interaction method for structural loads on surface ships." Ocean Engineering **36**(17-18): 1346-1357.

Parunov, et al. (2015). "Comparison of two practical methods for seakeeping assessment of damaged ships." Analysis and Design of Marine Structures: 37-44.

Phillips, S., et al. (2015). "Crew transfer vessel performance evaluation." Design & Operation of Wind Farm Support Vessels: 28-29.

Price, W. G. and W. Yousheng (1985). Hydroelasticity of marine structures. Theoretical and applied mechanics, Elsevier**:** 311-337.

Procedings, I. T. T. C. (2014). "Practical Guidelines for Ship CFD Applications ITTC Recommended Procedures and Guidelines." International Towing Tank Conference **section 7.5-03-02-03**.

Remy, F., et al. (2006). "Experimental and numerical study of the wave response of a flexible barge." Hydroelasticity in Marine Technology, Wuxi, China: 255-264.

Romanowski, A., et al. (2019). "Development of a CFD methodology for the numerical simulation of irregular sea-states." Ocean Engineering **192**.

Salvesen, N., et al. (1970). "Ship motions and sea loads."

Santos, T. A. and C. Guedes Soares (2008). "Study of damaged ship motions taking into account floodwater dynamics." Journal of Marine Science and Technology **13**(3): 291-307.

Seltmann and Astrid (2015). Global marine insurance report 2015. International Union of Marine Insurance (IUMI) Conference.

Sen, D. (2002). "Time-domain computation of large amplitude 3D ship motions with forward speed." Ocean Engineering **29**(973–1002).

Senjanović, et al. (2009). "Hydroelasticity of large container ships." Marine Structures **22**(2): 287-314.

Senjanović, et al. (2008). "Investigation of ship hydroelasticity." Ocean Engineering **35**(5-6): 523-535.

Shen, Z. R., et al. (2014). "URANS simulations of ship motion responses in long-crest irregular waves." Journal of Hydrodynamics **26**(3): 436-446.

Siddiqui, M. A., et al. (2020). "Experimental studies of a damaged ship section in beam sea waves." Applied Ocean Research **97**.

Simonsen, C. D., et al. (2013). "EFD and CFD for KCS heaving and pitching in regular head waves." Journal of Marine Science and Technology **18**(4): 435-459.

Smith, C. S. (1977). "Influence of local compressive failure on ultimate longitudinal strength of a ship's hull." Trans PRADS **1977**: 73-79.

Soares, C., et al. (2009). "Damage Assessment After Accidental Events: Report of Committee V. 1."

Stern, F., et al. (2006). "Quantitative V&V of CFD simulations and certification of CFD codes." International Journal for Numerical Methods in Fluids **50**(11): 1335-1355.

Stern, F., et al. (2001). "Comprehensive approach to verification and validation of CFD simulations—part 1: methodology and procedures." J. Fluids Eng. **123**(4): 793-802.

Stern, F., et al. (2013). "Computational ship hydrodynamics: Nowadays and way forward." International Shipbuilding Progress **60(1-4)**: 3-105.

Sun, Z., et al. (2021). "Investigation of Non-Linear Ship Hydroelasticity by CFD-FEM Coupling Method." Journal of Marine Science and Engineering **9**(5).

Takami, T. and K. Iijima (2019). "Numerical investigation into combined global and local hydroelastic response in a large container ship based on two-way coupled CFD and FEA." Journal of Marine Science and Technology **25**(2): 346-362.

Takami, T., et al. (2020). "Efficient FORM-based extreme value prediction of nonlinear ship loads with an application of reduced-order model for coupled CFD and FEA." Journal of Marine Science and Technology **25**(2): 327-345.

Tamer, A. (2021). "Aeroelastic Response of Aircraft Wings to External Store Separation Using Flexible Multibody Dynamics." Machines **9**(3).

Terziev, M., et al. (2018). "Numerical investigation of the behaviour and performance of ships advancing through restricted shallow waters." Journal of Fluids and Structures **76**: 185-215.

Tezdogan, T., et al. (2015). "Full-scale unsteady RANS CFD simulations of ship behaviour and performance in head seas due to slow steaming." Ocean Engineering **97**: 186-206.

Tezdogan, T., et al. (2016). "Full-scale unsteady RANS simulations of vertical ship motions in shallow water." Ocean Engineering **123**: 131-145.

Uekermann, B., et al. (2017). Official preCICE adapters for standard open-source solvers. Proceedings of the 7th GACM colloquium on computational mechanics for young scientists from academia.

VERITAS, B. (2018). Rules for the Classification of Crew Boat. Guidance Note. **NR490**.

Watanabe, E., et al. (2004). "Hydroelastic analysis of pontoon-type VLFS: a literature survey." Engineering Structures **26**(2): 245-256.

Wei, et al. (2022). "A fully coupled CFD-DMB approach on the ship hydroelasticity of a containership in extreme wave conditions." Journal of Marine Science and Engineering **10**(11): 1778.

Wei, W., et al. (2017). "A discrete-modules-based frequency domain hydroelasticity method for floating structures in inhomogeneous sea conditions." Journal of Fluids and Structures **74**: 321-339.

Wei, W., et al. (2018). "A time-domain method for hydroelasticity of very large floating structures in inhomogeneous sea conditions." Marine Structures **57**: 180-192.

Wei, Y. and T. Tezdogan (2022). "A fluid-structure interaction model on the hydroelastic analysis of a container ship using Precice." In 41st International Conference on Ocean, Offshore and Arctic Engineering **OMAE2022-78131**.

Weller, H. G. (2002). "Derivation, modelling and solution of the conditionally averaged two-phase flow equations." Nabla Ltd, No Technical Report TR/HGW **2**(2002): 9.

Yago, K. and H. Endo (1996). "On the Hydroelastic Response of Box-Shaped Floating Structure with Shallow Draft Tank Test with Large Scale Model." Journal of the Society of Naval Architects of Japan **1996**(180): 341-352.

Zhang, J. S., et al. (2014). "Numerical simulation of wave–current interaction using a RANS solver." Ocean Engineering **75**: 157-164.

Zhang, L., et al. (2021). "A practical direct URANS CFD approach for the speed loss and propulsion performance evaluation in short-crested irregular head waves." Ocean Engineering **219**.

Zhang, X., et al. (2018). "A time domain discrete-module-beam-bending-based hydroelasticity method for the transient response of very large floating structures under unsteady external loads." Ocean Engineering **164**: 332-349.

Zhang, Y., et al. (2021). "Study on the unequivalence between stiffness loss and strength loss of damaged hull girder." Ocean Engineering **229**.

Zhang, Z. R., et al. (2006). "Application of CFD in ship engineering design practice and ship hydrodynamics." Journal of Hydrodynamics, Ser. B **18**(3): 315-322.

Zhou, Y., et al. (2019). "Investigation of focused wave impact on floating platform for offshore floating wind turbine: a CFD study. ." Proceedings of the ASME 2019 38th International Conference on Ocean, Offshore and Arctic Engineering OMAE2019 **96043**.

Zhou, Y., et al. (2019). "Numerical Modelling of Dynamic Responses of a Floating Offshore Wind Turbine Subject to Focused Waves." Energies **12**(18).

Zhou, Y., et al. (2021). "Assessing focused wave applicability on a coupled aero-hydro-mooring FOWT system using CFD approach." Ocean Engineering **240**.